Intensity Effects in Dielectric Laser Accelerator Structures

Egenolf, Thilo

(2020)

DOI (TUprints): https://doi.org/10.25534/tuprints-00014139

Publikationstyp: Dissertation

Fachbereich: 18 Fachbereich Elektrotechnik und Informationstechnik

Quelle des Originals: https://tuprints.ulb.tu-darmstadt.de/14139

Intensity Effects in Dielectric Laser Accelerator Structures

Intensitätseffekte in lasergetriebenen dielektrischen Beschleunigungsstrukturen
Zur Erlangung des Grades eines Doktors der Naturwissenschaften (Dr. rer. nat.)
genehmigte Dissertation von Thilo Egenolf aus Wiesbaden
Tag der Einreichung: 15.06.2020, Tag der Prüfung: 09.10.2020
Darmstadt — D 17

1. Gutachten: Prof. Dr. Oliver Boine-Frankenheim
2. Gutachten: Prof. Dr. Holger Podlech

TECHNISCHE
UNIVERSITÄT
DARMSTADT

Fachbereich Elektrotechnik
und Informationstechnik
Institut für Teilchenbeschleunigung
und Elektromagnetische Felder

Intensity Effects in Dielectric Laser Accelerator Structures
Intensitätseffekte in lasergetriebenen dielektrischen Beschleunigungsstrukturen

Genehmigte Dissertation von Thilo Egenolf aus Wiesbaden

1. Gutachten: Prof. Dr. Oliver Boine-Frankenheim
2. Gutachten: Prof. Dr. Holger Podlech

Tag der Einreichung: 15.06.2020
Tag der Prüfung: 09.10.2020

Darmstadt — D 17

Bitte zitieren Sie dieses Dokument als:
URN: urn:nbn:de:tuda-tuprints-141399
URL: http://tuprints.ulb.tu-darmstadt.de/14139

Erklärung zur Dissertation gemäß der Promotionsordnung der TU Darmstadt

§ 8 Abs. 1 lit. c PromO
Ich versichere hiermit, dass die elektronische Version meiner Dissertation mit der schriftlichen Version übereinstimmt.

§ 8 Abs. 1 lit. d PromO
Ich versichere hiermit, dass zu einem vorherigen Zeitpunkt noch keine Promotion versucht wurde.

§ 9 Abs. 1 PromO
Ich versichere hiermit, dass die vorliegende Dissertation selbstständig und nur unter Verwendung der angegebenen Quellen verfasst wurde.

§ 9 Abs. 2 PromO
Die Arbeit hat bisher noch nicht zu Prüfungszwecken gedient.

Darmstadt, den 15.06.2020

(T. Egenolf)

Abstract

Electron accelerators have a wide range of applications in basic research, medicine and industry. In order to reduce costs and size of future devices and facilities, advanced compact accelerator concepts are subject to extensive research and development efforts in accelerator physics. A promising approach is the dielectric laser accelerator (DLA). The electromagnetic near-fields of an ultra-short laser pulse scattered by a dielectric structure are used to accelerate electrons. Dielectrics increases the achievable accelerating gradient by a factor of at least 10 in comparison to metallic structures. Recent progress in the development of femtosecond lasers and lithographic techniques in semiconductor fabrication has paved the way to experimental demonstration of DLAs in 2013. Possible applications of DLAs are in attosecond science, in ultrafast electron-microscopy and -diffraction, and in providing relativistic electrons for lithography and radiotherapy.

The use of near-fields in structures with period lengths in the order of micrometers leads to complicated particle dynamics during acceleration. Theoretical descriptions of the electromagnetic fields and the resulting particle dynamics are presented in this thesis. In order to confine the particles in the accelerating structures, a focusing scheme is introduced which is adapted from ion accelerators. This allows to transport particles through a DLA structure of arbitrary length.

Due to non-linear dynamics of the accelerated electrons, the particle trajectories are calculated numerically. A simulation tool based on the analytical description of the electromagnetic fields in the structures is implemented. Since DLA structures are quasi-periodic, the description simplifies to one complex number per structure period, i.e., the spatial harmonic of the synchronous accelerating mode. The required computational effort is thus significantly reduced as compared to the full electromagnetic fields.

Many applications of DLAs require particle distributions of high charge. The beam dynamics are additionally affected by wake fields, which are generated by the interaction of the charge distribution ensemble with the dielectric structures. Detailed studies of wake fields in DLA structures are discussed in this thesis. Moreover, first measurements of energy spectrum modulations caused by wake fields are presented.

The wake field effects can lead to instabilities. For the analysis of possible instabilities, wake fields are integrated in the aforementioned numerical simulation tool. This extended tool is applied to compare particle dynamics with simplified analytical models of longitudinal and transverse wake effects and instabilities. These studies provide estimates for the maximum attainable charges of an accelerated particle bunch. For higher bunch charges, the effects from the wake fields exceed the accelerating and focusing laser fields and thus lead to beam loss. Finally, a possible damping mechanism is presented in order to counteract the instabilities and increase the bunch charge limits.

Zusammenfassung

Elektronenbeschleuniger haben ein breites Anwendungsspektrum in der Grundlagenforschung, in der Medizin und in der Industrie. Zur Reduktion von Kosten und Größe zukünftiger Anlagen wird intensiv an fortschrittlichen kompakten Beschleunigerkonzepten geforscht. Ein vielversprechendes Konzept ist der dielektrische Laser-Beschleuniger (engl. DLA), auch Glasbeschleuniger genannt. Dabei werden die elektromagnetischen Nahfelder eines Laserpulses an einer dielektrischen Struktur genutzt, um Elektronen zu beschleunigen. Der Einsatz von Dielektrika erhöht den erreichbaren Beschleunigungsgradienten im Vergleich zu metallischen Strukturen um mindestens eine Größenordnung.

Erst die Fortschritte in der Entwicklung von Femtosekunden-Lasern und lithografischen Herstellungsverfahren in der Halbleiterindustrie haben die experimentelle Demonstration von DLAs ermöglicht. Allerdings führt die Nutzung der Nahfelder in Strukturen mit Periodenlängen in der Größenordnung weniger Mikrometer zu einer komplizierten Teilchendynamik während der Beschleunigung. Die theoretische Beschreibung der elektromagnetischen Felder und der daraus resultierenden Teilchendynamik wird in dieser Arbeit vorgestellt. Weiterhin wird ein Fokussierungsschema präsentiert, dass den Teilchentransport durch eine DLA Struktur beliebiger Länge ermöglicht.

Da die beschleunigten Teilchen eine nichtlineare Dynamik aufweisen, werden die Teilchentrajektorien numerisch bestimmt. Dazu wird ein Simulationstool basierend auf der theoretischen Beschreibung der elektromagnetischen Felder in den Strukturen vorgestellt. Durch die (Quasi-) Periodizität der Strukturen kann auf die Berechnung der vollständigen elektromagnetischen Felder verzichtet werden. Stattdessen wird die Beschreibung auf eine komplexe Zahl pro Strukturperiode – die räumliche Harmonische der synchronen, beschleunigenden Mode – reduziert und der benötigte Rechenaufwand dadurch deutlich verringert.

Mögliche Anwendungen für DLAs finden sich in der Attosekundenphysik, in der ultraschnellen Elektronenmikroskopie und -beugung und zur Bereitstellung relativistischer Elektronen für Lithografie und Strahlentherapie. Für diese Anwendungen werden nicht nur beschleunigte Einzelteilchen, sondern Teilchenverteilungen mit höherer Ladung benötigt. In diesem Fall wird die Strahldynamik zusätzlich durch die Kielwellenfelder der bewegten Ladungen, die durch die Wechselwirkung mit den dielektrischen Strukturen entstehen, beeinflusst. Diese Kielwellenfelder werden in dieser Arbeit untersucht und erstmals Messungen von durch Kielwellenfeldern in DLA Strukturen verursachten Veränderungen des Energiespektrums dargestellt.

Des Weiteren können die Effekte verursacht durch die Kielwellenfelder zu Instabilitäten in der Teilchendynamik führen. Zur Analyse möglicher Instabilitäten wird das numerische Simulationstool um die Einflüsse der Kielwellenfelder erweitert. Das erweiterte

Simulationstool wird im Rahmen dieser Arbeit zum Vergleich der Teilchendynamik mit vereinfachten analytischen Modellen von longitudinalen und transversalen Kielwelleneffekten und Instabilitäten eingesetzt. Diese Studien ergeben Abschätzungen der maximal erreichbaren Ladungen eines beschleunigten Teilchenpaketes, bevor die Effekte der Kielwellenfelder die beschleunigenden und fokussierenden Laserfelder übersteigen. Abschließend wird in dieser Arbeit ein möglicher Dämpfungsmechanismus präsentiert, der es ermöglichen würde, die Ladungsgrenzen zu erhöhen.

Contents

Introduction

Particle accelerators serve as machines for many applications in science, medicine and industry. In addition to major scientific successes such as the discovery of the Higgs boson in 2012, they are, for example, used as coherent X-ray light sources, for particle therapy and radioisotope production for medical purposes, and as ion implanters for semiconductor doping. In conventional accelerator facilities, the acceleration is usually done by metallic cavities. Due to the electrical breakdown in such structures in the presence of high electric fields, the maximum accelerating gradients are limited to a range of 10 to $100\,\mathrm{MV\,m^{-1}}$. The devices are driven by electromagnetic waves in the radio-frequency (rf) part of the spectrum with frequencies from a few hundred MHz to several GHz. The dimensions of these cavities are thus of the order of centimeters to meters. Therefore, linear accelerators based on rf technology are often large and expensive due to the required accelerator length.

A reduction in size and costs is desirable or even necessary to make future applications possible. The utilization of new materials and technologies enables advanced accelerator concepts. One of these concepts is based on dielectric grating structures processed by lithographic techniques and driven by ultra-short pulsed lasers, called Dielectric Laser Accelerators (DLAs), which is introduced in Sec. I.1. This dissertation focuses on the beam dynamics in such structures and intensity effects, that limit the number of accelerated particles per second for possible applications. Section I.2 gives a brief overview of the dissertation.

I.1 Dielectric Laser Acceleration

The size of accelerator cavities depends on the wavelength of the driving electromagnetic waves. One way to reduce the dimensions of the cavities to a few microns is the use of optical frequencies instead of rf. This comes along with shorter pulse lengths. Both of them theoretically increase the breakdown voltage, which enables higher gradients and a shorter accelerator length. However, optical frequencies lead to high power loss in metallic cavities. Thus, suitable substitutes are dielectric materials which are transparent at these frequencies. Appropriate dielectrics are for example silicon and amorphous silicon dioxide, also known as fused silica. Figure I.1 shows the absorption coefficient and the refractive index for both materials. With a few exceptions, absorption at optical frequencies in the shown frequency range is negligible for these materials.

The electromagnetic fields in the structures are limited by the damage threshold depending significantly on the pulse length of the exposing laser [1, 2, 3]. At pulse lengths

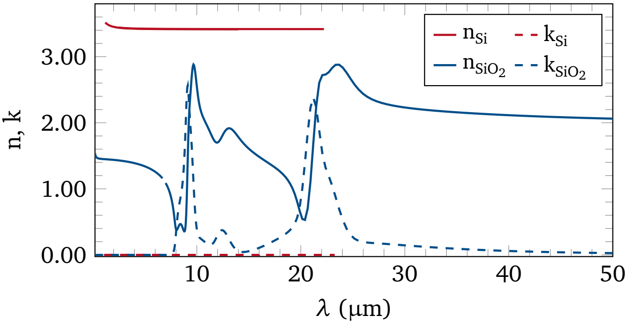

Figure I.1: Refractive index n and absorption coefficient k of silicon and fused silica. The data is taken from [4] based on [5, 6] for silicon and from [7] for fused silica at room temperature.

above 10 ps, the primary breakdown mechanism is thermal heating. For shorter pulse lengths, it changes to ablation and multiphoton ionization. The damage threshold fluence of fused silica, i.e., the maximum radiant energy per unit area without damage, is about $1\,\mathrm{J\,cm^{-2}}$ below 2 ps pulse length, which corresponds to gradients on the order of $1\,\mathrm{GV\,m^{-1}}$. These gradients are 1 to 2 orders of magnitude above the gradients achievable in conventional metallic rf cavities. Therefore, the accelerator length is decreased by 1 to 2 orders of magnitude to get the same beam energy gain. For silicon, the damage threshold fluence is about one order of magnitude lower than for fused silica. However, the refractive index and the relative permittivity of silicon is larger (see Fig. I.1). Thus, gradients in the same order of magnitude as in fused silica can be realized.

Evanescent waves can be employed in order to accelerate charged particles with such high gradients. Concepts using the inverse Cherenkov and Smith-Purcell effects were already proposed in 1962 [8, 9]. Nevertheless, only significant progress in the development of lithographic techniques in the semiconductor production in the last decades have enabled dielectric structure fabrication with sub-micron precision. Moreover, ultra-short pulsed solid-state lasers are now available. That makes the experimental demonstration of the acceleration mechanism possible. Peralta et al. performed the first demonstration of DLAs for relativistic electrons at SLAC [10] and Breuer et al. for non-relativistic electrons at FAU Erlangen-Nuremberg [11]. Further intensive theoretical and experimental studies followed. Most of them are funded by the Gordon and Betty Moore Foundation within the Accelerator on a Chip International Program (ACHIP). The studies for this dissertation were also conducted in course of the ACHIP collaboration.

Figure I.2 describes the basic design of a dielectric laser acceleration structure: an electron beam passes the dielectric structure with (quasi-) periodic features with a distance in the range of the evanescent fields from the structure. These fields are driven

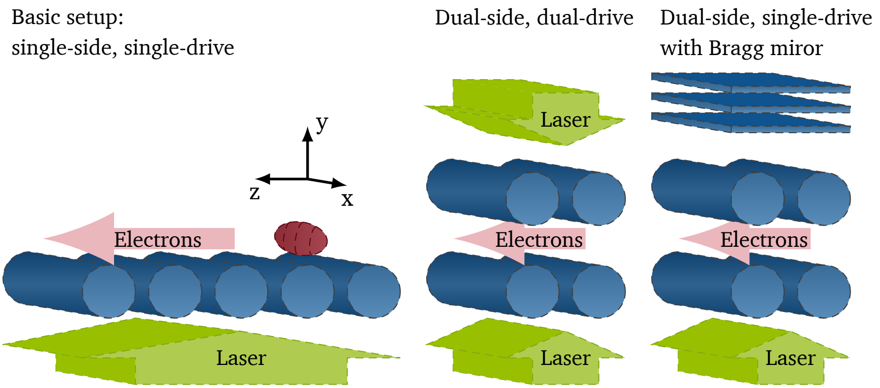

Figure I.2: Dielectric laser acceleration structures.

by a short-pulsed laser propagating perpendicular to the electron beam and polarized in the direction of the electron beam motion. To enhance the accelerating fields a second structure, in the two right drawings in Fig. I.2 a second row of pillars, is added on the other side of the electron beam. Furthermore a second laser beam or a dielectric Bragg mirror can be used to further enhance and symmetrize the fields in the structure. The length of one grating period is given by $\lambda_z = \beta\lambda_0$ with the laser wavelength λ_0, the velocity βc_0 of the electron beam, and the speed of light c_0. In order to accelerate all electrons of a particle distribution, the width of the distribution determines the required laser pulse length and in order to illuminate the entire dielectric structure, the structure length determines the laser spot size.

The Lawson-Woodward theorem [12, 13, 14, 15] prohibits a net energy gain of a particle interacting with a laser field assumed as a plane wave in vacuum. In such a field, a particle gains as much energy in one half of the optical cycle as it loses again in the second half. The dielectric structure near the interaction region acts as a near field source. The evanescent fields from the dielectric structure are periodically modulated in z-direction due to optical path differences between different positions in z. Due to the synchronization of the grating period length the the electron beam velocity, the field modulation has the right periodicity and acceleration is possible. In order to describe the acceleration mechanism within one grating period in detail, snapshots of the longitudinal electric fields are plotted in Fig. I.3. During the first and the last quarter of the period, the longitudinal electric field at the particle location is positive resulting in a negative energy gain for electrons as negatively charged particles. In the second and third quarter of the period, the longitudinal electric field is negative and the energy gain therefore positive. Since the absolute values of the electric field in the center of the period between the pillars ($z = 1\,\mu\text{m}$) is larger than at the boundaries of the period

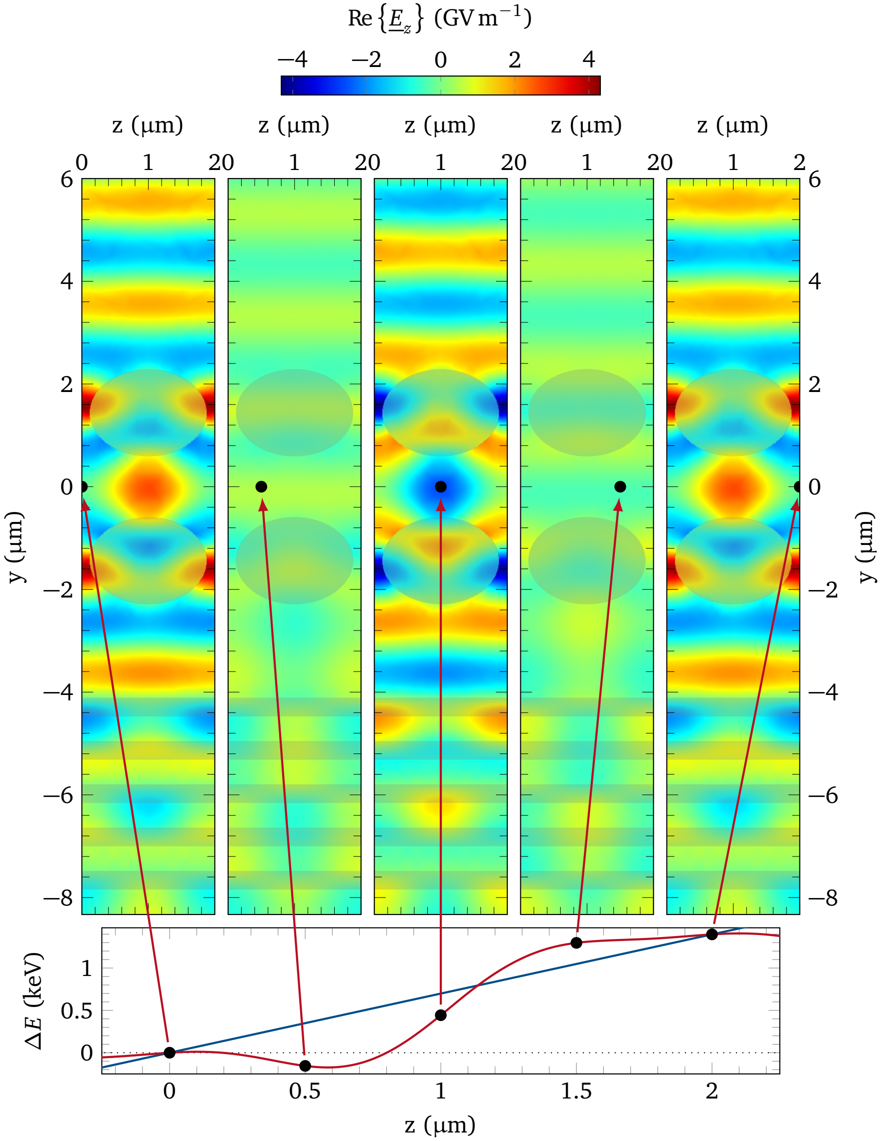

Figure I.3: Principle of acceleration in a DLA grating period: energy gain along the period (bottom, red curve) compared to a linear energy gain (blue curve) and snapshots of the longitudinal electric field at five points in time across the period (top). The driving laser comes from the top and the shaded material regions are fused silica.

($z = 0\,\mu\text{m}$), the net energy gain is positive. If we consider a lattice with many DLA grating periods, the energy deviation from a linearized energy gain within one period is negligible compared to the energy gain along the entire lattice. The crucial variable is thus the average gradient instead of the exact curve of the energy gain within one period (see the blue curve in the bottom plot of Fig. I.3). This enables the approach to study the beam dynamics in a lattice by single-particle tracking with only one momentum change per DLA grating period. The snapshots depict also the function of the Bragg mirror to symmetrize the fields in the gap between the pillars. The field source for the simulation is a plane wave with $1\,\text{GV}\,\text{m}^{-1}$ from the top. The wave is almost completely reflected at the Bragg layers, whereas the distance between the pillars and the first Bragg layer is chosen such that the center of the gap is a plane of symmetry for the resulting field and the far-field wave on top of the structure has an almost doubled peak field.

The first demonstration of DLAs at SLAC reported a gradient of more than $250\,\text{MV}\,\text{m}^{-1}$ in a fused silica rectangular double grating driven by single side illumination with a 800 nm Ti:sapphire laser [10]. In the same setup, the laser pulse duration was later shortened to $\tau = 90\,\text{fs}$ FWHM and the gradient increased to $690\,\text{MV}\,\text{m}^{-1}$ [16]. The current record gradient of $850\,\text{MV}\,\text{m}^{-1}$ was reached at UCLA in the same grating structure but with $\tau = 45\,\text{fs}$ FWHM laser pulse duration and significantly enhanced incident electric peak field [17]. In this experiment, nonlinear effects in the dielectric materials like the Kerr phase shift were observed for the first time. Due to these effects, the originally expected gradient of $1.8\,\text{GV}\,\text{m}^{-1}$ was reduced significantly. In order to increase not only the gradient but also the absolute energy gain, the interaction length has to be extended. Therefore, the pulse front tilt technique was applied and an interaction length 50 times larger than the laser pulse duration was demonstrated [18]. A pulse front tilt means that the arrival time of a laser pulse varies across the transverse beam profile (see Fig. I.4).

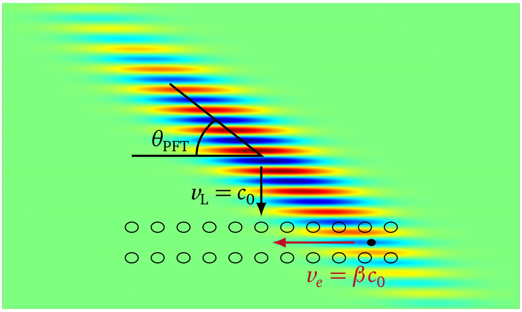

Figure I.4: Layout of the DLA interaction between an electron propagating from right to left with velocity $v_e = \beta c_0$ and a pulse-front-tilted laser beam propagating from top to bottom. The tilt angle is given by $\theta_{\text{PFT}} = \arctan \beta^{-1}$.

In the sub-relativistic regime, the first demonstration of acceleration in a DLA structure was done with 27.7 keV electrons and a single sided fused silica rectangular grating with a maximum accelerating gradient of 25 MV m^{-1} at the 3rd harmonic [11, 19]. The gradient was later increased to 370 MV m^{-1} [20]. Leedle et al. demonstrated acceleration and deflection depending on the phase difference between two excitation lasers [21]. Based on this setup, Black et al. reported on DLA structures used as focusing electron lens [22] and for bunching [23, 24]. The fabrication of a structure with Bragg mirror and the acceleration of sub-relativistic electrons in this structure was demonstrated by Yousefi et al. in order to do not need the second driving laser [25]. Free space coupling of the laser beam into the DLA structure was completely avoided in the first waveguide-integrated DLA, which was demonstrated by Sapra et al. [26].

Theoretical studies on DLAs were started parallel to the first experimental demonstrations [27]. Design and optimization of DLA structures [28, 29, 30] lead to beam dynamics studies [31] and the theoretical demonstration of a scheme for beam confinement [32] in DLA structures of arbitrary length.

Relativistic DLA experiments are planned or already performed at conventional accelerator facilities such as SwissFEL at the Paul Scherrer Institute (PSI) [33, 34] and SINBAD at DESY [35, 36]. In these accelerator lattices, it is possible to focus all particles of the beam to the size of the gap of a DLA structure in the micrometer range. This leads to intensity effects disturbing the energy and bunch distribution. In a similar way, intensity effects also limit possible applications of DLAs because a high beam current is crucial for the success of the particular application. For example, the beam current is used to determine the luminosity, which is the ratio of the number of events per second detected in an experiment to the interaction cross-section.

The intensity effects in relativistic DLAs are mainly caused by wake fields created by the interaction of the particle with the surroundings. First studies of longitudinal intensity effects were already done by Schächter et al. in 2003 [37] and Hanuka et al. [38, 39, 40]. These studies are based on azimuthally symmetric dielectric-loaded waveguide as simplified model for DLA structures. However, it is to be expected that the wake fields of experimentally tested DLA structures differ strongly from these models. Furthermore, instabilities due to transverse wake fields could lead to particle loss much earlier than longitudinal effects. Therefore, estimating the maximum possible beam current for future applications of DLAs requires intense wake field studies of real DLA structures including longitudinal and transverse effects and the resulting beam dynamics.

I.2 Overview

The thesis is organized as follows: Chapter 1 discusses the fundamentals of accelerator physics starting with Maxwell's equations, followed by the basic concepts of particle beam dynamics and wake fields.

In Chapter 2 this theoretical framework is applied to the single electron motion in DLA structures. Section 2.1 presents the acceleration in such structures and Sec. 2.2 presents a beam confinement scheme. These sections are partly based on [31, 32, 41]. Section 2.3 on structure design and optimization is partly based on [29, 30, 32].

Wake fields are analyzed in Chapter 3. First, the applied simulation model is presented. Afterwards examples of longitudinal and transverse wake fields of different DLA structures are described. The results of this chapter are partly published in [42, 43].

Chapter 4 discusses an experiment performed at SwissFEL measuring the effects of the longitudinal wake field of a DLA structure on the energy spectrum of an electron beam and compares them to corresponding simulations. For this experiment, short DLA structures are used, which implies the particle distribution does not change within the interaction length.

The non-linear tracking tool called DLAtrack6D has been developed for beam dynamic studies [31]. This tool is introduced in Chapter 5 and tracking examples are shown, which are partly taken from [32, 43]. For the analysis of intensity effects, kicks by wake fields are added to DLAtrack6D as presented in [43].

Chapter 6 investigates wake field driven beam instabilities and intensity effects. A longitudinal effect known as Beam loading is analyzed in Sec. 6.1, where the results are published in [42]. The transverse effects are distinguished in two energy regimes. For high energies, i.e., a stiff bunch, the transverse beam breakup is studied in Sec. 6.2. For lower energies, the head tail instability may occur. A study of this instability in DLA structures is presented in Sec. 6.3. The discussion on both transverse effects is, in part, published in [43].

Finally, conclusions are drawn and an outlook for future work is given in the last chapter.

1 Fundamentals

This chapter summarizes the theoretical framework of this thesis. The basic principles, in particular Maxwell's equations and the Lorentz force are presented in Sec. 1.1. Section 1.2 introduces the single particle dynamics in a particle accelerator and Sec. 1.3 includes wake fields to the description of collective beam dynamics.

1.1 Maxwell's Equations

Maxwell's equations describe electromagnetics macroscopically by vector fields as

$$\nabla \times \vec{E}(\vec{r},t) = -\frac{\partial \vec{B}(\vec{r},t)}{\partial t} \tag{1.1a}$$

$$\nabla \times \vec{H}(\vec{r},t) = \frac{\partial \vec{D}(\vec{r},t)}{\partial t} + \vec{J}(\vec{r},t) \tag{1.1b}$$

$$\nabla \cdot \vec{D}(\vec{r},t) = \rho(\vec{r},t) \tag{1.1c}$$

$$\nabla \cdot \vec{B}(\vec{r},t) = 0, \tag{1.1d}$$

for any position $\vec{r} \in \Omega$, any volume $\Omega \subset \mathbb{R}^3$, and time $t \in \mathbb{R}$. In the relations 1.1, $\nabla \times \vec{F}$ and $\nabla \cdot \vec{F}$ denote the curl and the divergence of the vector field $\vec{F}$, respectively. The electric field strength $\vec{E}(\vec{r},t)$ and the electric displacement field $\vec{D}(\vec{r},t)$ of a linear and isotropic medium are coupled by the permittivity $\varepsilon(\vec{r})$ as $\vec{D}(\vec{r},t) = \varepsilon(\vec{r})\vec{E}(\vec{r},t)$ and the permeability $\mu(\vec{r})$ links the magnetic flux density $\vec{B}(\vec{r},t)$ to the magnetic field strength $\vec{H}(\vec{r},t)$ by $\vec{B}(\vec{r},t) = \mu(\vec{r})\vec{H}(\vec{r},t)$. Furthermore, $\rho(\vec{r},t)$ and $\vec{J}(\vec{r},t)$ denote the charge density and current density, respectively, where the current density is composed of three parts: the conduction current density $\vec{J}_\kappa(\vec{r},t)$ connected to the electric field strength by the conductivity $\kappa(\vec{r})$ through $\vec{J}_\kappa(\vec{r},t) = \kappa(\vec{r})\vec{E}(\vec{r},t)$, the convection current density $\vec{J}_\rho(\vec{r},t) = \rho(\vec{r},t)\,\vec{v}(\vec{r},t)$ considering free charges, and the externally imprinted source current density $\vec{J}_\mathrm{s}(\vec{r},t)$. Thus, it is $\vec{J} = \vec{J}_\kappa + \vec{J}_\rho + \vec{J}_\mathrm{s}$. Maxwell's equations were first given in this notation by Heaviside in 1892 [44], although they had already been postulated 27 years earlier by Maxwell [45, 46, 47].

In a vacuum, charge-free, and current-free space ($\rho(\vec{r},t)=0, \vec{J}(\vec{r},t)=0$), Maxwell's equations can be rewritten as homogeneous wave equations

$$\left(\frac{1}{c_0^2}\frac{\partial^2}{\partial t^2}-\nabla^2\right)\vec{E}(\vec{r},t)=0 \tag{1.2a}$$

$$\left(\frac{1}{c_0^2}\frac{\partial^2}{\partial t^2}-\nabla^2\right)\vec{B}(\vec{r},t)=0, \tag{1.2b}$$

where ∇^2 is the Laplace operator. The general solution of Eqs. 1.2 is a linear superposition of functions of the form $g\left(\omega t-\vec{k}\cdot\vec{r}\right)$. Therein the angular frequency ω and the wave vector $\vec{k}$ are coupled by the dispersion relation $\left|\vec{k}\right|=\omega/c_0$. The function g can be expressed by a Fourier integral

$$g\left(\omega t-\vec{k}\cdot\vec{r}\right)=\mathrm{Re}\left\{\int_0^\infty \underline{\Phi}(\omega)\exp\left(i\omega t-i\underline{\vec{k}}\cdot\vec{r}\right)\mathrm{d}\omega\right\}, \tag{1.3}$$

which can be interpreted as a superposition of plane waves propagating in the direction of the complex wave vector $\underline{\vec{k}}$. A real valued wave number describes a homogeneous plane wave, also called propagating wave. Evanescent waves with exponential decay from a surface or source are characterized by a purely imaginary wave number.

The Lorentz force, which acts on a charged particle due to electromagnetic fields, is given by

$$\vec{F}_L(\vec{r},t)=q\left[\vec{E}(\vec{r},t)+\vec{v}(\vec{r},t)\times\vec{B}(\vec{r},t)\right] \tag{1.4}$$

with the particle's charge q and velocity $\vec{v}$. Equation 1.4 shows that the electric field can act in the direction of the particle's motion and thus transfers energy, whereas the magnetic field acts perpendicular to the particle's motion only deflecting the particle without any change in energy. Newton's second law states that the rate of change of particle's momentum $\vec{p}=\gamma m_\mathrm{p}\vec{v}$ is directly proportional to the force,

$$\vec{F}(\vec{r},t)=\frac{\mathrm{d}\vec{p}(\vec{r},t)}{\mathrm{d}t}. \tag{1.5}$$

Therein, $\gamma=\left(1-\beta^2\right)^{-1/2}$ and $\beta=|\vec{v}|/c_0$ are the relativistic factors and m_p is the mass of the particle. Combining Eqs. 1.4 and 1.5, the motion of a particle in an electromagnetic field can be analyzed.

1.2 Particle Beam Dynamics

The position and motion of a particle in a particle accelerator is usually described in a co-moving coordinate system with respect to a reference or synchronous particle. Its ideal trajectory, which is determined by the design of the focusing and accelerating components, is termed (reference) orbit. The co-moving coordinate system is a Frenet-Serret frame [48, 49] following the reference orbit, i.e., the reference particle is placed in the origin of the co-moving coordinates (see Fig. 1.1). In the rest frame, the reference orbit is described by the longitudinal coordinate z. In the co-moving frame, the s-coordinate points in the direction tangentially to the reference orbit, while the x-coordinate is perpendicular to the orbit in the direction of its curvature and the y-coordinate completes the right-handed coordinate system. Usually, the x-coordinate is arranged as the horizontal direction, even if the curvature of the reference orbit is zero. An arbitrary particle can be described by a six-dimensional phase space vector

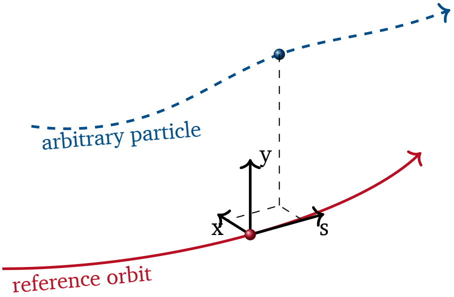

Figure 1.1: Sketch of the co-moving Frenet-Serret coordinate system.

$$\vec{r}_{\mathrm{p}}(z) = \begin{pmatrix} x \\ x' \\ y \\ y' \\ s \\ \delta \end{pmatrix}, \tag{1.6}$$

where $x' = dx/dz$ and $y' = dy/dz$ are the derivatives of the transverse coordinates with respect to z. The relative momentum deviation is given by $\delta = (p - p_0)/p_0$ with the momenta p and p_0 of the particle and the reference particle, respectively.

In an accelerator lattice, the change of the phase space vector can be described by a function, which depends on the initial phase space vector and the evolution of the reference particle. In a linear lattice, this function simplifies to a linear matrix multiplication

$\vec{r}_{\mathrm{p,f}} = M_{\mathrm{if}} \vec{r}_{\mathrm{p,i}}$, where the indices i and f indicate the initial and final phase space vectors, respectively. If the phase space planes are uncoupled, the transfer matrix M_{if} is block-diagonal and each plane can be treated separately as a two-dimensional phase space vector and a 2x2 transfer matrix. Transfer matrices for standard beam optics elements can, for example, be found in [50, ch. II.4].

In a conventional accelerator, the particles are confined by quadrupole magnets, which are focusing in one transverse plane and defocusing in the other plane. A combination of a focusing and a defocusing quadrupole magnet with drift sections in between provides net focusing and thus stable beam transport (a so-called FODO lattice). The focusing strength of such a quadrupole magnet is defined by $K = qB_0/(p_0 a)$, where B_0 is the magnetic field strength on the hyperbolic pole with a distance a to the beam axis and q is the electric charge of the particle with momentum p_0. Considering a particle in the co-moving coordinate system moving in a periodic magnetic quadrupole field of a FODO lattice, the corresponding equation of transverse motion is given by Hill's equation

$$u'' + K(z)u = 0, \tag{1.7}$$

where $K(z)$ is periodic with the period length L, i.e., $K(z) = K(z+L)$, and u is one of the transverse coordinates x or y. The second-order linear ordinary differential equation is named after the astronomer George William Hill, who introduced it in 1886 [51]. There are two independent solutions of this differential equation of the form

$$u_1(z) = w(z)\exp(i\mu z/L) \tag{1.8a}$$

$$u_2(z) = w^*(z)\exp(-i\mu z/L), \tag{1.8b}$$

where the function $w(z)$ is unique and periodic in z with period L, $w^*(z)$ is the complex conjugate to $w(z)$, and μ is defined by

$$\cos(\mu) = \frac{1}{2}\mathrm{Tr}\left[M_{\mathrm{if},u}(z+L|z)\right] \tag{1.9}$$

with the two-dimensional transfer matrix $M_{\mathrm{if},u}$. The trace of the tranfer matrix and thus the coefficient μ is independent of z. Note that the solution remains periodic and finite for

$$\mathrm{Tr}\left[M_{\mathrm{if},u}(z+L|z)\right] < 2, \tag{1.10}$$

which provides a stability criterion for beam confinement.

The particle in a FODO lattice moves along an ellipse in phase space whose area is $\pi\epsilon_u$ with the single particle emittance ϵ_u and whose orientation is described by the Twiss or Courant Snyder parameters $\hat{\alpha}_u$, $\hat{\beta}_u$, and $\hat{\gamma}_u$ [52] (see Fig. 1.2). A solution

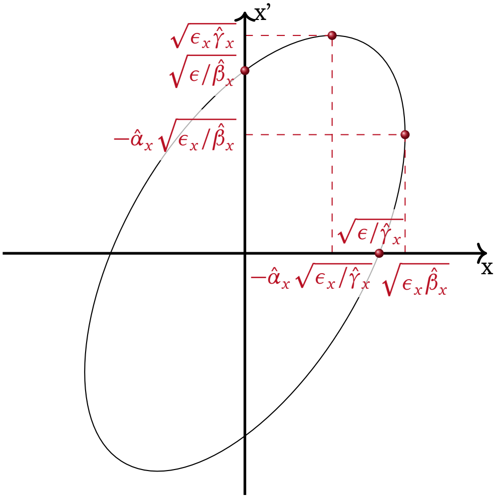

Figure 1.2: Phase space ellipse with Courant Snyder parameters.

of Hill's equation 1.7 formulated with Twiss parameters can be written as transverse betatron motion [53]

$$u(z) = \sqrt{\epsilon_u \hat{\beta}_u(z)} \cos\left(\psi_u(z) - \psi_u(z_0)\right), \tag{1.11}$$

which is equivalent to a linear superposition of the solutions in Eq. 1.8 with $w_u = \sqrt{\epsilon_u \hat{\beta}_u}$. Inserting Eq. 1.11 into Eq. 1.7 and equating coefficients of cosine and sine on either side of the resulting equation, leads to

$$\hat{\beta}_u' \psi_u' + \hat{\beta}_u \psi_u'' = 0 \tag{1.12a}$$

$$\frac{1}{2}\hat{\beta}_u \hat{\beta}_u'' + K\hat{\beta}_u^2 - \frac{1}{4}\hat{\beta}_u'^2 - \hat{\beta}_u^2 \psi_u'^2 = 0 \tag{1.12b}$$

Integrating Eq. 1.12a, the phase advance of the betatron oscillation after the distance z is found as

$$\psi_u(z) - \psi_u(z_0) = \int_{z_0}^{z} \frac{1}{\hat{\beta}_u(\tilde{z})} d\tilde{z}. \tag{1.13}$$

This results in a phase advance of $\mu_u = \psi_u(z+L) - \psi_u(z) = \int_z^{z+L} 1/\hat{\beta}_u(\tilde{z})\, d\tilde{z}$ for the lattice period L. Substituting Eq. 1.13 into Eq. 1.12b, yields for the Twiss beta function

$$\frac{1}{2}\hat{\beta}_u \hat{\beta}_u'' + K\hat{\beta}_u^2 - \frac{1}{4}\hat{\beta}_u'^2 = 1. \tag{1.14}$$

The remaining Twiss parameters are given by $\hat{\alpha}_u = -\frac{1}{2}\hat{\beta}_u'$ and $\hat{\gamma}_u = \left(1+\hat{\alpha}_u^2\right)/\hat{\beta}_u$. With these parameters, the single particle emittance is

$$\epsilon_u = \hat{\gamma}_u u^2 + 2\hat{\alpha}_u u u' + \hat{\beta}_u u'^2. \tag{1.15}$$

Analogous to the phase space vector, the evolution of the Twiss parameters in a linear lattice can be described by a matrix multiplication

$$\begin{pmatrix} \hat{\beta}_u \\ \hat{\alpha}_u \\ \hat{\gamma}_u \end{pmatrix}_{\mathrm{f}} = \begin{pmatrix} m_{11}^2 & -2m_{11}m_{12} & m_{12}^2 \\ -m_{11}m_{21} & m_{12}m_{21}+m_{11}m_{22} & -m_{12}m_{22} \\ m_{21}^2 & -2m_{21}m_{22} & m_{22}^2 \end{pmatrix} \begin{pmatrix} \hat{\beta}_u \\ \hat{\alpha}_u \\ \hat{\gamma}_u \end{pmatrix}_{\mathrm{i}}, \tag{1.16}$$

where m_{ij} are the entries of the two-dimensional transfer matrix $M_{\mathrm{if},u}$ and the indices i and f indicate the initial and final Twiss parameters, respectively. A stable solution, i.e., a vector of Twiss parameters, which changes periodically with the lattice period, can be calculated as eigenvector of the transfer matrix in Eq. 1.16 to the eigenvalue 1.

So far, we have described the motion of a single particle. However, a particle beam is usually an ensemble of particles distributed in the phase space. The rms beam emittance is then given by

$$\epsilon_{u,\mathrm{rms}} = \sqrt{\sigma_u^2\sigma_{u'}^2 - \sigma_{uu'}^2}, \tag{1.17}$$

where σ_u and $\sigma_{u'}$ are the rms beam widths and $\sigma_{uu'}$ is the correlation. The rms emittance is equal to the phase space ellipse defined by the Twiss parameters of the particle with rms amplitude. The beam envelope, which describes the local beam size, is given by

$$w_u = \sqrt{\epsilon_{u,\mathrm{rms}}\hat{\beta}_u}. \tag{1.18}$$

Using Eq. 1.14, the envelope as function of the lattice is determined by the differential equation

$$w_u'' + K w_u - \frac{\epsilon_{u,\mathrm{rms}}}{w_u^3} = 0. \tag{1.19}$$

Due to Liouville's theorem [54], the beam emittance stays constant in a linear beam transport lattice. However, Liouville's theorem requires the use of canonical variables, i.e., the transverse momentum p_u. If the angle $u' = du/dz = p_u/p$ is used instead, the beam emittance, often called geometric emittance, descreases during acceleration. Instead, the product of particle momentum and beam emittance remains constant leading to the definition of the normalized emittance as

$$\epsilon_{\mathrm{n}} = \beta\gamma\epsilon, \tag{1.20}$$

which is an invariant also in case of acceleration.

The longitudinal motion of a particle in an accelerator describes the interaction of the particle with an electric field. In conventional accelerators, this is mostly the rf electric field in the cavities, which produces a cosine potential

$$V_{\mathrm{rf}} = V_0 \cos\left(\frac{\omega_{\mathrm{rf}} s}{c_0} + \varphi_0\right) = V_0 \left[\cos\left(\frac{\omega_{\mathrm{rf}} s}{c_0}\right)\cos(\varphi_0) - \sin\left(\frac{\omega_{\mathrm{rf}} s}{c_0}\right)\sin(\varphi_0)\right]. \tag{1.21}$$

The frequency ω_{rf} has to be synchronized to the velocity of the reference particle $\beta_0 c_0$. We can consider two accelerating cavities separated by a distance λ_z. For continuous acceleration, the phase of the rf fields in each of the cavities must reach the same specific value at the time of arrival of the reference particle. This can be described with the synchronicity condition $\omega_{\mathrm{rf}} = 2\pi c_0 m \beta_0/\lambda_z$, which is known as Wideröe's condition [55], with m as an integer called harmonic number. The specific phase of the reference particle φ_0 with respect to the electric field is called synchronous phase. In order to formulate the longitudinal equation of motion, the derivation of energy difference and distance to the reference particle in one period with period duration $T_0 = \lambda_z/c_0$ can be described by

$$\frac{\partial \Delta E}{\partial t} = \frac{q}{T_0} V_0 \left[\cos\left(\frac{\omega_{\mathrm{rf}} s}{c_0} + \varphi_0\right) - \cos(\varphi_0)\right] \tag{1.22a}$$

$$\frac{\partial s}{\partial t} = -\frac{c_0}{\beta_0^2 \gamma_0^3 E_0} \Delta E. \tag{1.22b}$$

Derivating Eq. 1.22b and inserting Eq. 1.22a yields the equation of motion

$$\frac{\partial^2 s}{\partial t^2} = -\frac{c_0 q}{\beta_0^2 \gamma_0^3 T_0 E_0} V_0 \left[\cos\left(\frac{\omega_{\mathrm{rf}} s}{c_0} + \varphi_0\right) - \cos(\varphi_0)\right]. \tag{1.23}$$

If $\omega_{\mathrm{rf}} s/c_0 \ll 1$, which is fulfilled for small s, Eq. 1.23 can be linearized in s. Using the trigonometrical relation in Eq. 1.21 as $\sin(\omega_{\mathrm{rf}} s/c_0) \approx \omega_{\mathrm{rf}} s/c_0$ and $\cos(\omega_{\mathrm{rf}} s/c_0) \approx 1$ leads to the differential equation of a simple harmonic oscillator $\partial^2 s/\partial t^2 s + \omega_s^2 s = 0$ with

$$\omega_s = \sqrt{-\frac{\omega_{\mathrm{rf}}\, q}{\beta_0^2 \gamma_0^3 T_0 E_0} V_0 \sin(\varphi_0)}. \tag{1.24}$$

This angular frequency ω_s (Eq. 1.24) is known as synchrotron frequency. Stable oscillation of a particle with charge $q < 0$ is therefore possible for $0 < \varphi_0 < \pi$. For particles with larger s, Eq. 1.22 can be solved numerically. In the longitudinal phase space, the boundary between the area of all particles with a stable oscillation around the reference particle and the unstable particles is called separatrix. The separatrix encloses the bucket with all stable particle trajectories. The points, where a particle would remain for all times, if it is there at any time, are called fixed points. The crossings of two branches of the separatrix are unstable fixed points, also called hyperbolic fixed points, because nearby trajectories take this form. A stable fixed point is located at the phase space coordinates of the reference particle. Such a fixed point is also called elliptic, since nearby orbits take the form of ellipses. Phase space diagrams for two exemplary synchronous phases are shown in Fig. 1.3.

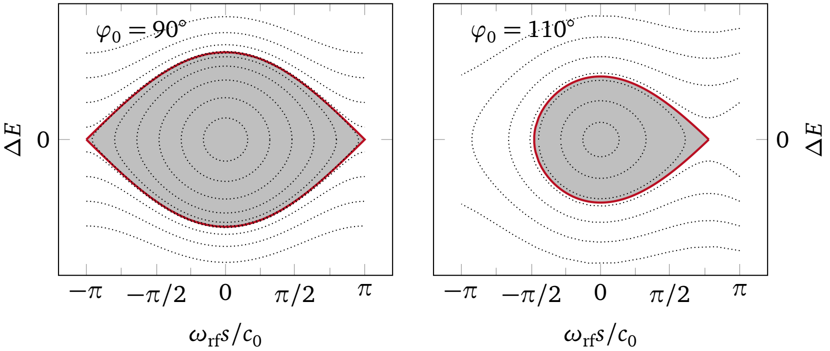

Figure 1.3: Longitudinal phase space diagrams for two different synchronous phases. The separatrix (red line) encloses the bucket (gray area). The dashed lines show possible stable or unstable particle trajectories.

1.3 Wake Field

So far, we have only considered a beam of non-interacting particles moving in the electromagnetic fields. For a high intensity beam, the electromagnetic fields generated by the beam has to be taken into consideration as well. At a velocity close to the speed of light, the electromagnetic field of a point charge particle is Lorentz contracted into a thin disk, which is perpendicular to the direction of motion. In the limit $v \rightarrow c_0$, the disk becomes a delta distribution with an electric field radially outward from the particle and a magnetic field perpendicular to electric field and direction of motion. Due to causality, these source fields do not affect particles in front of or behind the particle which generates the field. Nevertheless, reflections of the source fields on the surface of

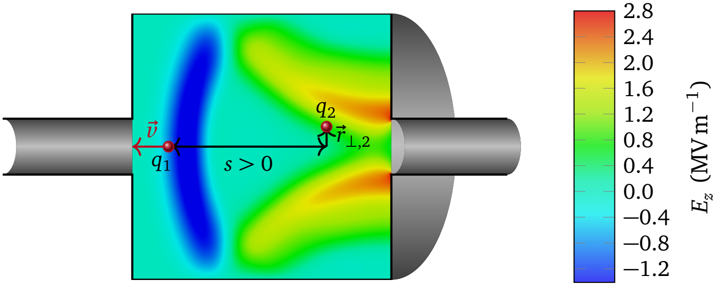

Figure 1.4: Longitudinal electric field of a source particle q_1 passing from right to left through a cylindrical cavity. The longitudinal wake function is the integrated Lorentz force of this field acting on a test particle q_2 at a constant distance s behind the source particle with transverse offset $\vec{r}_{\perp,2}$ ($\vec{r}_{\perp,1}=0$).

accelerator components or image currents on those surfaces can lead to electromagnetic fields behind the relativistic particle.

Considering a test particle with charge q_2 following a source particle with charge q_1 at a distance s with $v_1 = v_2 \approx c_0$, the fields generated by the source particle interacting with its surroundings apply a Lorentz force (cf. Eq. 1.4) to the test particle. Note that $s>0$ means that the test particle moves behind the source particle (see Fig. 1.4). The resulting momentum change of the test particle can be calculated as an time integral over the Lorentz force or an integral of the Lorentz force over the longitudinal coordinate z. The Lorentz force at the longitudinal position z is then evaluated at the corresponding time $t=(z+s)/v_2$. This leads to the definition of the wake function [56, 57]

$$\vec{w}\left(\vec{r}_{\perp,1},\vec{r}_{\perp,2},s\right) = \frac{1}{q_1 q_2}\int_{-\infty}^{\infty} \vec{F}_L\left(\vec{r}_{\perp,2},z,t=\frac{z+s}{v_2}\right)\mathrm{d}z \tag{1.25a}$$

$$= \frac{1}{q_1}\int_{-\infty}^{\infty} \vec{E}\left(\vec{r}_{\perp,2},z,t=\frac{z+s}{v_2}\right) + \vec{v}_2\times\vec{B}\left(\vec{r}_{\perp,2},z,t=\frac{z+s}{v_2}\right)\mathrm{d}z. \tag{1.25b}$$

Due to the normalization, the wake function is independent of the particles' charge. Mathematically, the wake function resembles a Green's function. Hence, the wake potential of a beam can be determined by a convolution with the charge distribution,

$$\vec{W}\left(\vec{r}_{\perp,2},s\right) = \int_{-\infty}^{\infty}\int_{-\infty}^{\infty}\int_{-\infty}^{\infty} \vec{w}\left(\vec{r}_{\perp,1},\vec{r}_{\perp,2},s-\tilde{s}\right)\lambda\left(\tilde{s},\vec{r}_{\perp,2}\right)\mathrm{d}\tilde{s}\,\mathrm{d}^2\vec{r}_{\perp,1}, \tag{1.26}$$

where the charge distribution is normalized as

$$\int_{-\infty}^{\infty}\int_{-\infty}^{\infty}\int_{-\infty}^{\infty} \lambda(s)\,\mathrm{d}s\,\mathrm{d}^2\vec{r}_{\perp,1} = 1. \tag{1.27}$$

In order to formulate the integral in Eq. 1.26, we apply the following two approximations (see also e.g. [58]):

1. **Rigid beam approximation:** The beam passes a device which creates the wake field rigidly. This means the wake field does not affect the motion of the particles within the device. The change of the particles' velocity by energy gain or loss is negligible for relativistic particles and the transverse motion, e.g., betatron motion, can also be neglected.

2. **Impulse approximation:** Although the wake field is continuously acting on the test particle, the effect is combined to an integrated momentum change as the test particle leaves the device. We call this the wake kick.

Therefore, the transverse positions of the source and test particles and also the longitudinal distance between the particles stay constant. We can distinguish the effects by the wake field in two regimes: The transient regime, which is dominant for small distances s, and the resonant regime for distances much larger than the bunch length. Accordingly, the former is called short-range wake and the latter is called long-range wake.

Due to the longitudinal wake potential, there is a change of particles' energy in addition to the change by an external potential. This leads to a so-called potential well distortion, which depends on the wake field and, thus, on the bunch shape and charge. The total energy loss of a bunch by the wake field is given by $\Delta E = q_{\mathrm{bunch}}^2 k_{\mathrm{loss}}$ with the loss factor

$$k_{\mathrm{loss}} = \int_{-\infty}^{\infty} \lambda(s)\, W_{||}(s)\, \mathrm{d}s. \tag{1.28}$$

In the accelerating potential, the energy gain of a bunch depends, however, linearly on the bunch charge. Therefore, there is a bunch intensity at which energy loss by the wake field and energy gain by the external field are equal. At this intensity and above acceleration of the bunch is not possible. This defines the beam loading bunch intensity limit [59].

The fundamental theorem of beam loading states that a point-like particle sees one-half of its transient beam-loading voltage, when it crosses a cavity. This can be proven by energy conservation if two particles pass the cavity with a distance of half the oscillation period in the cavity or if the first particle passes the cavity again when the cavity phase has changed by an arbitrary angle (see for example [56, 60, 59]). The theorem implies that the longitudinal wake function does not vanish in the limit $s \rightarrow 0$.

However, the transverse wake function for a point-line particle in the limit $s \rightarrow 0$ is zero. This means that the transverse wake does not act on the generating particle. It only leads to a deflection of subsequent particles. Moreover, a bunch distribution is not deflected as a whole but only the head of the bunch deflects the tail.

If the wake function is only known in one plane, longitudinal or transverse, the wake function in the other plane can be calculated analytically. For this, we can use Maxwell's equation 1.1a to obtain $\vec{e}_z \times \partial \vec{B}/\partial t = \partial \vec{E}_\perp/\partial z - \nabla_\perp E_{||}$. The partial differentiation of the transverse component of Eq. 1.25 with respect to s using $\partial s/\partial t = v_2$ thus yields [56]

$$\begin{aligned}
\frac{\vec{w}_\perp}{\partial s} &= \frac{1}{q_1}\int_{-\infty}^{\infty}\left[\frac{1}{v_2}\frac{\partial}{\partial t}\left(\vec{E} + \vec{v}_2 \times \vec{B}\right)\right]_\perp \mathrm{d}z && (1.29a)\\
&= \frac{1}{q_1}\int_{-\infty}^{\infty}\left(\frac{1}{v_2}\frac{\partial \vec{E}_\perp}{\partial t} + \vec{e}_z \times \frac{\partial \vec{B}}{\partial t}\right)\mathrm{d}z && (1.29b)\\
&= -\frac{1}{q_1}\int_{-\infty}^{\infty}\left(\frac{1}{v_2}\frac{\partial \vec{E}_\perp}{\partial t} + \frac{\partial \vec{E}_\perp}{\partial z}\right)\mathrm{d}z - \frac{1}{q_1}\int_{-\infty}^{\infty}\nabla_\perp E_{||}\mathrm{d}z && (1.29c)\\
&= -\frac{1}{q_1}\int_{-\infty}^{\infty}\frac{d\vec{E}_\perp}{dz}\mathrm{d}z + \frac{1}{q_1}\int_{-\infty}^{\infty}\nabla_\perp E_{||}\mathrm{d}z. && (1.29d)
\end{aligned}$$

Therein, we have explicitly used the rigid beam approximation, i.e., $\vec{v}_2 = v_2\vec{e}_z = \partial z/\partial t = \text{const}$. Furthermore, we assume that the fields vanish for $z = \pm\infty$. Thus, the first integral of Eq. 1.29d vanishes and the second integral can be written as

$$\begin{aligned}
\frac{\partial \vec{w}_\perp}{\partial s} &= -\frac{1}{q_1}\nabla_\perp\int_{-\infty}^{\infty} E_{||}\mathrm{d}z && (1.30a)\\
&= -\nabla_\perp w_{||} && (1.30b)
\end{aligned}$$

By convolution, Eq. 1.30 holds also for the wake potential. Equation 1.30 is often referred to as Panofsky-Wenzel theorem, even though Panofsky and Wenzel have derived a relationship between longitudinal and transverse electromagnetic forces in a more general manner [61].

High beam intensities imply strong wake fields. The action of these fields back on the beam leads to instabilities and therefore limits the possible beam intensity of a particle accelerator. Intensity effects caused by wake fields can be divided into single-bunch effects by the short-range wake field and multi-bunch effects by the long-range wake field. For conventional accelerators intensity effects have already been studied in great detail, both theoretically and experimentally. Intensity effects in DLA structures have not yet been analyzed in detail, and this thesis provides a first theoretical investigation of intensity limits due to wake fields.

2 Single Particle Dynamics in Dielectric Laser Accelerator Structures

The complex particle dynamics in the evanescent fields of Dielectric Laser Accelerator (DLA) structures represent a major challenge for the analysis and the design of an accelerator lattice based on DLA structures. The single particle dynamics in conventional accelerators have been studied for decades. The studies presented in this thesis are based on the notation introduced in the context of conventional accelerators to benefit from conventional accelerator literature. In Sec. 2.1, energy gain and transverse forces in DLA grating periods are derived by using a spatial Fourier series. This leads to a potential comparable to that of a conventional magnetic quadrupole accelerator lattice and Hill's equations describing the particle motion. Furthermore, it enables the transfer of focusing concepts, especially the Alternating Phase Focusing (APF) scheme, to DLA structures, which is presented in Sec. 2.2. Section 2.3 summarizes the different design and optimization tasks for single DLA periods and full APF lattices based also on similar methods used in the lattice design of conventional accelerators.

2.1 Acceleration

In order to analyze the single particle dynamics in a DLA structure, we consider one DLA cell as unit cell and define a coordinate system such that the reference particle propagates in positive z-direction and the laser, which is z-polarized, propagates in y-direction. The structure is assumed to be invariant in x-direction. Following [31], the energy gain of a particle with charge q and velocity v in one DLA cell of length λ_z is

$$\Delta E_\mathrm{p}(x,y;s) = q\int_{-\lambda_z/2}^{\lambda_z/2} E_z\left(x,y,z;t=(z+s)/v\right)\mathrm{d}z \tag{2.1a}$$

$$= q\int_{-\lambda_z/2}^{\lambda_z/2} \mathrm{Re}\left\{\underline{E}_z(x,y,z)\exp\left(i\frac{\omega}{v}(z+s)\right)\right\}\mathrm{d}z \tag{2.1b}$$

with $\omega = 2\pi c_0/\lambda_0$ and the longitudinal electric laser field $\underline{E}_z(x,y,z)$ in the DLA cell. The phase shift between laser phase and particle injection phase is described by the distance s. Due to the z-periodicity, the laser field can be written in a spatial Fourier series

$$\underline{E}_z(x,y,z) = \sum_{m=-\infty}^{\infty} \underline{e}_m(x,y) \exp\left(-im\frac{2\pi}{\lambda_z}z\right) \tag{2.2}$$

with the spatial harmonics

$$\underline{e}_m(x,y) = \frac{1}{\lambda_z}\int_{-\lambda_z/2}^{\lambda_z/2} \underline{E}_z(x,y,z) \exp\left(im\frac{2\pi}{\lambda_z}z\right)\mathrm{d}z. \tag{2.3}$$

Substituting Eq. 2.2 in Eq. 2.1b yields the energy gain

$$\Delta E_\mathrm{p}(x,y;s) = q\mathrm{Re}\left\{\exp\left(\frac{2\pi is}{\beta\lambda_0}\right)\sum_{m=-\infty}^{\infty}\underline{e}_m(x,y)\,\lambda_z \mathrm{sinc}\left(\frac{\lambda_z}{\beta\lambda_0}-m\right)\right\}. \tag{2.4}$$

If the argument of the sinc function in Eq. 2.4 is non-integer, the energy gain averages to zero, if it is integer other than zero, it directly vanishes. Therefore, only one summand does not vanish, which fulfills the synchronicity condition

$$\lambda_z = m\beta\lambda_0. \tag{2.5}$$

Equation 2.5 is well known from conventional linear accelerators as Wideröe's condition [55]. This simplifies the energy gain to

$$\Delta E_\mathrm{p}(x,y;s) = q\lambda_z\mathrm{Re}\left\{\exp\left(\frac{2\pi is}{\beta\lambda_0}\right)\underline{e}_m(x,y)\right\} \tag{2.6a}$$

$$= q\lambda_z\left|\underline{e}_m(x,y)\right|\cos\left(\frac{2\pi s}{\beta\lambda_0} + \arg\left(\underline{e}_m(x,y)\right)\right). \tag{2.6b}$$

The longitudinal dependence of the energy gain is thus completely described analytically. The transverse dependence can be determined by the dispersion relation of the synchronous mode. Due to the invariance of the structure in x-direction, the wave number in x-direction is $k_x = 0$. The spatial harmonic is therefore independent of x, i.e., $\underline{e}_m(x,y) = \underline{e}_m(y)$. A description for tilted gratings (periodic in x-direction), where $k_x \neq 0$, can be found in [31]. Furthermore, we have $k_z = \omega/(\beta c_0)$ and $k = \omega/c_0$. This leads to

$$k_y = \pm\sqrt{k^2 - k_z^2} = \pm\frac{\omega}{c_0}\sqrt{1-\beta^{-2}} = \pm\frac{i\omega}{\beta\gamma c_0}, \tag{2.7}$$

which describes the evanescent decay of the near field on the DLA structure. Without loss of generality we choose the positive solution of Eq. 2.7 for the following. Thus, the transverse dependence of the spatial harmonic after a single grating (at $y = g/2$) is

$$\underline{e}_m(y) = \underline{e}_m^0 \exp\left(-ik_y y\right) = \underline{e}_m^0 \exp\left(\frac{\omega y}{\beta\gamma c_0}\right) \tag{2.8}$$

with $\underline{e}_m^0 = \underline{e}_m(y=0)$. We add now a second grating with distance g to the first grating (at $y = -g/2$) and a second laser. The laser propagates in negative y-direction with the same frequency and peak field as the first laser, i.e., $\left|\underline{e}_{m,1}^0\right| = \left|\underline{e}_{m,2}^0\right|$, but arbitrary phase difference. This results in

$$\underline{e}_m(y) = \underline{e}_{m,1}^0 \exp\left(\frac{\omega y}{\beta\gamma c_0}\right) + \underline{e}_{m,2}^0 \exp\left(-\frac{\omega y}{\beta\gamma c_0}\right) \tag{2.9a}$$

$$\begin{aligned} &= \left|\underline{e}_{m,1}^0\right| \left\{ \left[\exp\left(i \arg\left(\underline{e}_{m,1}^0\right)\right) + \exp\left(i \arg\left(\underline{e}_{m,2}^0\right)\right)\right] \cosh\left(\frac{\omega y}{\beta\gamma c_0}\right) \right. \\ &\quad \left. + \left[\exp\left(i \arg\left(\underline{e}_{m,1}^0\right)\right) - \exp\left(i \arg\left(\underline{e}_{m,2}^0\right)\right)\right] \sinh\left(\frac{\omega y}{\beta\gamma c_0}\right) \right\}. \end{aligned} \tag{2.9b}$$

The spatial harmonic is therefore a superposition of a hyperbolic sine and a hyperbolic cosine depending on the phase difference between the two incident laser fields. There are two special cases in which one of the summands disappears: in case of equal laser phase, the second summand vanishes and the first summand simplifies to

$$\underline{e}_m(y) = \underline{e}_m^0 \cosh\left(\frac{\omega y}{\beta\gamma c_0}\right) \tag{2.10}$$

with $\underline{e}_m^0 = 2\underline{e}_{m,1}^0$. That means, that the spatial harmonic is symmetric to the center of the gap and there is thus no transverse kick for particles at the center. This is the usually used accelerating mode. If the laser phase differs by π, Eq. 2.10 changes to [62]

$$\underline{e}_m(y) = \underline{e}_m^0 \sinh\left(\frac{\omega y}{\beta\gamma c_0}\right). \tag{2.11}$$

Since the hyperbolic sine is an odd function, the longitudinal kick is antisymmetric to the center of the gap and disappears in the center. This mode can be used for streaking experiments [23].

So far, only the evanescent decay of the near field on the side of the grating has been considered, where the corresponding laser is incident. However, reflections on the opposite side of the dielectric grating are also possible. We describe the reflections on the grating surface by a reflection coefficient r. The reflections of the evanescent wave from one side of the grating occur at a distance g on the other side of the gap. The reflected wave travels back through the gap until it is reflected again. The spatial harmonic of the first evanescent wave from one side and one laser is given by Eq. 2.8. After the first reflection, the spatial harmonic of this wave is

$$\underline{e}^{r}_{m,1}(y) = r\underline{e}^{0}_{m,1}\exp\left(-\frac{\omega}{\beta\gamma c_0}[y+g]\right). \tag{2.12}$$

Summing up all possible reflections, the result for the spatial harmonics is

$$\begin{aligned} \underline{e}_{m}(y) = &\sum_{n=0}^{\infty} r^{n}\underline{e}^{0}_{m,1}\exp\left(\frac{\omega}{\beta\gamma c_0}\left[(-1)^{n}y - ng\right]\right) \\ &+\sum_{n=0}^{\infty} r^{n}\underline{e}^{0}_{m,2}\exp\left(-\frac{\omega}{\beta\gamma c_0}\left[ng + (-1)^{n}y\right]\right). \end{aligned} \tag{2.13}$$

The geometric series in Eq. 2.13 yields

$$\begin{aligned} \underline{e}_{m}(y) = &\frac{1}{1 - r^{2}\exp\left(-\frac{2\omega g}{\beta\gamma c_0}\right)}\left\{\left[\underline{e}^{0}_{m,1} + r\underline{e}^{0}_{m,2}\exp\left(-\frac{\omega g}{\beta\gamma c_0}\right)\right]\exp\left(\frac{\omega y}{\beta\gamma c_0}\right)\right. \\ &\left.+\left[r\underline{e}^{0}_{m,1}\exp\left(-\frac{\omega g}{\beta\gamma c_0}\right) + \underline{e}^{0}_{m,2}\right]\exp\left(-\frac{\omega y}{\beta\gamma c_0}\right)\right\}. \end{aligned} \tag{2.14}$$

Equation 2.14 has the same dependence on y as Eq. 2.9a and, thus, can be treated in the same way as a superposition of a hyperbolic sine and a hyperbolic cosine. A similar formulation can be found in the supplemental material of [23]. The spatial harmonics in the center of the gap must be calculated numerically [27, 28, 29, 30, 31, 62]. For a symmetric double-sided grating, the evaluation of the spatial harmonics in the center already includes possible reflections and Eq. 2.9 applies.

In the following we will concentrate on the case of equal laser phase. This allows particle acceleration in the center of the channel, which becomes clear by inserting Eq. 2.10 into Eq. 2.6. In this case, the energy gain is

$$\Delta E_{\mathrm{p}}(y,s) = q\lambda_{z}\left|\underline{e}^{0}_{m}\right|\cosh\left(\frac{\omega y}{\beta\gamma c_0}\right)\cos\left(\frac{2\pi s}{\beta\lambda_0} + \arg\left(\underline{e}^{0}_{m}\right)\right). \tag{2.15}$$

The argument of the cosine in Eq. 2.15 is only a phase shift to the laser phase with an additional constant offset by the argument of the spatial harmonic. It can be redefined as a phase φ_0 of a reference or synchronous particle regarding the accelerating phase in the structure, i.e., $\varphi_0 = 180°$ means on-crest acceleration, and a distance s between the reference particle and an arbitrary particle in a bunch. Instead of the energy gain per particle per cell, we can additionally consider the change of the energy difference between the arbitrary particle and the reference particle,

$$
\begin{aligned}
\Delta E\left(y,s\right) &= \Delta E_{\mathrm{p}}\left(y, s+\frac{\beta\lambda_0}{2\pi}\left[\varphi_0-\arg\left(\underline{e}_m^0\right)\right]\right) \\
&\quad -\Delta E_{\mathrm{p},0}\left(0, \frac{\beta\lambda_0}{2\pi}\left[\varphi_0-\arg\left(\underline{e}_m^0\right)\right]\right) && \text{(2.16a)} \\
&= q\lambda_z\left|\underline{e}_m^0\right|\left[\cosh\left(\frac{\omega y}{\beta\gamma c_0}\right)\cos\left(\frac{2\pi s}{\beta\lambda_0}+\varphi_0\right)-\cos\left(\varphi_0\right)\right]. && \text{(2.16b)}
\end{aligned}
$$

Note that the reference phase is not defined regarding the laser phase. As described above, it is defined by the accelerating phase in the structure, that means, with a constant offset by the argument of the spatial harmonic. This allows to follow the phase convention in conventional linear accelerators (cf. Eq. 1.21).

The transverse forces in one DLA cell can be obtained by using the Panofsky-Wenzel theorem [61] as [31, 32]

$$
\begin{aligned}
\Delta\vec{p}_\perp\left(y,s\right) &= -\int \mathrm{d}s\nabla_\perp\Delta p_{||}\left(y,s\right) && \text{(2.17a)} \\
&= -\frac{q\lambda_z\left|\underline{e}_m^0\right|}{\beta c_0}\nabla_\perp\left[\frac{\beta\lambda_0}{2\pi}\cosh\left(\frac{\omega y}{\beta\gamma c_0}\right)\sin\left(\frac{2\pi s}{\beta\lambda_0}+\varphi_0\right)-s\cos\left(\varphi_0\right)\right] && \text{(2.17b)} \\
&= -\frac{2\pi q m}{\omega\gamma}\left|\underline{e}_m^0\right|\sinh\left(\frac{\omega y}{\beta\gamma c_0}\right)\sin\left(\frac{2\pi s}{\beta\lambda_0}+\varphi_0\right)\vec{e}_y, && \text{(2.17c)}
\end{aligned}
$$

where the energy momentum differential $\Delta p_{||}=\Delta E/\left(\beta c_0\right)$ and Eq. 2.16 are used. The derivation of Eq. 2.17a is similar to Eq. 1.29. However, the integral limits are the DLA cell boundaries, where the fields fulfill a periodic boundary condition. Equations 2.16 and 2.17c show that the motion in the transverse and longitudinal plane is coupled. Based on the relations $\Delta p_y/\Delta t \approx \dot{p}_y = -\partial V/\partial y$ with $\Delta t = \lambda_0/c_0$ and $\Delta E/\left(\beta\lambda_0\right) = \dot{\Delta p}_{||} = \partial V/\partial s$, the integration of these two equations yields the potential

$$
V_m\left(y,s\right) = qm\left|\underline{e}_m^0\right|\left[\frac{\beta\lambda_0}{2\pi}\cosh\left(\frac{\omega y}{\beta\gamma c_0}\right)\sin\left(\frac{2\pi s}{\beta\lambda_0}+\varphi_0\right)-s\cos\left(\varphi_0\right)\right]. \tag{2.18}
$$

For a particle with a small transverse displacement from the beam axis, $\omega y/\left(\beta\gamma c_0\right) \ll 1$, and a small distance from the reference particle, $2\pi s/\left(\beta\lambda_0\right) \ll 1$, the potential (Eq. 2.18) can be expanded to second order omitting constant terms. This results in the potential of a two-dimensional harmonic oscillator,

$$
V_m\left(y,s\right) = \frac{1}{2}\frac{q\lambda_z}{2\pi}\left|\underline{e}_m^0\right|\sin\left(\varphi_0\right)\left[\left(\frac{\omega y}{\beta\gamma c_0}\right)^2-\left(\frac{2\pi s}{\beta\lambda_0}\right)^2\right]. \tag{2.19}
$$

As in the linearized motion of a conventional linear accelerator (see Eq. 1.7), the equations of motion are Hill's equations,

$$y'' + K_m y = 0 \tag{2.20a}$$

$$s'' - K_m s = 0, \tag{2.20b}$$

with

$$K_m = \frac{2\pi m q}{\beta^3 \lambda_0 m_e \gamma^3 c_0^2} \left|\underline{e}_m^0\right| \sin\left(\varphi_0\right), \tag{2.21}$$

which lead to a decoupling of the coupled non-linear motion. The traceability to Hill's equations means that all procedures of conventional accelerator physics, such as matching using Twiss parameters, can also be used in DLA structures, at least in the linearized case. However, only the equations for the synchronous m are relevant due to the synchronicity condition (Eq. 2.5). Furthermore, the DLA cell length has to be adjusted to the velocity of the reference particle. The energy of the reference particle after passing N DLA cells is given by

$$E_{\text{kin}}\left(N\right) = E_{\text{kin},0} + q \sum_{n=1}^{N} \lambda_z^{(n)} \left|\underline{e}_m^{0(n)}\right| \cos\left(\varphi_0^{(n)}\right) \tag{2.22}$$

If the synchronous phase φ_0 is chosen such that the reference particle will gain (or lose) energy, the cell length has to be changed along the structure according to the acceleration ramp as

$$\lambda_z^{(n+1)} - \lambda_z^{(n)} = \lambda_0 \left(\beta^{(n+1)} - \beta^{(n)}\right) = \frac{q \lambda_0^2}{m_e c_0^2 \left(\gamma^{(n)}\right)^3} \left|\underline{e}_m^{0(n)}\right| \cos\left(\varphi_0^{(n)}\right). \tag{2.23}$$

Such a grating with increasing cell length is referred to as chirped grating in the literature. A chirped grating is designed by an iterative process [30]: the injection velocity of the reference particle determines the length of the next grating period. A numerical simulation of the electric fields results in the spatial harmonics. With this, the energy gain at synchronous phase and the particle velocity after passing the grating period can be determined. Afterwards the loop starts over again. A grating that is not correctly designed leads to dephasing, which implies that the synchronous phase changes continuously along the structure and synchronous acceleration of a particle bunch is prevented.

Under certain assumptions the energy spectrum after passing a (chirped) DLA grating can be calculated analytically [41]. These assumptions are to neglect the transverse dependence of the accelerating gradient and a change in peak gradient and phase within the interaction. Thus, the energy gain (Eq. 2.15) is simplified and the energy after an interaction length l is

$$E_{\mathrm{p}}\left(\varphi, E_{\mathrm{p,inj}}\right) = ql\left|\underline{e}_m^0\right|\cos\varphi + E_{\mathrm{p,inj}}, \tag{2.24}$$

where φ describes the injection phase and $E_{\mathrm{p,inj}}$ the injection energy of each particle. We can now use a random variable transformation from probability theory. We transform the two random variables φ and $E_{\mathrm{p,inj}}$ to E_{p} by Eq. 2.24. Thus, the initial bunch distribution as probability density function $\lambda_{\mathrm{inj}}\left(\varphi, E_{\mathrm{p,inj}}\right)$ is mapped to the energy spectrum after the interaction length as probability density function $\lambda_l\left(E_{\mathrm{p}}\right)$ by the integral

$$\lambda_l\left(E_{\mathrm{p}}\right) = \int_{-\infty}^{\infty} \frac{\lambda_{\mathrm{inj}}\left(\varphi\left(E_{\mathrm{p}}, E_{\mathrm{p,inj}}\right), E_{\mathrm{p,inj}}\right)}{\left|\frac{\partial E_{\mathrm{p}}\left(\varphi, E_{\mathrm{p,inj}}\right)}{\partial\varphi}\right|} \mathrm{d}E_{\mathrm{p,inj}}. \tag{2.25}$$

In order to solve Eq. 2.25, the inverse function $\varphi = \arccos\left(\left(E_{\mathrm{p}} - E_{\mathrm{p,inj}}\right)/\left(ql\left|\underline{e}_m^0\right|\right)\right)$ and the derivative $\partial E_{\mathrm{p}}\left(\varphi, E_{\mathrm{p,inj}}\right)/\partial\varphi = -ql\left|\underline{e}_m^0\right|\sin(\varphi)$ of Eq. 2.24 are required. For an initially Gaussian shaped bunch distribution,

$$\lambda_{\mathrm{inj}}\left(\varphi, E_{\mathrm{p,inj}}\right) = \frac{1}{2\pi\sigma_\varphi\sigma_E}\exp\left(-\frac{(\varphi-\varphi_0)^2}{2\sigma_\varphi^2}\right)\exp\left(-\frac{\left(E_{\mathrm{p,inj}} - E_{0,\mathrm{inj}}\right)^2}{2\sigma_E^2}\right), \tag{2.26}$$

with standard deviations σ_φ and σ_E and means φ_0 and $E_{0,\mathrm{inj}}$, the integral Eq. 2.25 can be written as a convolution

$$\lambda_l\left(E_{\mathrm{p}}\right) = \frac{1}{\sqrt{2\pi}\sigma_E}\int_{-\infty}^{\infty} \Lambda\left(E_{\mathrm{p}}\right)\exp\left(-\frac{\left(E_{\mathrm{p,inj}} - E_{0,\mathrm{inj}}\right)^2}{2\sigma_E^2}\right)\mathrm{d}E_{\mathrm{p,inj}} \tag{2.27}$$

with

$$\Lambda\left(E_{\mathrm{p}}\right) = \frac{1}{\sqrt{2\pi}\sigma_\varphi}\frac{1}{\sqrt{\left(ql\left|\underline{e}_m^0\right|\right)^2 - E_{\mathrm{p}}^2}}\exp\left(-\frac{\left(\arccos\left(\frac{E_{\mathrm{p}}}{ql\left|\underline{e}_m^0\right|}\right) - \varphi_0\right)^2}{2\sigma_\varphi^2}\right). \tag{2.28}$$

$\Lambda\left(E_{\mathrm{p}}\right)$ in Eq. 2.28 does not depend on the initial energy spectrum. Instead, it can be understood as the mapped probability function of a bunch, which initial energy distribution is a Dirac delta function, $\Lambda\left(E_{\mathrm{p}}\right) = \lambda_l\left(E_{\mathrm{p}}\right)\big|_{\sigma_E\to 0}$. Therefore, the energy distribution after interaction for an arbitrary initial energy distribution is also given by the convolution of $\Lambda\left(E_{\mathrm{p}}\right)$ with the initial energy distribution.

Figure 2.1 shows energy spectra of bunches with different width injected at the same phase. By increasing the bunch width the Gaussian shaped energy spectrum for coherent acceleration of the shortest bunch changes to the characteristic double horn structure for a bunch much longer than the grating period. Such double horn spectra have already been measured experimentally [10, 16].

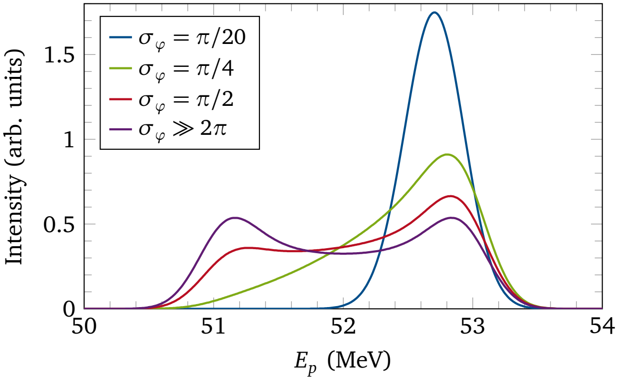

Figure 2.1: Analytically calculated energy spectra after DLA interaction for bunches with different σ_φ and $\sigma_E = 200\,\mathrm{keV}$ injected at a synchronous phase 45° off-crest. The energy gain of the reference particle is 707 keV (adapted from [41, Figs. 3 & 4]).

2.2 Alternating Phase Focusing

As shown in Eq. 2.20, the linearized and decoupled longitudinal and transverse motions are shifted by 90 degrees. This means a longitudinally focused bunch is defocused in the transverse direction and vice versa (see Fig. 2.2). During longitudinally stable acceleration, there are transverse defocusing forces in the $\mathrm{MT\,m^{-1}}$ range [32], which cannot be overcome by a conventional magnetic focusing lattice. However, if the synchronous phase changes along the DLA grating, this can be interpreted as a time dependent focusing potential providing beam confinement in both the longitudinal and one transverse plane. A first focusing concept was presented by Naranjo et al. [63]. They used the ponderomotive forces from the non-synchronous spatial harmonics for focusing and the synchronous ones for acceleration. Differing from this, we have proposed to use the synchronous spatial harmonics only simultaneously for focusing and acceleration by alternating the synchronous phase and thus the focusing direction [32].

In contrast to conventional accelerators, which use alternating quadrupole lattices for transverse beam confinement, in our scheme the phase alternates between the phase

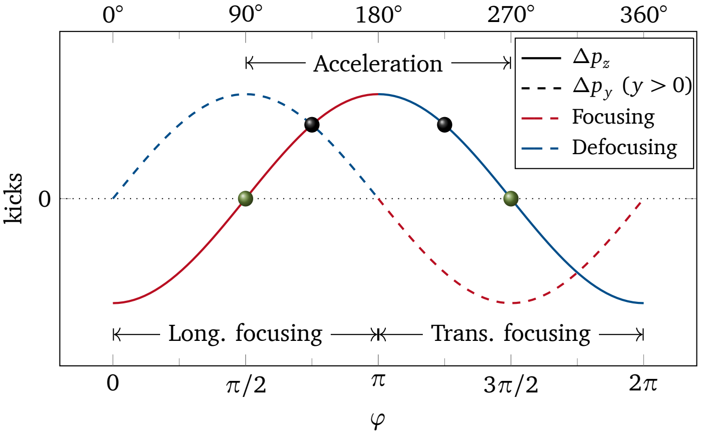

Figure 2.2: Electron acceleration and focusing properties as a function of phase. The green dots denote fixed points for beam transport, i.e., no acceleration, but longitudinal or transverse focusing, respectively. The black dots denote fixed points for transversely stable acceleration (adapted from [32, Fig. 2]).

range of longitudinal focusing and transverse focusing in the non-invariant plane of the grating. The phase ranges defined by the accelerating potential are shown in Fig. 2.2. Furthermore, two exemplary couples of fixed points are depicted. Shifting the phase by 180° between the green points provides stable beam transport, i.e, transverse confinement without acceleration. Shifting the phase between the black dots enables beam confinement and acceleration simultaneously. The phase shifts are realized by a fractional cell drift between two segments with constant synchronous phase. According to Eqs. 2.15 and 2.16, stable beam transport and acceleration are given for synchronous phases $\varphi_0 = 90° + n \cdot 180°$ and $\varphi_0 \in (90°, 270°) + n \cdot 180°$ with $n \in \mathbb{Z}$, respectively. Equation 2.21 shows, that a phase shift by $\Delta\varphi_0 = 360° - 2\varphi_0 + n \cdot 360°$ changes only the sign of the focusing strength, while the accelerating gradient stays constant.

Each lattice cell in the alternating phase focusing scheme consists of a transversely focusing segment with length L_f and p DLA cells followed by a drift of length $l_{\mathrm{f}\to\mathrm{d}}$ and a transversely defocusing segment with length L_d and $\tilde{p}$ DLA cells followed by a drift of length $l_{\mathrm{d}\to\mathrm{f}}$, where the drift lengths are defined by

$$l_{\mathrm{f}\to\mathrm{d}} = \frac{2\pi - \varphi_{0,\mathrm{f}}}{\pi} \beta^{(p)} \lambda_0, \tag{2.29a}$$

$$l_{\mathrm{d}\to\mathrm{f}} = \frac{\pi - \varphi_{0,\mathrm{d}}}{\pi} \beta^{(p+\tilde{p})} \lambda_0 \tag{2.29b}$$

with $\varphi_{0,\mathrm{f}} = 2\pi - \varphi_{0,\mathrm{d}}$. Due to this structure, a lattice cell is often called FODO cell. Both segments can be modeled as thick lenses with the transfer matrices

$$M_\mathrm{f}(z) = \begin{pmatrix} \cos\left(\sqrt{K}z\right) & \frac{1}{\sqrt{K}}\sin\left(\sqrt{K}z\right) \\ -\sqrt{K}\sin\left(\sqrt{K}z\right) & \cos\left(\sqrt{K}z\right) \end{pmatrix}, \tag{2.30a}$$

$$M_\mathrm{d}(z) = \begin{pmatrix} \cosh\left(\sqrt{K}z\right) & \frac{1}{\sqrt{K}}\sinh\left(\sqrt{K}z\right) \\ \sqrt{K}\sinh\left(\sqrt{K}z\right) & \cosh\left(\sqrt{K}z\right) \end{pmatrix}. \tag{2.30b}$$

For long segments ($p, \tilde{p} \gg 1$), the drifts can be neglected and the lattice cell can be represented by the transfer matrix $M_\mathrm{fd}(L_\mathrm{f} + l_{\mathrm{f}\to\mathrm{d}} + L_\mathrm{d} + l_{\mathrm{d}\to\mathrm{f}}) = M_\mathrm{d}(L_\mathrm{d} + l_{\mathrm{d}\to\mathrm{f}}) M_\mathrm{f}(L_\mathrm{f} + l_{\mathrm{f}\to\mathrm{d}})$. In a strictly periodic beam transport lattice with length $L = (2p+1)\beta\lambda_0$, the matched Twiss parameters can be calculated by solving the eigenvalue problem in Eq. 1.16. The maximum of the resulting Twiss beta function, which occurs in half of the focusing segment, gives a limit on the emittance, that fits the aperture. Furthermore, the phase advance per lattice cell μ is given by

$$\cos(\mu) = \cos\left(\frac{1}{2}\sqrt{K}L\right)\cosh\left(\frac{1}{2}\sqrt{K}L\right) < 1, \tag{2.31}$$

where the inequality relation resembles the stability criterion of Eq. 1.10 for stable beam confinement. As for the transverse plane, it is also feasible to define Twiss parameters for the longitudinal phase space, where the longitudinal envelope is a measure of the bunch length. According to the shift in the focusing properties, the longitudinal Twiss parameters are shifted by half a lattice cell to the transverse ones.

In an accelerating lattice, the transfer matrices of the segments can also be used to map the initial Twiss parameters through the lattice. Since the lattice is no longer periodic, the Twiss parameters can only be approximated by the periodic eigenvalue solution of each lattice cell. This approximation is sufficiently fulfilled if the change in segment and period length is small. If this is true, it can be used in the lattice design process to determine the segment lengths where the maximum of the Twiss beta function is minimal for given particle velocity, peak gradient, and synchronous phase (see Fig. 2.3).

2.3 Structure Design and Optimization

For the design and optimization of a DLA grating structure, we can distinguish two different tasks: single cell optimization and lattice design. The first one is a classical numerical optimization task defining various quantities of interest as, for example, highest gradient in the center of the channel or lowest field in the material for a given laser field strength or highest bandwidth. Using periodic boundary conditions in the direction of the electron beam propagation, the fields in a single DLA cell can be simulated by sev-

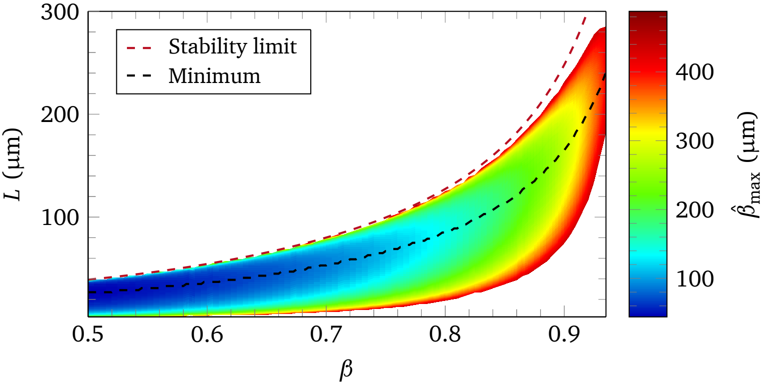

Figure 2.3: Maximal Twiss beta function $\hat{\beta}_{\mathrm{max}}$ in the (β, L) plane for acceleration from 83 keV to 1 MeV at a synchronous phase 60° off-crest with an average gradient of $187\,\mathrm{MV\,m^{-1}}$ (adapted from [32, Fig. 4]).

eral methods such as Finite Difference/Integration Time Domain [30], Finite Difference Frequency Domain [64], or Finite Element Frequency Domain [29]. The geometrical degrees of freedom for the optimization can be determined from a physical point of view or based on structures, that are known to be fabricable. A more rigorous mathematical approach uses adjoint methods in order to optimize a structure geometry with a continuous permittivity distribution [28]. However, the continuous permittivity must be converted into a manufacturable discrete distribution. As an example, Fig. 2.4 shows a dual pillar structure to be optimized for highest gradient and the corresponding density plot of the absolute value of the first harmonic as function of the geometrical degrees of freedom, which is the pillar radii. In this example, the simulations of a periodic single cell are made with CST Microwave Studio [65].

The second task is a full lattice design taking beam dynamics into consideration. Starting point of the design is the optimized single cell. The design process then follows the workflow shown in Fig. 2.5, which is explained in more detail below. Initial parameters of the design are on the one hand laser parameters like wavelength and peak field strength and on the other hand the initial particle beam energy and the chosen synchronous phase. In all steps except the full 3D field simulation, the laser field is assumed to be a plane wave, which is justified if the laser pulse length is significantly longer than the bunch length and the pulse front is tilted such that the reference particle stays in the center of the pulse while it passes through the lattice [67, 68]. The aim of the lattice design is the highest possible throughput of particles through the whole lattice. For a pure transport structure, the lattice is strictly periodic and we can calculate the matched Twiss parameters as a function of the segment length and select the

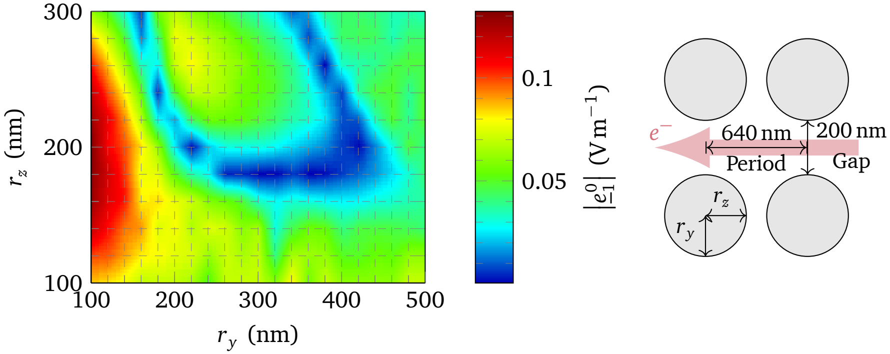

Figure 2.4: Parameter plot of the first spatial harmonic (left) of a silicon dual pillar structure (right) and an incident laser field with 2 µm wavelength and $1\,\mathrm{V\,m^{-1}}$ normalized peak field. The structure period length is synchronized to particles with $\beta = 0.32$.

length with the smallest envelope. For an accelerating lattice, a first guess is done the same way, i.e., the matched Twiss beta function is calculated as a function of the segment length and additionally the velocity of the reference particle. The segment length is then selected so that it follows the minimal envelope as a function of the velocity of the reference particle (cf. Fig. 2.3). However, since the energy of the particles increases within the lattice, the period length of a single DLA cell and also the focusing strength (Eq. 2.21) changes, which breaks the periodicity of the lattice. Thus, the calculated Twiss parameters are no longer matched to the lattice and the beam envelope increases. Figure 2.6 shows such an increase in the longitudinal Twiss beta function. Furthermore, it shows that a few manual corrections of the segment lengths can reduce the increase significantly. In this example, the maximum of the transverse Twiss beta function is almost the same in the corrected and uncorrected lattice. This is, however, not generally true. The remaining increase in the Twiss beta function is counteracted by adiabatic damping of the emittance due to momentum increase (cf. Eq. 1.20), so that the local maxima of the beam envelope are almost constant.

So far, only linearized dynamics are considered. Therefore, the next work steps after exporting the lattice geometry and the initial Twiss parameters is a multi-tool validation approach: we can use a simplified tracking simulation which takes a couple of minutes for an usual lattice design of a few thousand periods. Using this fast simulation tool, we can verify that non-linearities have no undue influence on the Twiss beta functions and we can estimate the maximum possible emittance for a desired particle throughput. Due to the assumption that a segment contains only quasi-periodic single cells, edge field effects at the end of a segment, fields in the drift sections, and coupling between

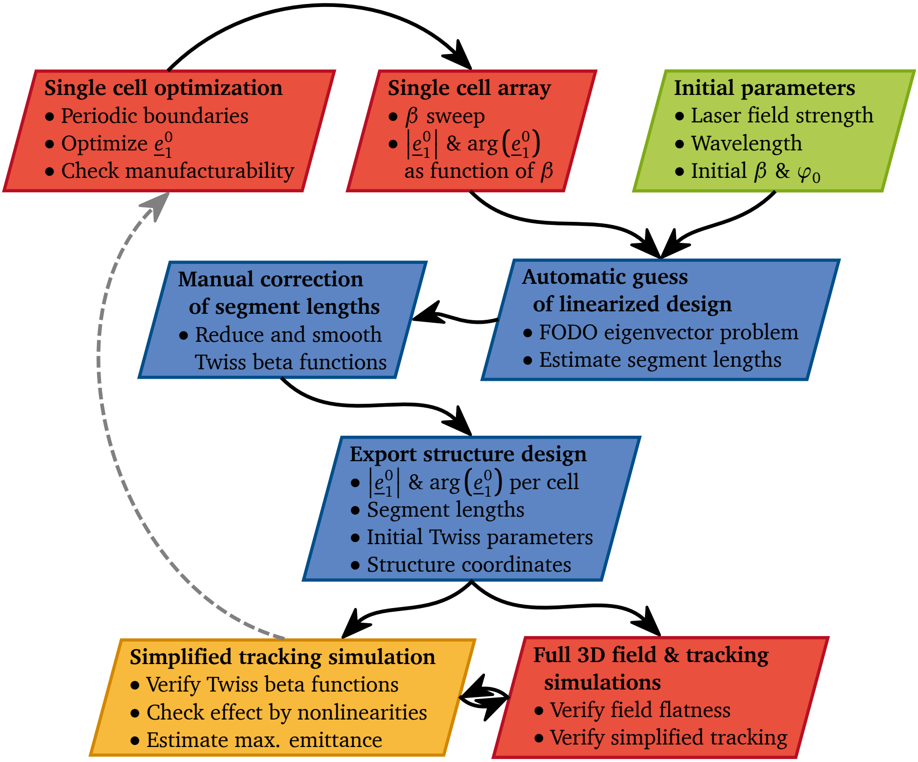

Figure 2.5: Workflow for linearized structure design. The color of the boxes specifies the used program: Red - CST Studio Suite [65], blue - Mathematica [66], yellow - DLAtrack6D (Matlab/Python) [31]

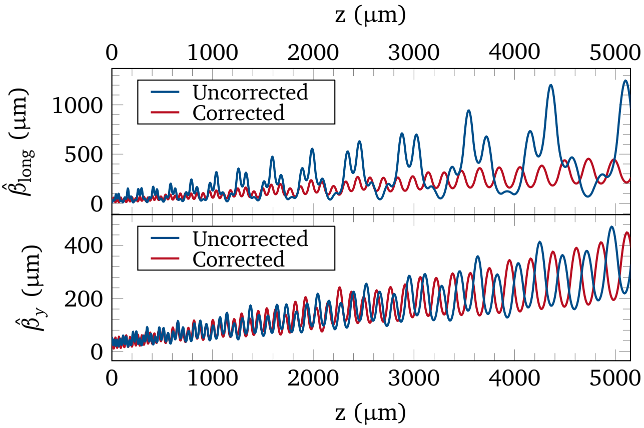

Figure 2.6: Twiss beta functions of an accelerating lattice from 83 keV to 1 MeV with an average gradient of 187 MV m^{-1} at a synchronous phase ± 60° off-crest. In the longitudinal plane, the manual corrections reduce the beta function significantly (top), whereas the maximum of the transverse one remains almost unchanged (bottom).

the segments are neglected in these simplified simulations. Therefore, CST Studio Suite is additionally used to simulate the full three-dimensional electromagnetic fields in the structure and track the particles through these fields. Such simulations take hours up to days, but they provide the opportunity to check the results of the simplified tracking and analyze the effects of edge fields and coupling. If the simulation results of both tools match and fulfill the required specifications, the CAD model included in the CST simulation can directly be transferred to the nanofabrication.

3 Wake Fields in Dielectric Laser Accelerator Structures

Wake fields in DLA structures are generated by the Smith-Purcell effect and the Cherenkov effect simultaneously. The grating apertures are almost completely filled by particles. Therefore, an analytical calculation of the wake fields is not possible and numerical simulations are required. Section 3.1 presents the simulation model applied to calculate the wake field of an arbitrarily shaped bunch. Section 3.2 summarizes longitudinal wake field results including simulation to validate the used models and Sec. 3.3 concludes the chapter by showing the results of transverse wake field simulations.

3.1 Wake Field Simulation Model and Convolution

In order to calculate the wake field of DLA structures, we use the time-domain wake field solver in CST Studio Suite [65]. The wake field solver in CST Studio Suite applies a transient solver based on the Finite Integration Technique [69] to calculate the electromagnetic fields (see Fig. 3.1) step by step through time by the Leap-Frog updating scheme. The wake potential is then determined by evaluating Eq. 1.25. A longitudinally

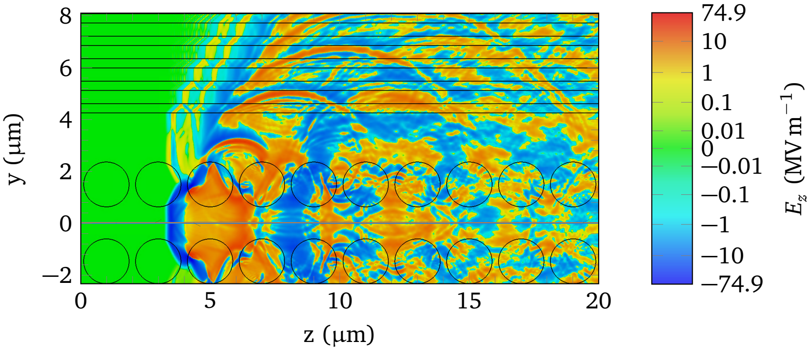

Figure 3.1: Snapshot of the longitudinal electric field generated by a 50 nm bunch with a charge of 1 fC at $z = 3.435$ µm in a dual pillar structure (adapted from [43, Fig. 1]).

Gaussian shaped moving line charge (like a pencil beam) parallel to the z-axis is used as source bunch. Open boundary conditions are applied in y- and z-direction and electric boundary conditions in x-direction to limit the simulation range (cf. Fig. I.2 for a clarification of the coordinate axes). The required length of the simulation model, which corresponds to the number of DLA periods, is given by the catch-up distance. This is the position z_c reached by a test particle traveling a distance s behind the source particle, when the test particle will experience the wake fields scattered at a distance b from the particle trajectory [70],

$$z_c \approx \frac{b^2 - s^2}{2s}. \tag{3.1}$$

Therefore, the number of DLA periods and the spacing to the boundaries is chosen such that the short-range wake field per DLA period converges without being influenced by the boundary conditions. This implies that the long-range wake, for which the catch-up distance is shorter, is possibly influenced by the boundary conditions and the trustworthy range has to be checked in each simulation. Our simulation models are validated against to other codes and analytical models in Sec. 3.2.1.

For the computation of the wake field induced by an arbitrary shaped bunch, we start from a periodic grating structure, which is translation invariant in x-direction, and simulate the wake potential of a longitudinally Gaussian shaped bunch distribution with a short bunch length as described above. The integration paths, on which the wake field is calculated, are arranged on a rectangular grid in the gap region and the excitation beam path is varied along the locations of the integration path in y-direction (see Fig. 3.2). The simulation is performed for each position of the source beam. Due to the translation symmetry of the structure in x-direction, it is sufficient to have all beam paths at the same x-position. If the length of the Gaussian excitation signal is much shorter than the real bunch length, the simulation wake result is a good approximation of Green's function $\vec{w}(x-\tilde{x}, y, \tilde{y}, \tilde{s})$, where $\tilde{x}$ and $\tilde{y}$ are the coordinates of the beam path, x and y are the coordinates of the integral path, and $\tilde{s}$ is the longitudinal coordinate with $\tilde{s}=0$ at

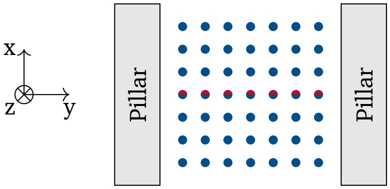

Figure 3.2: Integration paths (blue) and beam paths (red) in the CST wake field simulation model. For each beam path one simulation is performed and wake fields are calculated on each integration path (adapted from [43, Fig. 2]).

the position of the charge. The error of this approximation can be estimated by considering two Gaussian bunch distributions with bunch lengths $\sigma_{z,1}$ and $\sigma_{z,2}$, respectively, and $\sigma_{z,1} < \sigma_{z,2}$. The exact longitudinal wake potential of the second bunch is then given by [71]

$$W_{z,2}(s) = \frac{1}{\sqrt{2\pi}\sigma_{z,12}} \int_{-\infty}^{\infty} W_{z,1}(s') \exp\left(-\frac{(s-s')^2}{2\sigma_{z,12}^2}\right) \mathrm{d}s' \tag{3.2}$$

with $\sigma_{z,12}^2 = \sigma_{z,2}^2 - \sigma_{z,1}^2$. Equation 3.2 can be proven by substituting $W_{z,1}(s')$ with the convolution of the wake function and the Gaussian distribution with standard deviation $\sigma_{z,1}$. After a few mathematical operations the convolution of the wake function and the Gaussian distribution with standard deviation $\sigma_{z,2}$ is obtained. The approximation with the wake potential $W_{z,1}$ of the first bunch as Green's function is, however,

$$W_{z,2}^{\mathrm{approx}}(s) = \frac{1}{\sqrt{2\pi}\sigma_{z,2}} \int_{-\infty}^{\infty} W_{z,1}(s') \exp\left(-\frac{(s-s')^2}{2\sigma_{z,2}^2}\right) \mathrm{d}s'. \tag{3.3}$$

The convolution with an arbitrary bunch distribution on an arbitrary transverse position in the gap results in the wake potential

$$\vec{W}(x,y,s) = \int_{-\infty}^{\infty}\int_{-\infty}^{\infty}\int_{-\infty}^{\infty} \vec{w}(x-\tilde{x},y,\tilde{y},\tilde{s})\,\lambda(\tilde{x},\tilde{y},s-\tilde{s})\,\mathrm{d}\tilde{x}\,\mathrm{d}\tilde{y}\,\mathrm{d}\tilde{s}, \tag{3.4}$$

where the bunch distribution is normalized as $\int_V \lambda(x,y,s)\,\mathrm{d}V = 1$. For simplicity, we assume an uncorrelated distribution $\lambda(\tilde{x},\tilde{y},s-\tilde{s}) = \lambda_x(\tilde{x})\,\lambda_y(\tilde{y})\,\lambda_s(s-\tilde{s})$. This splits the three-dimensional integral in Eq. 3.4 in three independent one-dimensional integrals. First we execute the integral over the transverse coordinate y,

$$\vec{W}^{\lambda_y}(x-\tilde{x},y,\tilde{s}) = \int_{-\infty}^{\infty} \vec{w}(x-\tilde{x},y,\tilde{y},\tilde{s})\,\lambda_y(\tilde{y})\,\mathrm{d}\tilde{y}. \tag{3.5}$$

Then the second transverse integral follows as a convolution of the first result,

$$\vec{W}^{\lambda_x\lambda_y}(x,y,\tilde{s}) = \int_{-\infty}^{\infty} \vec{W}^{\lambda_y}(x-\tilde{x},y,\tilde{s})\,\lambda_x(\tilde{x})\,\mathrm{d}\tilde{x}, \tag{3.6}$$

and finally the longitudinal convolution results in the wake potential

$$\vec{W}(x,y,s) = \int_{-\infty}^{\infty} \vec{W}^{\lambda_x\lambda_y}(x,y,\tilde{s})\,\lambda_s(s-\tilde{s})\,\mathrm{d}\tilde{s}. \tag{3.7}$$

We will now discretize the above integrals, i.e., approximate them as sums. The integral over the transverse coordinate $\tilde{y}$ is, for example, approximated as

$$\vec{W}^{\lambda_y}\left(x-\tilde{x},y,\tilde{s}\right)\approx\Delta\tilde{y}\sum_{n_{\tilde{y}}}\left[\vec{w}\left(x-\tilde{x},y,n_{\tilde{y}}\Delta\tilde{y},\tilde{s}\right)\lambda_y\left(n_{\tilde{y}}\Delta\tilde{y}\right)\right], \tag{3.8}$$

where the wake function and the bunch distribution are evaluated at $n_{\tilde{y}}$ points with distance $\Delta\tilde{y}$ in y-direction. The sum can be interpreted as a tensor product with all coordinates replaced by representative indices

$$\begin{aligned}\vec{W}^{\lambda_y}\left(x-\tilde{x},y,\tilde{s}\right)&\approx\vec{W}^{\lambda_y}_{n_x,n_{\tilde{x}},n_y,n_{\tilde{s}}} &\text{(3.9a)}\\ &=\Delta\tilde{y}\sum_{n_{\tilde{y}}}\vec{w}_{n_x,n_{\tilde{x}},n_y,n_{\tilde{y}},n_{\tilde{s}}}\lambda^y_{n_{\tilde{y}}}. &\text{(3.9b)}\end{aligned}$$

The discrete representation of Eq. 3.4 follows as

$$\vec{W}\left(n_x,n_y,n_s\right)=\Delta\tilde{s}\Delta\tilde{x}\Delta\tilde{y}\sum_{n_{\tilde{s}}}\sum_{n_{\tilde{x}}}\sum_{n_{\tilde{y}}}\vec{w}_{n_x,n_{\tilde{x}},n_y,n_{\tilde{y}},n_{\tilde{s}}}\lambda^y_{n_{\tilde{y}}}\lambda^x_{n_{\tilde{x}}}\lambda^s_{n_{\tilde{s}},n_s}, \tag{3.10}$$

which can be implemented in a very efficient manner. As an example Fig. 3.3 shows the wake potential of a Gaussian shaped bunch distribution passing through a rectangular grating with an aperture of 1.2 µm. In contrast to conventional accelerator beam pipes, whose aperture is much larger than the bunch width and whose wake potential can thus be assumed to be independent of the transverse position within the bunch, the apertures of a DLA grating are almost completely filled by particles and the wake potential depends highly on the transverse position.

Longitudinal and transverse wake fields are coupled by the Panofsky-Wenzel theorem (cf. Eq. 1.30). We can use this relation as validation of the wake potentials numerically calculated by Eq. 3.10. The relative error in fulfilling the y-component of Eq. 1.30 is written as

$$f_{\mathrm{PW}}\left(x,y,s\right)=\frac{\left|\frac{\partial}{\partial y}W_s\left(x,y,s\right)+\frac{\partial}{\partial s}W_y\left(x,y,s\right)\right|}{\left|\frac{\partial}{\partial s}W_y\left(x,y,s\right)\right|+\left|\frac{\partial}{\partial y}W_s\left(x,y,s\right)\right|} \tag{3.11}$$

with $f_{\mathrm{PW}}\left(x,y,s\right)\ll 1$, which is plotted in Fig. 3.4. The plot shows that the numerical difference in the Panofsky-Wenzel theorem applied to the wake fields plotted in Fig. 3.3 is well below 1% except for one spot where both derivatives of the wake are zero and thus artifacts of the finite differences blow up the relative error.

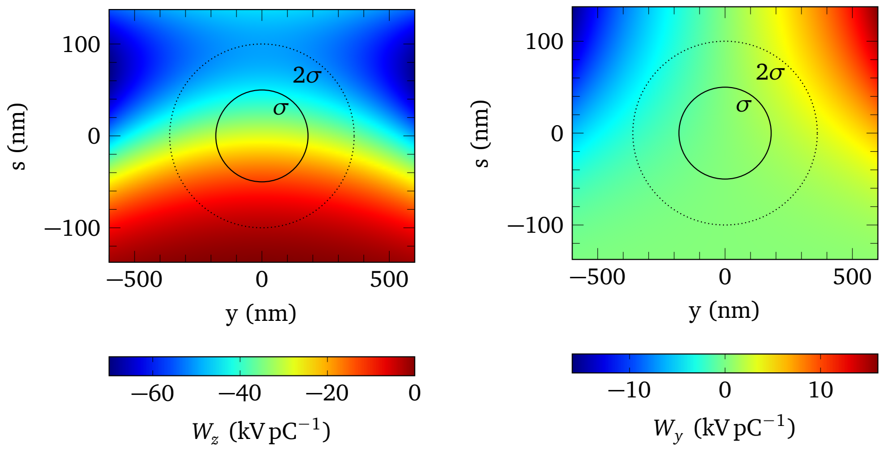

(a) Longitudinal wake **(b)** Transverse wake

Figure 3.3: Two-dimensional wake potential per DLA grating period generated by a bunch with 50 nm longitudinal and 181 nm transverse size. The standard deviation is indicated by the black ellipses (adapted from [43, Fig. 3]).

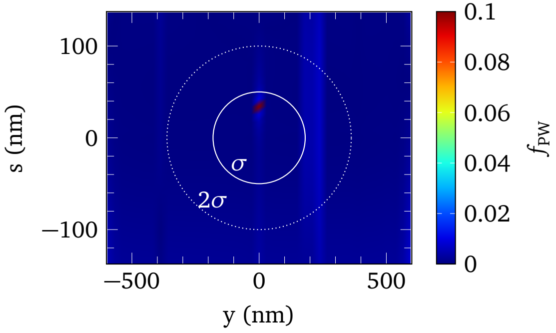

Figure 3.4: Normalized difference between the left end the right hand side of the Panofsky-Wenzel theorem (Eq. 3.11) calculated for the simulated wake field data of a Gaussian bunch distribution with standard deviation given by the white ellipse. The wake fields are shown in Fig. 3.3 (adapted from [43, Fig. 3]).

3.2 Longitudinal Wake Field

Longitudinal wake fields lead to a position dependent energy modulation. This result in a change of the energy spread and also in a modulation of the mean energy of the whole bunch. The longitudinal wake fields of different structure geometries are presented in the following. Section 3.2.1 shows the validation of the wake field simulation model in CST Studio Suite against wake field results of other simulation tools and a comparison with analytical solutions of similar structures. In Sec. 3.2.2, scaling laws are described, which are useful if the numerical wake field simulations are computationally expensive. The findings can also be applied to the transverse wake fields by the Panofsky-Wenzel theorem (Eq. 3.11). Furthermore, Section 3.2.3 proposes structures with tunable wake fields depending on the transverse position of the beam within the structure.

3.2.1 Validation of Simulation Model

In order to validate the simulation model used in CST Studio Suite, we compare the CST longitudinal wake field results of a longitudinally Gaussian shaped pencil beam with results calculated by two other simulation codes. In Fig 3.5a the three-dimensional CST results of a rectangular grating are compared to two- and three-dimensional simulation results of VSim [72] based on the Finite Difference Time Domain method. The wake field calculation is done by manually integrating the electromagnetic fields exported from the time domain simulations. As expected, the three-dimensional results agree very well. However, the two-dimensional simulation shows large differences, especially in the long-range wake. This is accounted to effects in the dielectric material that are not captured in the two-dimensional model. A two-dimensional wake field simulation is therefore physically not sufficient. Furthermore, the longitudinal wake of a cavity structure proposed in [30] is calculated by CST and the parallelized PBCI code, which uses a moving window approach [73]. The simulation with PBCI was done by Erion Gjonaj. The short-range wake results shown in Fig. 3.5b agree also very well.

For a metallic corrugated plate with a similar geometry as the dielectric rectangular structure, there is an analytical model for the short range wake by Bane et al [74]. The longitudinal wake function for $s > 0$ is given by

$$w_z(s,y) = \frac{\pi^2}{g^2} \sec^2\left(\frac{\pi y}{g}\right) \exp\left(-\sqrt{\frac{s}{s_{0l}}}\right) \tag{3.12}$$

with

$$s_{0l} = \frac{g^2 t}{2\pi \left[\alpha(t/\lambda_z)\right]^2 \lambda_z^2} \left[1 + \frac{1}{3}\cos^2\left(\frac{\pi y}{g}\right) + \left(\frac{\pi y}{g}\right)\tan\left(\frac{\pi y}{g}\right)\right]^{-2}, \tag{3.13}$$

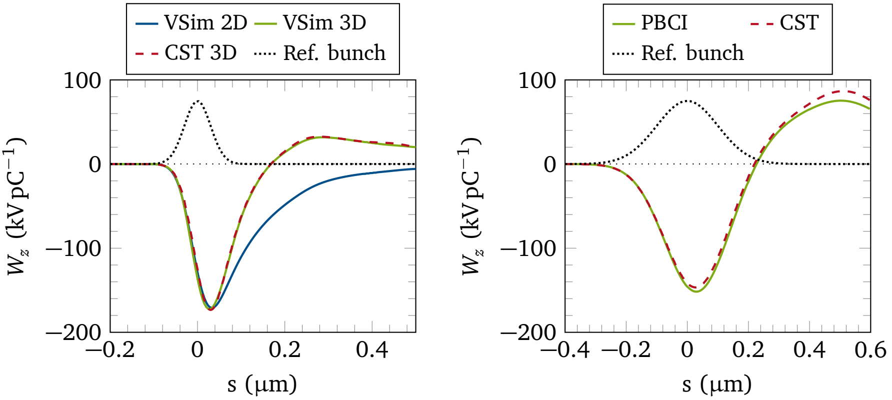

(a) Comparison between CST and VSim. **(b)** Comparison between CST and PBCI.

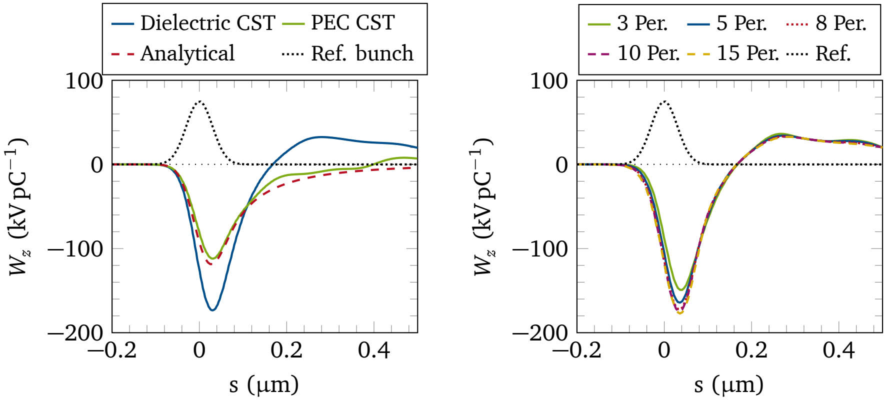

(c) Comparison between analytical model of metallic corrugated plates, a CST model with dielectric material and a CST model with PEC material.

(d) Study of longitudinal wake per period for different number of periods simulated.

Figure 3.5: Validation of CST wake field model by comparison of the longitudinal wake field per DLA grating period with other codes and an analytical model and by studying the convergence of the longitudinal wake field per DLA grating period. The simulated structure in Figs. (a), (c), and (d) is a rectangular grating with 800 nm period length, $\varepsilon_\mathrm{r} = 2.4$, 400 nm aperture, 400 nm tooth width, 576 nm tooth height, and 30 nm bunch length. For Fig. (b), a cavity structure with 920 nm period length $\varepsilon_\mathrm{r} = 11.63$, 200 nm aperture, 100 nm tooth width, 306 nm tooth height, and 100 nm bunch length is used.

where g represents the gap, λ_z the period length, t the longitudinal gap between the corrugations, h the depth of the corrugations, and $\alpha(x) \approx 1 - 0.465\sqrt{x} - 0.07x$. Due to causality the wake function vanishes for $s < 0$. Figure 3.5c shows the wake potential calculated by a convolution of the wake function in Eq. 3.12 compared with the CST results of the corresponding dielectric rectangular grating and a grating where perfect electric conducting material is used instead of dielectric. The analytical solution is a fairly good approximation for the PEC grating, but the results differ greatly from the wake field of the dielectric grating. Since in the wake field of the dielectric grating the Smith-Purcell effect and the Cherenkov effect are present, the analytical solution represents only the Smith-Purcell wake and the difference to the result of the dielectric grating is affected by the Cherenkov wake in the material.

Since the available number of mesh cells in the simulation is limited, we have to find a trade-off between accuracy and mesh size. Both are increasing with increasing number of periods (cf. catch-up distance, Eq. 3.1, for accuracy). Figure 3.5d shows the longitudinal wake field per grating period for rectangular gratings with various numbers of DLA periods. As expected, the simulations converge with increasing number of periods. Simulations with 10 periods do not deviate much from those with 15 periods. Thus, all analyzed models contain at least 10 to 15 DLA periods.

The Smith-Purcell wake is already estimated by the analytical wake function of a metallic corrugated plate (see Eq. 3.12). The additional effects in the dielectric material creating the Cherenkov wake are intensively studied within the context of driving wake fields in dielectric wake field accelerators (DWAs) [75, 76, 77]. In DWAs, wake fields created by an electron beam passing a slab-symmetric or cylindrical-symmetric, dielectric loaded structure are used to accelerate a second electron beam following the first one through the structure. The rectangular DLA grating can be converted to a slab-symmetric grating by filling the space between the teeth or by cutting off the teeth, which increases the vacuum gap. The longitudinal wake of booth variants is plotted in Fig. 3.6a. Filling the spaces leads to a larger Cherenkov wake and thus also to a stronger longitudinal wake per grating period than the rectangular DLA grating. On the other hand, an increase of the gap by cutting off the teeth results in a significantly smaller wake, whose peak is additionally shifted to larger s. These simulations and the comparison to the analytical solution of a metallic corrugated plate show that distinguishing between Smith-Purcell and Cherenkov wake is not trivial and a good analytical approximation of the wake field created by a DLA grating is therefore almost impossible.

The discussion of DWA structures has also shown that the distance of the beam center to the first vacuum dielectric interface is crucial for the strength of the wake field. However, what about reflections on the opposite side of the grating? Is the wake of a single-sided grating half the wake of a dual-sided grating? This question is answered in Fig. 3.6b. If we compare the longitudinal wake per grating period of a dual-sided rectangular grating with the doubled longitudinal wake of a single-sided rectangular grating with the same geometric parameters at the distance of the half gap of the former grating, the short-range wakes are almost identical. Due to reflections, only the

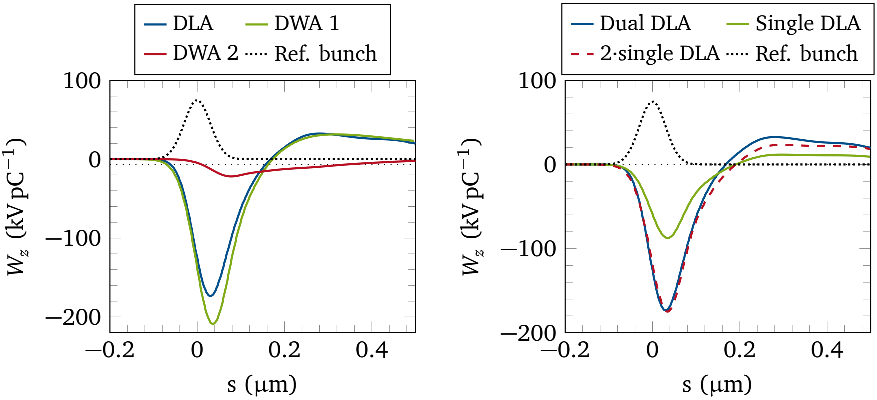

(a) Comparison between DLA and DWA structures. The analyzed structure is a rectangular grating with 800 nm period length as described in the caption of Fig. 3.5. For DWA 1, a planar structure is generated by filling in the space between the teeth. For DWA 2, the teeth are removed.

(b) Comparison between single and dual DLA structure. The analyzed structure is a rectangular grating with 800 nm period length as described in the caption of Fig. 3.5.

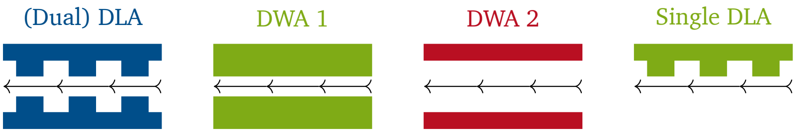

(c) DLA and DWA structures used in Figs. (a) and (b).

Figure 3.6: Longitudinal wake field per grating period of different DLA and DWA structures.

long-range wake differs slightly. This agrees with the findings of Schächter et al [37] indicating that reflections of the self-fields have no effect on the exciting point charge, if the propagation length of the self-field including reflections is large in comparison to the gap size.

3.2.2 Structure Scaling

During the design of an accelerating lattice based on DLA structures, the geometric parameters of the structures are often changed. For each parameter set, we have to repeat the simulations. This effort can be significantly reduced by using scaling laws. The easiest case is if all dimensions of the excitation and the grating structure are changed by the same factor at the same time. If they are modified by a scaling factor α, i.e., $\tilde{s} = \alpha s$, the Green's function wake per period scales as α^{-1} [71], i.e., $\tilde{w}(\tilde{s}) = \alpha^{-1} w(s)$. For a longitudinal bunch distribution, which is also scaled as $\tilde{\lambda}(\tilde{s}) = \alpha^{-1}\lambda(s)$, the wake potential scales the same as the Green's function wake. This follows from the convolution

$$\tilde{W}(\tilde{s}) = \int_{-\infty}^{\infty} \tilde{\lambda}\left(\tilde{s} - \hat{\tilde{s}}\right) \tilde{w}\left(\hat{\tilde{s}}\right) \mathrm{d}\hat{\tilde{s}} \tag{3.14a}$$

$$= \alpha^{-1} \int_{-\infty}^{\infty} \lambda(s - \hat{s})\, w(\hat{s})\, \mathrm{d}\hat{s} \tag{3.14b}$$

$$= \alpha^{-1} W(s)\,. \tag{3.14c}$$

Scaling the period length of a grating structure and the laser wavelength for $\beta \approx 1$ is equivalent to modifying all dimensions. The change in period length causes a change in acceptable bunch length for coherent acceleration and also a change in the decay length of the evanescent fields in the channel. Most DLA experiments are performed at a laser wavelength of $\lambda_0 = 2\,\mu\mathrm{m}$, but there are also experiments at $\lambda_0 = 800\,\mathrm{nm}$ at UCLA [18] or at $\lambda_0 = 50\,\mu\mathrm{m}$ at PSI (cf. Sec. 3.2.3). In order to scale these structures, Eq. 3.14c can be used with $\alpha = 2.5$ or $\alpha = 0.04$, respectively.

If only single geometric parameters are changed, the wake field can change qualitatively. The integrated effect of these changes is the energy change of the entire bunch distribution. This can be analyzed by the loss factor k_{loss} (cf. Eq. 1.28) and compared to the accelerating gradient expressed by the absolute value of the first Fourier coefficient in the center of the gap $\left|\underline{e}_1^0\right|$ (cf. Eq. 2.3). An increase of the gap width, for example, lowers the wake field and thus the loss factor significantly. However, the absolute value of the first Fourier coefficient also decreases with the gap width. Figure 3.7 shows the loss factor indicating the strength of the wake effects in comparison to $\left|\underline{e}_1^0\right|$ for the grating described previously as function of the gap width. The plateau in the first Fourier coefficient represents a robust optimum for the vacuum gap in the range of 1.2 µm. Values, that fulfill a Bragg condition within a DLA period are resonant, as e.g. at a gap of

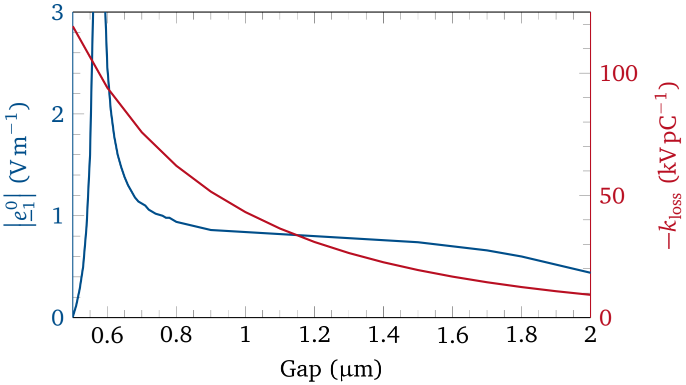

Figure 3.7: Loss factor indicating the strength of wake effects as function of the vacuum gap compared to the absolute value of the first Fourier coefficient indicating the accelerating gradient in the center of a fused silica dual pillar structure with 2 µm period length for a normalized laser peak field of 1 V m^{-1} (adapted from [43, Fig. 4]).

0.6 µm. Thus, they are sensitive to parameter changes and also impede the use of short laser pulses due to the limited bandwidth.

In contrast to geometrical changes, modifications in the relative permittivity only slightly affect the loss factor, since it constitutes an average over a large frequency band and is dominated by the geometry. However, the narrow-band external laser drive is very sensitive to material changes, which in turn requires structure optimization (cf. Sec. 2.3).

There are different geometries of dual-layer DLA structures in use in recent experiments, especially rectangular grating structures and dual pillar structures [62]. If we optimize a fused-silica dual-layer rectangular grating and a dual pillar structure, both with the same vacuum gap and the same period length, in terms of accelerating gradient, we reach for the rectangular grating a gradient 40 % lower than for the dual pillar structure. Another option is to replace one row of pillars with a Bragg mirror. The three structure shapes are given in Fig. 3.8a. Figure 3.8b compares the longitudinal wake per grating period of the structures for a Gaussian shaped line charge, where good agreement between the curve shapes is visible. However, in contrast to the accelerating gradient, the wake of the dual pillar structure is slightly weaker than of the other two geometries. The short-range wake of the single-sided pillar structure with Bragg mirror is almost equal to the rectangular grating but additional effects in the long-range wake occur. Breaking the symmetry by the Bragg mirror generates a non-vanishing transverse wake deflecting an on-axis bunch (see Fig. 3.8c). If the distance of the Bragg mirror is much larger than the vacuum gap, it does not significantly affect the short-range wake. If the Bragg mirror is located near to the vacuum gap or one pillar row is even replaced by the Bragg mirror, it affects also the short-range wake.

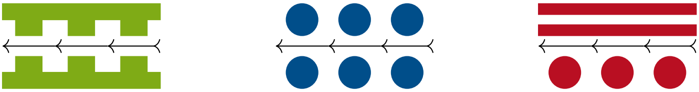

(a) DLA structures used for comparison: rectangular grating (left), dual pillar structure (center), and single-row pillar structure, where the second row is replaced by a Bragg mirror (right).

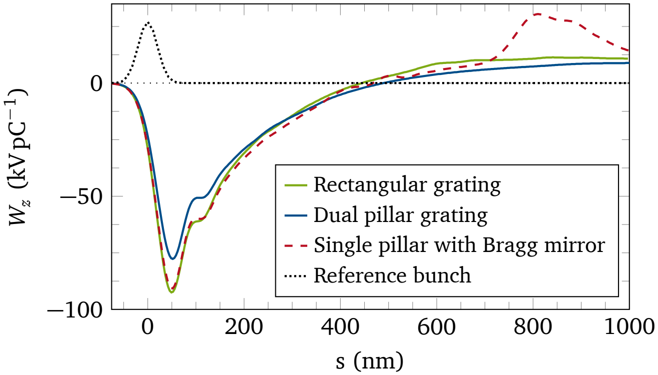

(b) Longitudinal wake field per grating period of the three DLA structures shown above (adapted from [43, Fig. 5]).

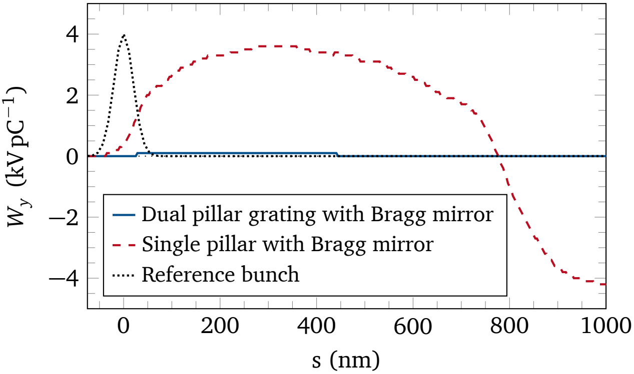

(c) Transverse on-axis wake field per grating period of a dual pillar structure (blue) with an additional Bragg mirror and a single-row pillar structure with a close Bragg mirror (adapted from [43, Fig. 6]).

Figure 3.8: Wake fields per grating period of a Gaussian bunch distribution passing on-axis through three different DLA structures. The reference bunch distribution is shown in dotted black.

3.2.3 Tunable DLA Grating

A possible application of DLA structures besides high energy gain is the phase space modulation or bunch shaping of electron beams from a conventional linear accelerator. This is possible in two ways: active modulation by an external laser field or passive modulation by self-fields of the electron beam. Active energy modulation for longitudinal bunching in a X-ray free-electron laser was proposed by Hermann et al. [33]. Passive energy modulation by wake fields was already implemented with metallic corrugated structures, for example at LCLS [78, 79]. As the analytical model described by Eq. 3.12 shows, the longitudinal wake scales with the inverse square of the gap size. The gap of the metallic structures in the millimeter range can be decreased to the micrometer range in dielectric structures, which increases the wake and thus the modulation strength significantly. Additionally, the Cherenkov wake due to the dielectric material further increases the modulation strength and reduces the required structure length. The advantages of the passive modulation are the simplicity of the experimental setup and the intrinsic synchronisation of the self-fields with the electron beam. A major disadvantage is that there is no additional adjustment possibility once the structure is installed and the beam optics up to the structure are set, in contrast to the laser in the active modulation scheme. However, we can overcome this drawback with a tunable structure. The gap of the already used metallic structures can be adjusted by step motors. Since it is experimentally difficult to move two grating structures with a distance of a few micrometers independently from each other and to align them precisely, I in collaboration with Benedikt Hermann at SwissFEL propose a structure where the gap size varies along the otherwise invariant direction. The adjustment is then made by moving the structure or the electron beam in this direction. A sketch of such a structure and the corresponding longitudinal wake per grating period for different gap sizes is shown in Fig. 3.9a. Changing the gap size changes the strength of the longitudinal wake while leaving the curve shape almost unchanged. If the short-range wake should stay constant and only the long-range effect should be adjusted, a structure with variable groove depth can be used. Fig. 3.9b shows an example and the corresponding longitudinal wake. This is particularly interesting for a bunch distribution in which the wake is excited by a sharp peak followed by a plateau which should be modulated. DLA grating structures with a period length smaller than a few micron have usually feature sizes in the range of a few hundred nanometers. Such structures are manufactured by lithographic techniques like electron beam lithography and reactive ion etching [80]. However, the proposed structures for tunable wake field applications have a period length of 50 µm. For these structures, a subtractive manufacturing technique developed by FEMTOprint® [81] can be used. The technique is based on a two-step process of ultrashort-pulsed laser radiation in the dielectric material, followed by chemical wet etching to selectively remove the exposed material. This process can form three-dimensional shapes with sub-micron precision and high aspect ratio. Pattern created by local modifications of the refractive index by a laser beam can also be used to realize integrated optical components.

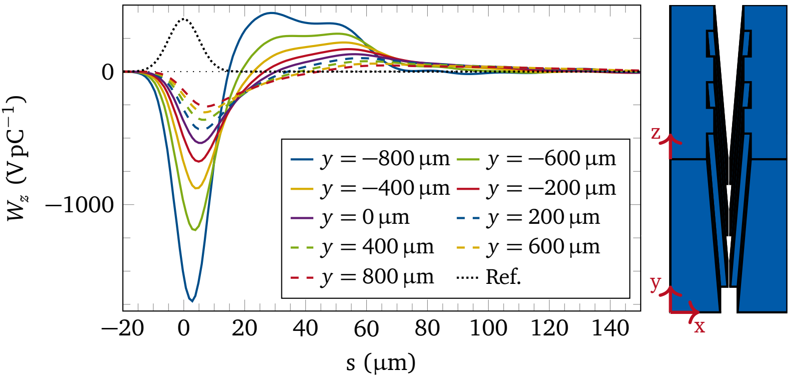

(a) Variable gap size $g(y) = 0.045y + 55$ µm.

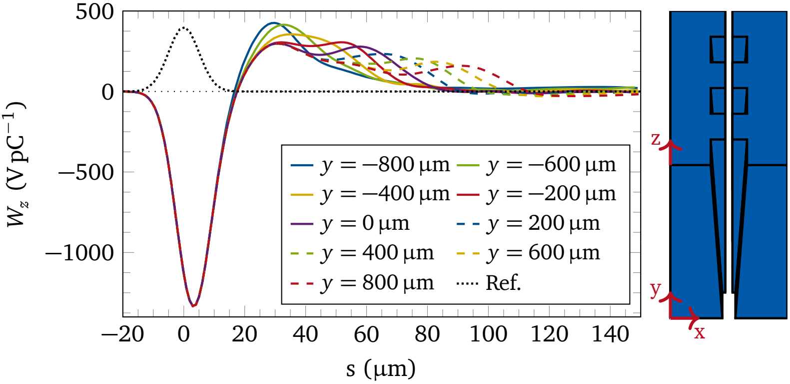

(b) Variable groove depth $d(y) = 0.02y + 30$ µm.

Figure 3.9: Longitudinal wake field per grating period of rectangular gratings with variable gap size or variable tooth height, respectively. The gratings made of fused silica have a period length of 50 µm and a groove width of 25 µm. The grating in (a) has a groove depth of 25 µm. The gap of the grating in (b) has also a size of 25 µm.

3.3 Transverse Wake Field

Transverse wake fields lead to deflecting and (de-)focusing forces. We can distinguish between coherent and incoherent effects. A coherent motion describes the center of mass motion of the entire bunch, e.g. oscillations due to an injection offset. The incoherent motion describes the motion of each individual particle in the bunch, e.g. by defocusing forces. The transverse wake can be expanded in a series of multipole moments of the test particle. The first existing transverse moment, the dipole wake, results in a coherent deflection of the particles depending only on the longitudinal and not on the transverse coordinates. The dipole wake vanishes for a bunch passing a symmetric structure along the symmetry axis. The next-order moment, the quadrupole wake, results in an incoherent motion by focusing or defocusing. As an example, Fig. 3.3b shows the transverse wake of a Gaussian bunch distribution passing centered through a symmetric rectangular grating, which leads to defocusing in the y-direction. In a non-symmetric grating, the dipole wake does not vanish, which results in a deflection (see Fig. 3.8c). The same happens for a bunch that is not centered, i.e., moves through the grating structure with a transverse offset (see Fig. 3.10a). In contrast to the longitudinal wake of a single particle which affects the particle itself, the transverse wake at the particle position is zero (see Sec. 1.3). This implies that the head of a bunch distribution is not deflected, but it deflects the tail in a banana shape towards the grating structure.

In a conventional accelerator, the bunch distribution is much smaller than the aperture. Therefore, the transverse dipole wake can be linearized as a function of the transverse offset. In a dielectric grating, the aperture is almost filled by particles. However, as long as the offset is small in comparison to the aperture, the same linearization can be done in a dielectric grating (see Fig. 3.10b). If the offset is too large, the non-linear wake response requires tracking of the particles in the full wake potential $\vec{W}(x, y, s)$ instead of linear analytical models. A tracking scheme with wake kicks is introduced in Sec. 5.3 and tracking results are included in the discussion of intensity effects in Chapter 6.

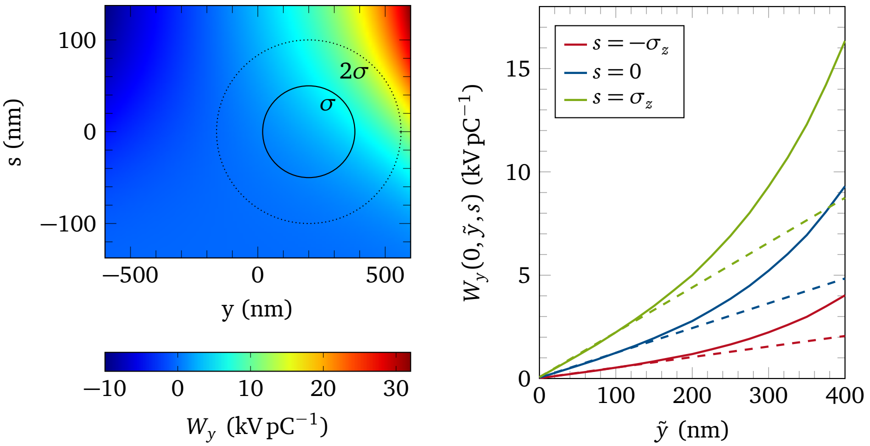

(a) Transverse wake per grating period of a bunch injected with 200 nm offset

(b) Transverse wake as a function of the injection offset evaluated at different longitudinal positions in the bunch (tangent as dashed line)

Figure 3.10: Transverse wake potential per grating period of a bunch injected with an offset in y-direction. The assumption of a linear dependence of the wake on the offset is only fulfilled for an offset significantly smaller than the aperture.

4 Wake Field Measurements

The first experiment to measure wake field effects in DLA grating structures took place at SwissFEL, the X-ray Free Electron Laser facility at the Paul Scherrer Institute in Switzerland [82]. The experiment was mainly conducted by Benedikt Hermann and Rasmus Ischebeck. Section 4.1 summarizes the experimental setup and the performed measurements. The experimental results are compared to tracking simulations including the longitudinal wake field in the DLA grating structure. The corresponding wake field simulations are presented in Sec. 4.2. Section 4.3 concludes the chapter by showing the comparison of measured and simulated energy spectra.

4.1 Setup and Measurements

The experiment analyzes the modifications in the energy spectrum caused by the longitudinal wake field of a rectangular DLA grating structure. The grating contains 100 periods with a period length of 50 µm and an aperture, and a tooth height and width of 25 µm each (see Fig. 4.2). It is made of fused silica ($\varepsilon_r = 4$) by a subtractive technique developed by FEMTOprint® [81] (cf. Sec. 3.2.3). The grating is mounted on a sample holder which is placed on a hexapod with nanometer adjustment accuracy (see Fig. 4.1a). A hexapod is a parallel manipulator that has usually six prismatic actuators attached in pairs to three positions on a baseplate, crossing over to three mounting points on a top plate. The sample holder on the top plate can be moved in six degrees of freedom with nanometer accuracy.

The experimental vacuum chamber contains the hexapod with up to five samples and two permanent magnetic quadrupole triplets, one triplet to focus the electron beam into the structure and a second after the structure to match the electron beam into the downstream lattice of the linear accelerator (see Fig. 4.1b). The SwissFEL facility consists of an injector section, two linac sections and two beamlines: the Aramis beamline with an additional linac section, undulators, a hard X-ray photon beamline and experimental areas and the Athos beamline with undulators, a soft X-ray photon beamline and experimental areas. The chamber is placed in the switchyard to the Athos beamline at an energy of about 3 GeV. For more details on the experimental chamber and the electron beam optics see [34, 83] and App. A.1.1.

In order to ensure that the electron beam size is sufficiently small to fit into the aperture of the grating structure, the beam size is measured by a nanofabricated wire scanner mounted at one of the sample holders at the interaction point. The device contains a conductive wire, which is transversely moved step by step through the beam. For each

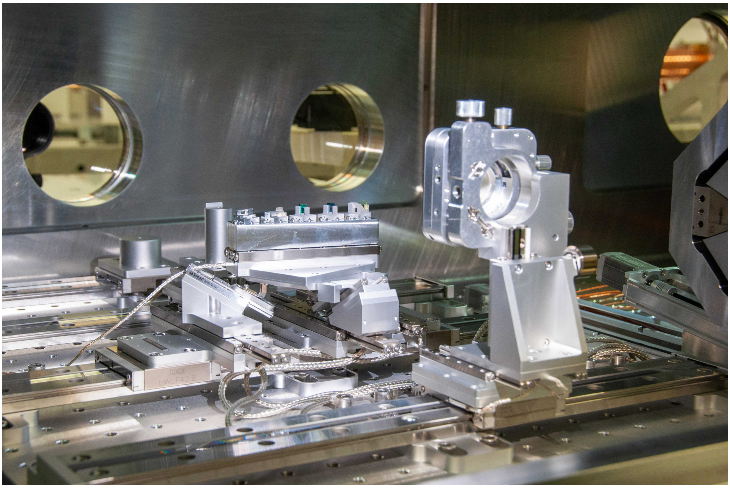

(a) Sample holder mounted on the hexapod.

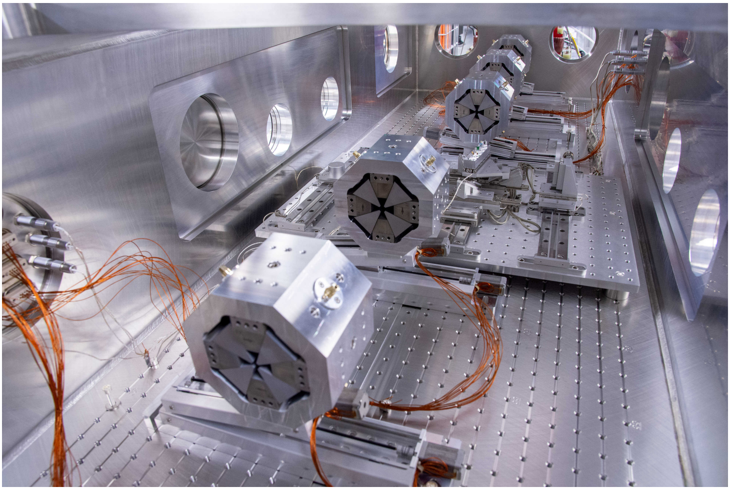

(b) Five of the six installed permanent magnetic quadrupoles with sample holder in the middle.

Figure 4.1: Experimental chamber at SwissFEL. Courtesy of Benedikt Hermann (PSI).

wire position, the forward scattered primary and secondary electrons are detected by a beam loss monitor (BLM). The BLMs at SwissFEL are scintillator fibers placed around the beam pipe which are triggered by out-vacuum scattered electrons [84]. The measured loss intensities allow a reconstruction of the bunch distribution perpendicular to the wire direction. The resolution depends on the wire thickness. The used nanofabricated wire scanners provide a sub-micron resolution [85]. Furthermore, a specific geometrical star-shaped arrangement of the wires enable the reconstruction of the full transverse beam distribution at the interaction point.

In order to align the grating structure to the electron beam, the BLM is evaluated, whereby the wire scanner is replaced by the grating structure. A particle loss due to the passing through the grating structure with 5 mm of dielectric material is clearly visible in the BLM data. The angular alignment is done by measuring the particle loss on an outer edge of the structure while moving the structure transversely. If the structure is perfectly aligned parallel to the electron beam, the outer edge acts like a step-function and the particle loss as function of the transverse position of the structure directly represents the bunch shape. If the structure is rotated, the depth of the penetrated material increases linearly. That flattens the particle loss function.

For measuring the energy spectra, magnets of the beam line can be used. The switchyard, where the experimental chamber is located, contains four dipole magnets. The last dipole magnet can serve as spectrometer magnet. Additionally, the longitudinal phase space is measured by a transverse deflecting cavity (TDC) in the injector diagnostic section at a beam energy of 330 MeV about 200 m in front of the switchyard [86]. Such a cavity projects the time axis on one of the transverse axes, called streaking. By placing the screen at a location of large momentum dispersion, the slice energy spread is projected on the other transverse axis. The screen thus directly images the longitudinal phase space. However, the nominal transverse beam size represented by the beta functions and the point spread function of the screen imaging system limit the temporal and energy resolution [87]. Additionally, the TDC measurements indicate a possible transverse offset or transversely asymmetrical distribution of the bunch. There are two zero-crossings in one period of the sinusoidal TDC potential. At these zero-crossings, a particle in the cavity center does not receive a transverse kick. A transversely symmetric bunch only changes the sign of the deflection from one zero-crossing to the other, i.e., the measurement results are mirror-symmetric. An asymmetric behaviour in the measurement results thus indicates an asymmetry in the transverse bunch distribution.

The desired longitudinal bunch distribution for wake field measurements is a profile with a sharp, strong peak at the beginning and a long low charge tail. This tail probes the wake field excited by the strong peak. Special settings in the electron source, the accelerating cavities, and the bunch shaping elements of SwissFEL provide such a bunch profile. During the measurements, the settings were slightly changed to analyze different bunch distributions. For each setting, the energy spectra with and without grating structure, the bunch charge, and the longitudinal phase space were measured.

4.2 Wake Field Simulations

The accompanying simulations are divided into two parts. The first part is a particle tracking simulation from the transverse deflecting cavity to the DLA interaction point. This simulation was performed by Benedikt Hermann with elegant, which is a 6D tracking code using transfer matrices and models for longitudinal space charge, wake fields and coherent synchrotron radiation in the conventional accelerator lattice [88]. Starting point of the tracking simulation is the reconstructed particle distribution from the TDC measurements. The particles were tracked through about 200 m accelerating lattice including two linac sections and elements for phase space manipulations. The tracking results at the interaction point can be compared to the measured energy spectra without DLA grating structure. The second part, the wake field simulation, takes these tracking results as input, since the tracked charge distribution at the interaction point is used as excitation signal for the CST wake field solver (see Fig. 4.2). The energy gain or loss by the wake potential is then added to the particle energy depending on the respective longitudinal position and the resulting energy spectra can be compared to the measured energy spectra with DLA grating period (see Sec. 4.3). The workflow is summarized in Fig. 4.3.

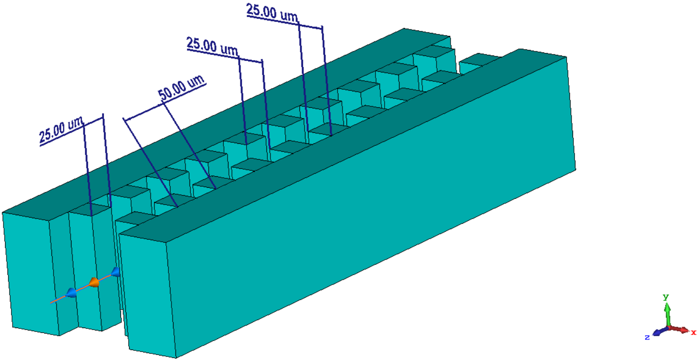

Figure 4.2: CST model of the DLA grating structure with 10 periods made of fused silica ($\varepsilon_r = 4$ at $\lambda_0 = 50\,\mu\text{m}$, cf. Fig. I.1).

The simulated structure is already described in Sec. 4.1. The corresponding CST model is shown in Fig. 4.2. In order to calculate the wake potential, the electromagnetic fields are excited in the center of the channel. The mesh cell size is chosen such that there are minimal ten mesh cells per rms width of the smallest peak in the charge distribution. Since the charge distribution is significantly smaller than the grating period, the mesh cell size is independent of the specific grating structure. Due to symmetry,

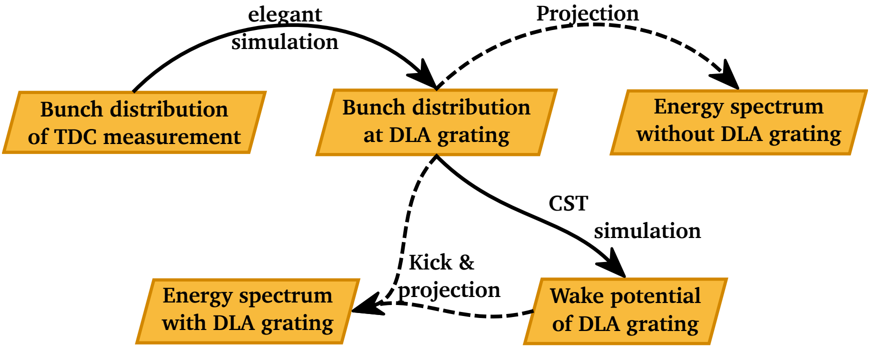

Figure 4.3: Workflow for tracking and wake field simulations.

it is only necessary that the mesh covers a quarter of the structure. The performed simulations were only possible in this way, since the required resolution has already used the for this study available computational resources of high performance single PCs. Figure 4.4 shows the longitudinal wake potential for different mesh cell sizes and number of periods. These results serve as a justification for the chosen simulation parameters. First, Fig. 4.4a shows the longitudinal wake potential per DLA grating period for different mesh cell sizes Δz. The simulation model consists of 10 grating periods. The curves of a mesh cell size smaller than 200 nm agrees very well. However, the enlargement indicates that position and value of the peak are sufficiently but not yet fully converged. Instead, the peak of the wake potential still varies by about 2.5 % or 0.1 kV pC^{-1}, which corresponds to an energy modulation of 0.1 MeV for 100 grating periods and 10 pC bunch charge. Second, Fig. 4.4b shows the longitudinal wake potential per DLA grating period for different numbers of grating periods in the simulation model. The used mesh cell size corresponds to the best resolution in Fig. 4.4a. The deviations between the results of the simulations with 8 and 10 grating periods are in the same range of the previous convergence study in Fig. 4.4a. Thus, the mesh used for the following simulations has a cell size of 130 nm and the simulation model is 10 grating periods long.

With these settings, the wake potentials of various charge profiles are calculated and presented in Fig. 4.5. The plot shows that the wake potential depends significantly on the charge profile. Each wake potential peak follows about 2 µm behind the charge peak and the maximum wake magnitude depends on the width of the current peak, the narrower the current peak, the stronger the wake peak. Note that the current profile plotted in blue is not sufficiently resolved by the mesh, which leads to the non-physical non-zero wake potential at $s \leq 0$ µm. The charge profile of the convergence study in Fig. 4.4 corresponds to the green curve.

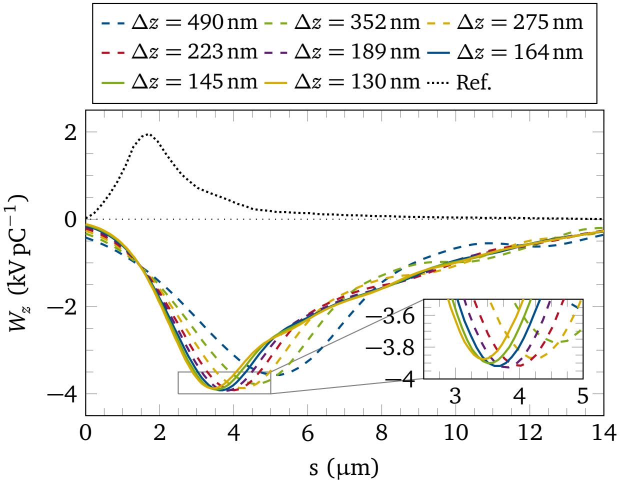

(a) Longitudinal wake field per DLA grating period for different mesh cell sizes. Δz is the length of a mesh cell in z-direction.

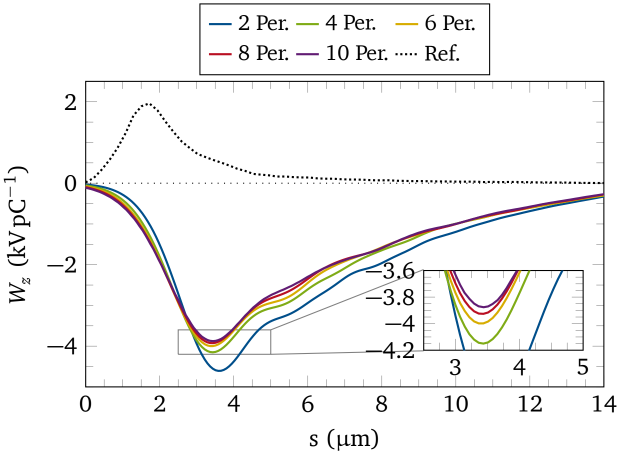

(b) Longitudinal wake field per DLA grating period for different numbers of periods.

Figure 4.4: Longitudinal wake fields of the rectangular structure used in the SwissFEL experiment per DLA grating period for different mesh cell sizes and numbers of periods, respectively.

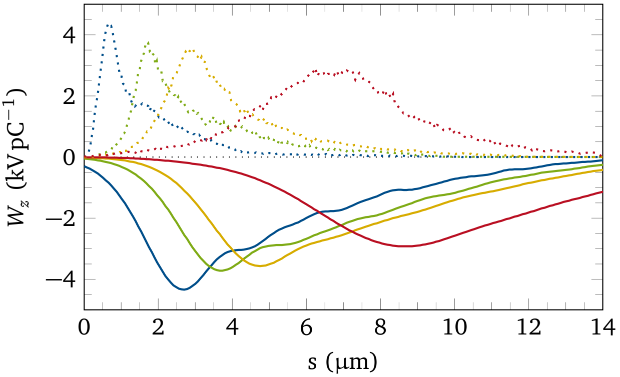

Figure 4.5: Longitudinal wake field per DLA grating period (solid lines) for different bunch profiles (dotted lines).

The four presented profiles correspond to reconstructed longitudinal phase spaces of TDC measurements with different beam line settings. Since the distance between the charge peak and the peak in the wake potential is larger than the width of the charge peak, the simulations meet the experimental expectations, that the wake is driven by the narrow peak at the beginning of the charge profile and modifies the longer tail of the profile.

4.3 Comparison between Experiment and Simulations

Goal of the experiment is the energy modulation of a bunch by the interaction with a DLA grating structure and the comparison with simulations. As described in Sec. 4.2, the wake potential depends significantly on the longitudinal charge profile of the bunch passing through the DLA grating structure. Since a measurement of the longitudinal phase space can not take place in the experimental chamber (cf. Sec. 4.1), the correct reconstruction of the phase space out of the TDC measurement about 200 m in front of the experimental chamber and the tracking through the SwissFEL lattice up to the DLA grating is very crucial. Thereby, it has to be considered, that the measured slice energy spreads are resolution limited by the point spread function of the screen and also a convolution of the nominal slice energy spreads and the nominal transverse beam size. As an approximation, the nominal slice energy spread σ_E is smaller than the measured energy spread $\sigma_{E,\mathrm{TDC}}$ as [87]

$$\sigma_E = \sqrt{\sigma^2_{E,\mathrm{TDC}} - \alpha_1 \sigma^2_y - \alpha_2 \sigma^2_{\mathrm{screen}}}, \tag{4.1}$$

where α_1 and α_2 are constant parameters. An example of a reconstructed and tracked longitudinal phase space is shown in Fig. 4.6a. The phase space projection on the time axis corresponds to the dotted yellow charge profile in Fig. 4.5. The energy modulation is then added to the initial energy of each particle depending on its longitudinal position. In this example, it is only an energy loss. The resulting phase space after DLA interaction is also plotted in Fig. 4.6a. Therein, the head of the bunch remains almost constant and the tail is shifted to lower energies. Furthermore, the shape of the wake yields an increased curvature in the longitudinal phase space resulting in a narrow peak in the energy spectrum followed by a broad tail (see Fig. 4.6b). The simulated spectrum and the spectra of 50 consecutive measurements (see Fig. 4.6c) almost match. The peak location is the same in both spectra with DLA interaction. This indicates that the simulated wake potential has the correct magnitude. A stronger wake potential would shift the peak to smaller energies, a weaker wake potential would shift the peak to larger energies. The peak in the simulated spectrum is however broader and smaller than in the measured spectra. The shape of the tail in the simulated energy spectrum is also not shown correctly. The tail is much broader and the sharp bend, visible at $\Delta E = 0\,\mathrm{MeV}$ in the measured spectra, does not exist in the simulated spectrum. The differences are possibly caused by small deviations in the reconstructed longitudinal phase space. This is most likely true, since even the energy spectra without structure do not correspond completely. Thus, the reconstructed and tracked charge profile does not completely correspond to the real profile either.

These differences become even more apparent for a distribution in the longitudinal phase space, which is more complicated. For this, an exemplary measurement was done with different beam line settings. The simulation and measurement results are shown in Fig. 4.7. The corresponding charge profile and the longitudinal wake potential are plotted as blue curves in Fig. 4.5. While the energy spectra of 50 consecutive measurements with DLA interaction show two distinct peaks, four peaks are visible in the simulated spectrum. Two of these are at similar positions as the measured peaks and the entire range of both spectra with DLA interaction is the same. This implies that the magnitude of the simulated wake potential is correct. Possible reasons for the two additional peaks are the following: As shown in Fig. 4.5, the peak in the charge profile is very small. Therefore, the wake potential simulation is not fully converged. The expected deviation in the wake potential is however not that large (cf. Fig. 4.4a). The discrepancy is rather due to the phase space reconstruction. In the TDC measurement, the slice energy spread is resolution limited. Thus, the slice energy spread in the reconstructed longitudinal phase space is too large. A smaller slice energy spread would lead to an even narrower peak in the charge profile. Furthermore, the TDC measurement indicates, that the transverse bunch distribution is not symmetric. However, the transverse particle distribution has been neglected so far. If the charge peak, which drives the wake, has a transverse offset, the wake potential is slightly stronger and shifted closer to the peak. If the modulated tail has a transverse offset, the wake is weaker and shifted further away from the peak.

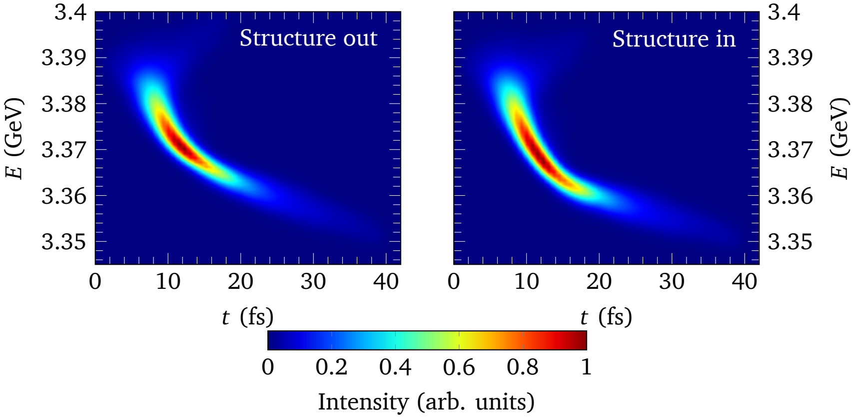

(a) Longitudinal phase space without (left) and with (right) DLA wake field effect.

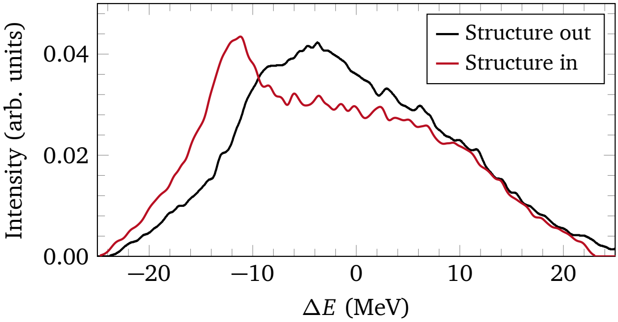

(b) Simulated energy spectra with mean energy at 3.3733 GeV.

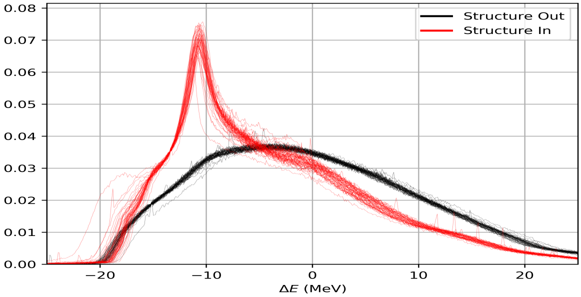

(c) Measured energy spectra of 50 consecutive shots (preliminary data plotted by Benedikt Hermann, PSI).

Figure 4.6: Phase spaces and energy spectra with and without DLA grating structure for an experimental setting where simulation and measurement almost match.

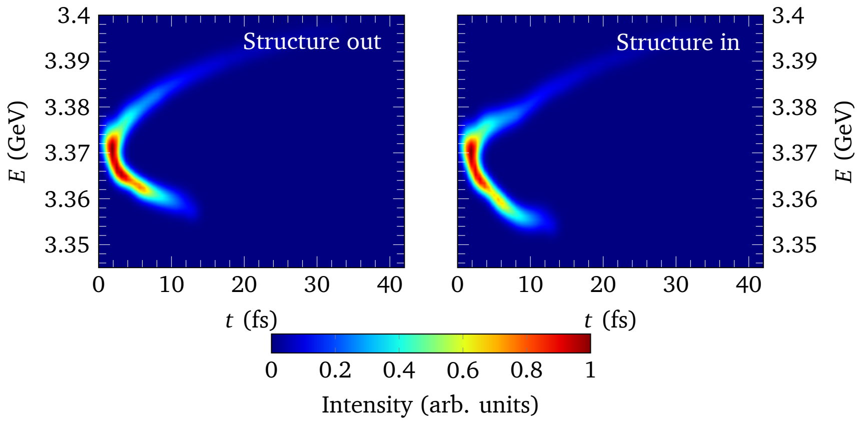

(a) Longitudinal phase space without (left) and with (right) DLA wake field effect.

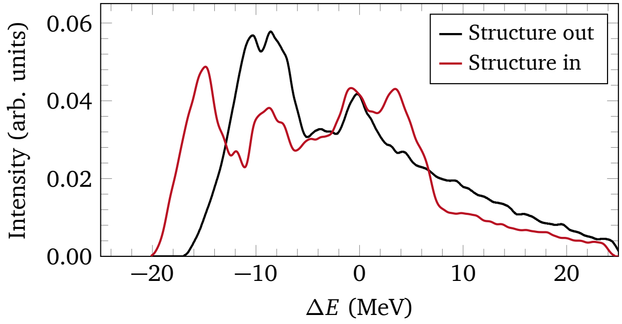

(b) Simulated energy spectra with mean energy at 3.3723 GeV.

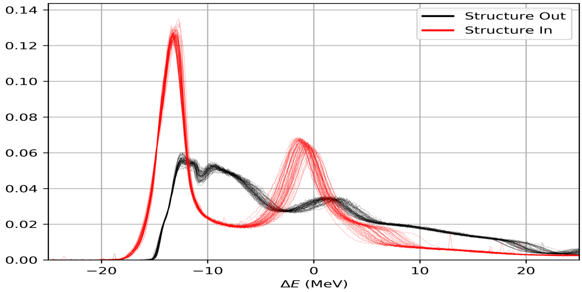

(c) Measured energy spectra of 50 consecutive shots (preliminary data plotted by Benedikt Hermann, PSI).

Figure 4.7: Phase spaces and energy spectra with and without DLA grating structure for an experimental setting where simulation and measurement do not match.

The identification of these possible reasons can be used to improve the measurements in upcoming beam times. The crucial aspect is the most exact reconstruction of the phase space. For this purpose, both the longitudinal and the transverse phase space should be determined at two positions in the beam line. The first position serves as starting point for the tracking by elegant. The measured phase space at the second position can be compared to the tracking results to verify the tracking accuracy. Measuring the entire phase space distribution after the DLA interaction point is not yet possible. The installation of a TDC with variable polarization at the end of the Athos beam line is planned for 2021. This device would enable a precise characterization of the full phase space with and without wake field interaction [89]. Before the additional diagnostics are installed, at least a projection of the longitudinal phase space can be compared with the energy spectrum, as already described. The same is also possible with a wirescanner measurement for the projection of the transverse phase space (see Sec. 4.1). With these measurements it is possible to adjust the beam line settings so that the phase space distribution is suitable for reconstruction. Especially, the measurement of the slice energy spread should not be limited by the achievable resolution and the charge profile should be wide enough to obtain a fully converged solution of the wake potential. In the past beam times, the focus was rather on a clear and strong wake effect. Nevertheless, the presented measurement results have shown wake field effects in DLA structures for the first time and confirmed the applied wake field simulations.

5 Particle Tracking

In order to analyze the non-linear dynamics of electrons passing a DLA grating structure (cf. Chapter 2), particle tracking simulations are needed. One option is a particle-in-cell simulation. Since an usual DLA lattice consists of a few thousand grating periods, such a particle-in-cell simulation with the full electromagnetic fields is computationally very expensive. The analytical description of the kicks acting on the particles offers a second option: a tracking scheme with only one kick per particle per grating period based on the spatial harmonics presented in Sec. 2.1. We have developed the tracking code DLAtrack6D [31] introduced in Sec. 5.1. Tracking examples for the purpose of lattice design and analysis of single particle dynamics are shown in Sec. 5.2. Adding wake kicks to the tracking scheme allows simulating collective effects. These kicks are explained in Sec. 5.3.

5.1 DLAtrack6D

The laser fields in a DLA grating period can be expanded in a spatial Fourier series (Eq. 2.2). Due to the synchronicity condition (Eq. 2.5), energy gain and transverse momentum change per grating period can be calculated by only one synchronous spatial harmonic (Eqs. 2.16 and 2.17c). In the following, the discussion is restricted to the first spatial harmonic, which is usually the strongest. The tracking is applied on the phase space coordinates $(x, x', y, y', \varphi, \delta)^T$. These coordinates are introduced in Eq. 1.6 except for the phase φ. For this, the relation to the longitudinal distance from the reference particle is $\varphi = 2\pi s/\lambda_z + \varphi_0$ with the period length λ_z and the synchronous phase φ_0. The reference particle is accelerated according to the acceleration ramp given by Eq. 2.6. The kicks, which are the changes of the momentum deviation per grating period, can be obtained by using Eqs. 2.15 and 2.17c. As in the analysis of the beam dynamics in Sec. 2, the investigated grating structures are invariant in the x-direction. Thus, the kick in this direction vanishes ($\Delta x' = 0$). The kicks for tilted gratings are given in [31]. The kick in y and the change of the relative momentum deviation are

$$\Delta y' = -\frac{i k_y \lambda_0^2 q \beta}{2\pi p_{z0} c_0} \sinh\left(i k_y y\right) \mathrm{Im}\left\{\underline{e}_1^0 \exp\left(i\varphi\right)\right\} \tag{5.1a}$$

$$\Delta\delta = \frac{q\lambda_z}{\gamma m_e c_0^2} \mathrm{Re}\left\{\underline{e}_1^0 \left[\cosh\left(i k_y y\right) \exp\left(i\varphi\right) - \exp\left(i\varphi_0\right)\right]\right\} \tag{5.1b}$$

with the longitudinal momentum p_{z0}, the velocity βc_0, and the energy $\gamma m_e c_0^2$ of the reference particle, the laser wavelength λ_0, the particle charge $q = -e$, the first spatial harmonic $\underline{e}_1^0$ at $y = 0$, and the transverse wavenumber $k_y = 2\pi i/(\beta\gamma\lambda_0)$ (cf. Eq. 2.7). The tracking equations

$$\begin{pmatrix} x \\ x' \\ y \\ y' \\ \varphi \\ \delta \end{pmatrix}^{(n+1)} = \begin{pmatrix} x \\ Ax' + \Delta x' \\ y \\ Ay' + \Delta y' \\ \varphi \\ \delta + \Delta\delta \end{pmatrix}^{(n)} + \begin{pmatrix} \lambda_z x' \\ 0 \\ \lambda_z y' \\ 0 \\ -\frac{2\pi}{\beta^2\gamma^2}\delta \\ 0 \end{pmatrix}^{(n+1)} \tag{5.2}$$

represent an Euler scheme applying first the explicit kicks in the nth DLA period followed by the implicit pushes of the coordinates to calculate the 6D phase space of the $n+1$th DLA period. Figure 5.1 depicts this tracking workflow. The constant A describes the adiabatic damping in the transverse planes by

$$A^{(n)} = \frac{(\beta\gamma)^{(n+1)}}{(\beta\gamma)^{(n)}} = 1 + \left(\frac{\lambda_0 q \mathrm{Re}\left\{\exp(i\varphi_0)\underline{e}_1^0\right\}}{\beta\gamma m_e c_0^2} \right)^{(n)} . \tag{5.3}$$

With the determinant of the Jacobian matrix

$$\det \frac{\partial\left(x, x', y, y', \varphi, \delta\right)^{(n+1)}}{\partial\left(x, x', y, y', \varphi, \delta\right)^{(n)}} = A^{(n)^2} \tag{5.4}$$

the symplecticity of the tracking scheme is confirmed, if the velocity of the reference particle does not change, and the tracking thus becomes phase space preserving. In case of acceleration, the tracking scheme is not strictly symplectic due to the use of $x' = p_x/p_z$ and $y' = p_y/p_z$ instead of p_x and p_y. However, the deviation is only caused by adiabatic damping and the normalized emittance is still preserved.

The tracking scheme called DLAtrack6D was first implemented in Matlab [90] by Uwe Niedermayer. The extended version including self-fields of the particles is implemented in Python [91] in this work. Both versions are based on a vectorized particle distribution which allows very efficient calculations as long as no direct particle particle interaction is included. Initial distributions for the particle tracking are directly imported or created based on the statistical quantities of a Gaussian distribution. The required lattice parameters are the laser wavelength and peak electric field, the synchronous phase of the reference particle, the aperture of the grating structure, the number of DLA grating periods per focusing or defocusing segment, the number of segments, and the structure constant, i.e., the normalized first spatial harmonic $\underline{e}_1^0$, for each DLA grating period. The acceleration ramp and the corresponding period lengths are then calculated based on

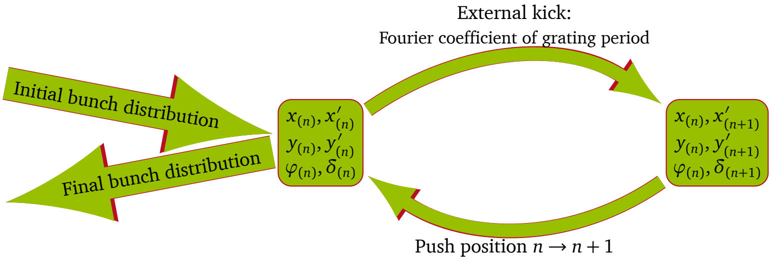

Figure 5.1: Schematic of one step in the tracking loop of DLAtrack6D.

these input parameters. Therefore, a particular structure geometry does not need to be specified. For beam dynamics studies, an ideal structure constant is sufficient. For the comparison with experimental data, the structure constant of a manufacturable grating structure has to be, however, used for tracking. In order to analyze the beam dynamics of an arbitrary grating structure with DLAtrack6D, the structure must have a hyperbolic cosine dependence of the first Fourier coefficient on one transverse coordinate and a (quasi-) periodicity in the longitudinal and the other transverse coordinate. The result of the particle tracking is a phase space evolution, which can be statistically analyzed during tracking or afterwards.

5.2 Tracking Results

The capabilities of DLAtrack6D are illustrated by examples of different lattices and different quantities under investigation. A main field of application is the verification of the design of subrelativistic accelerating lattices and the estimation of the maximum possible emittance. An example is shown in Sec. 5.2.1. The tool can also be used for the tracking of relativistic particles, particularly to study intensity effects due to wake fields. For the confinement of such relativistic beams, an APF lattice can also be applied. Section 5.2.2 summarizes the specifications of an exemplary lattice and the corresponding tracking results. An interesting quantity for beam dynamics studies is the phase advance. It can be reconstructed from the tracking results. An example of such reconstruction is presented in Sec. 5.2.3.

5.2.1 Acceleration of Subrelativistic Electrons

An example for the necessity of tracking is the comparison between linearized motion used for the lattice design and the non-linear motion in the full accelerating potential. For this comparison, an accelerating APF lattice from 83 keV to 1 MeV with an average gradient of 187 MV m^{-1} at a synchronous phase ± 60° off-crest is analyzed. The example is adapted from [32]. The lattice design is done as described in Sec. 2.3: First eigenvalue problems for periodic APF FODO cells are solved and the segment lengths with minimal Twiss beta functions are estimated. Second, small manual corrections make sure that the analytical beta functions remain limited and minimal even in the non-periodic accelerating lattice (see Fig. 2.6). The analytical results agree very well with the numerical tracking results for infinitesimal low emittance. With increasing emittance, the non-linearities increase and the throughput thus decrease. We obtain 93 % transmission for an initial normalized emittance of $\epsilon_\mathrm{n} = 14.82\,\mathrm{pm}$ and 56 % transmission for $\epsilon_\mathrm{n} = 59.27\,\mathrm{pm}$. Figure 5.2 shows the envelopes (see Eq. 1.18) and also the survival rates along the lattice. The envelopes, which are slightly smaller than the analytically calculated ones, indicate that the outer particles are lost by the non-linearities. In order to compare the envelopes of bunches with different emittances, the results for the smaller emittance are shown scaled in the top plot of Fig. 5.2. The longitudinal bunch length is chosen as $\sigma_z = 10\,\mathrm{nm}$. This ensures that the transmission depends only on the initial transverse emittance.

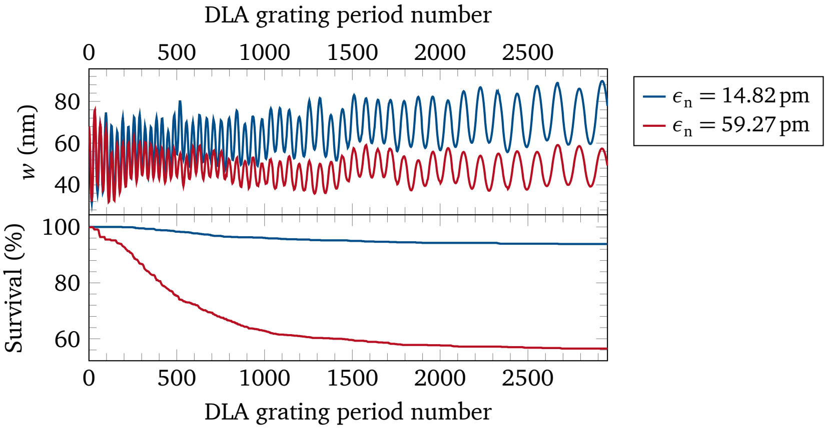

Figure 5.2: Envelopes (top) and survival rates (bottom) of bunches with different emittances passing through an accelerating APF lattice from 83 keV to 1 MeV with an average gradient of 187 MV m^{-1} at a synchronous phase ± 60° off-crest. For comparison, the envelope of the bunch with smaller emittance is scaled to the larger one.

5.2.2 APF Lattice for Relativistic Electrons

For relativistic electrons, the design of an accelerating APF lattice is easier due to the negligible chirp of the period length (cf. Sec. 2.1). However, the focusing strength $\sqrt{K}$ decreases proportional to $\gamma^{-3/2}$ (see Eq. 2.21). The length of an APF FODO cell L has to be modified accordingly along the lattice such that $\sqrt{K}L = \mathrm{const}$. Otherwise, the bunch distribution is not properly matched and additional particle loss occurs. This is confirmed by a tracking example based on a grating structure with an aperture of 480 nm, a grating period length of 0.8 µm, a peak gradient of $560\,\mathrm{MV\,m^{-1}}$, and acceleration at a synchronous phase ±45° off-crest. For a bunch at 6.5 MeV initial energy, the initial focusing strength is (cf. Eq. 2.21)

$$\sqrt{K_0} = \sqrt{\frac{2\pi q}{\beta^3 \lambda_0 m_e \gamma^3 c_0^2} \left|e_{-1}^0\right| \sin(\varphi_0)} \approx 1727.6\,\mathrm{m}^{-1}. \tag{5.5}$$

The top plot of Fig. 5.3 shows the energy ramp and the focusing strength as functions of the DLA grating period number (as longitudinal coordinate along the lattice). Choosing an initial FODO cell length of 1809 DLA grating periods, there is a stable periodic eigenvalue solution with a maximum Twiss beta function of $\hat{\beta}_{y,\mathrm{max}} \approx 2.445\,\mathrm{mm}$. A normalized emittance of $\epsilon_\mathrm{n} = 51.855\,\mathrm{pm}$ yields a transverse beam size of 100 nm. Figure 5.3 compares the tracking results of a lattice with constant FODO cell length and a lattice with increasing FODO cell length in accordance to the change of the focusing strength. In the lattice with increasing FODO cell length, the envelope is confined and the oscillation is visible over the entire length of the lattice. In the lattice with constant FODO cell length, the envelope increases at the beginning until the physical aperture is filled. After that it is no longer well defined and the oscillation by the phase space rotation disappears. Therefore, matching the FODO cell length almost doubles the throughput after 34800 DLA grating periods. This corresponds to a structure length of about 27.8 mm. The same design constraint given by the relation between focusing strength and FODO cell length can be confirmed by calculating the phase advance spectrogram, which is presented in Fig. 5.6 in Sec. 5.2.3.

5.2.3 Phase Advance Calculation

The non-linear spatial dependence of the fields in the dielectric grating leads to a betatron phase advance depending on the particle's amplitude. The linear phase advance is given analytically by Eq. 2.31. Numerically, the full (linear and non-linear) phase advance can be determined by reconstructing the transfer matrix of a FODO cell from the tracking result for each particle. The used transfer matrix reconstruction algorithm is presented by Luccio et al. [92]. For a coupled particle motion, the phase advance can be calculated by the eigenvalues of the 6x6 transfer matrix. The transfer matrix M_if is

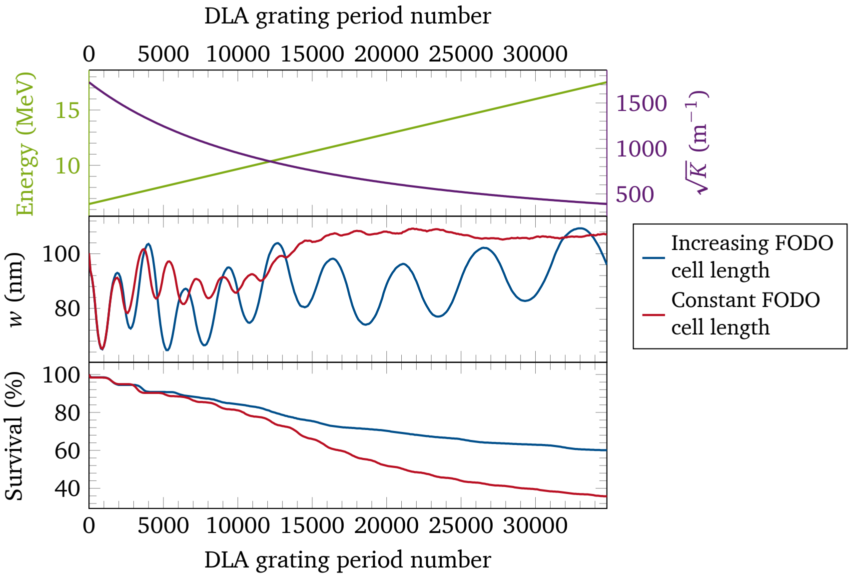

Figure 5.3: Envelopes (middle) and survival rates (bottom) of a particle distribution with 20 nm bunch length and 100 nm transverse size passing through accelerating lattices with constant APF FODO cell length and increasing FODO cell length in accordance to the increasing energy at a synchronous phase 45° off-crest. Energy ramp and focusing strength are shown in the top plot.

determined by solving the system of 36 linear equations between the initial coordinates of a particle and the coordinates after 5 successive FODO cells,

$$x_k^{(n+1)} = \sum_{j=1}^{6} M_{\text{if}}^{k,j} x_j^{(n)}, \tag{5.6}$$

where x_k is the k-th component of the phase space vector $\vec{r}_\text{p}$ (cf. Eq. 1.6), i.e., $k = 1,\ldots,6$, and n is the FODO cell number, i.e., $n = 0,\ldots,5$.

With negligible coupling between planes, only a 2x2 transfer matrix for each dimension,

$$M_{\text{if},u} = \begin{pmatrix} \cos(\mu_u) + \hat{\alpha}_u \sin(\mu_u) & \hat{\beta}_u \sin(\mu_u) \\ -\hat{\gamma}_u \sin(\mu_u) & \cos(\mu_u) - \hat{\alpha}_u \sin(\mu_u) \end{pmatrix}, \tag{5.7}$$

is required, where $\hat{\alpha}_u$, $\hat{\beta}_u$, and $\hat{\gamma}_u$ are the Twiss parameters (cf. Sec. 1.2). Therefore, the system of equations in Eq. 5.6 is reduced to 4 linear equations and we need only two subsequent FODO cells for the transfer matrix calculations. The phase advance μ_u is then given by the arccosine of half the trace of the matrix (cf. Eq. 1.9). Figure 5.4 shows the distributions of the transverse phase advance for a particle distribution with negligible emittance, which exactly confirms the analytical value $\mu_y = 1.3642$. With a realistic emittance, the distribution shows the expected broadening. Usually the phase advance is calculated by a Fast Fourier Transform (FFT). Applying a FFT along 2500 FODO cells to determine the phase advance spectrum yields the same mean value. Such a large number of FODO cells is required to achieve a sufficient resolution in the spectrum. However, one has to account for the increased particle losses during this long time scale. In particular, particles with large amplitudes have a large tune deviation and are likely to be lost, which explains the narrowing of the spectrum in Fig. 5.4.

Physically, the spread is explained as follows: A larger transverse emittance leads to larger particle amplitudes. Since $\Delta y' \propto \sinh\left(ik_y y\right) \to ik_y y$ for $\gamma \to \infty$ (see Eq. 5.1a), this gives a stronger focusing and a spread towards larger transverse phase advance. A larger longitudinal emittance leads also to larger amplitudes in the longitudinal plane. However, focusing becomes weaker and creates a spread towards smaller transverse phase advances. In comparison, for the longitudinal phase advance there is no spread towards larger values since $\Delta\delta \propto \cosh\left(ik_y y\right) \to 1$ for $\gamma \to \infty$ (see Eq. 5.1b). Both phase advance distributions, longitudinal and transverse, are shown in Fig. 5.5.

Furthermore, the calculation of the phase advance as trace of the transfer matrix requires a very limited number of subsequent FODO cells, only two FODO cells if coupling between planes is negligible. This allows a moving window approach to obtain a spectrogram, in order to analyze the temporal variation of the phase advance e.g, in case of acceleration. As described in Sec. 5.2.2, a technique for lattice design is based on varying the length of a FODO cell along the lattice to keep the phase advance per FODO cell con-

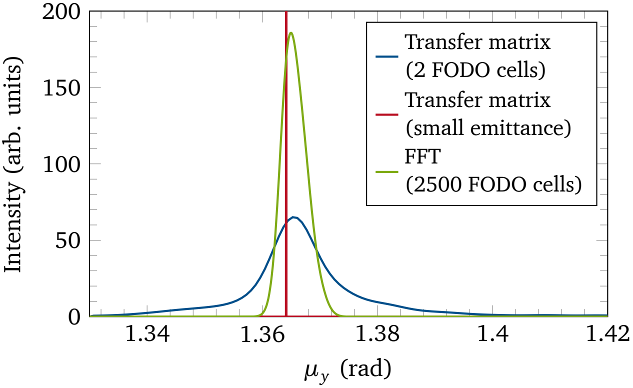

Figure 5.4: Transverse phase advance per FODO cell for a negligible emittance in complete agreement with the analytical $\mu_y = 1.3642$ and a distribution with 20 nm bunch length and 100 nm transverse size. The latter is obtained by both FFT and the transfer matrix reconstruction method. The narrowing of the FFT curve originates from high amplitude particle losses over the long (2500 FODO cells) transport distance (adapted from [43, Fig. 11]).

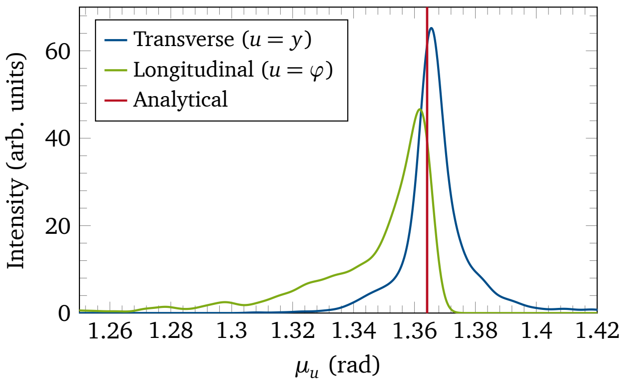

Figure 5.5: Longitudinal and transverse phase advance per FODO cell for a distribution with 20 nm bunch length and 100 nm transverse size. The analytical linear phase advance is $\mu_y = 1.3642$.

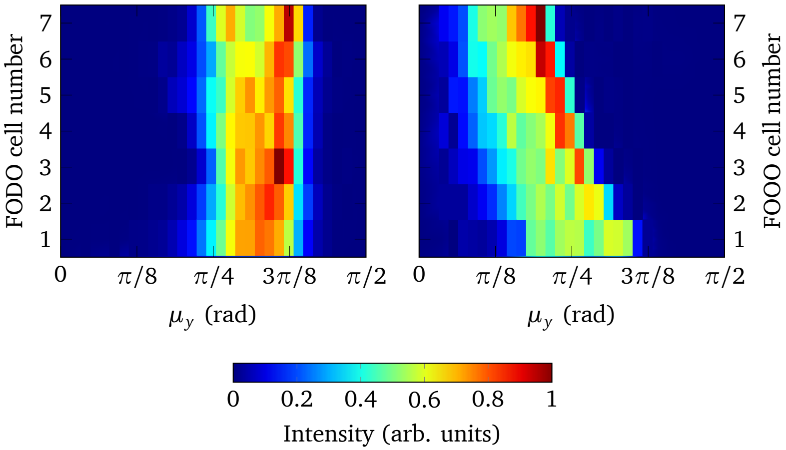

Figure 5.6: Spectrograms of the transverse phase advance per FODO cell for a particle distribution accelerated in an APF grating structure with 0.8 µm period length. Increasing the FODO cell length along the structure in accordance to the increasing energy keeps the phase advance distribution almost constant (left). A constant FODO cell length, however, leads to a decreasing phase advance (right) (adapted from [43, Fig. 12]).

stant and thus the beam envelope bounded. The left plot in Fig. 5.6 shows the spectrum of the transverse phase advance for an accelerator design with increasing FODO cell length such that the designed linear phase advance on the acceleration ramp remains almost constant. The applied lattice design is presented in Sec. 5.2.2. By defining the length at the beginning of the respective next FODO cell, although the energy increases along the FODO cell, the mean of the phase advance distribution is slightly shifted towards higher values along the lattice. The right plot shows the spectrum for a constant FODO cell length. In this case, the phase advance decreases over time. The width of the distributions is composed of both the intrinsic width of the particle distribution and the numerical error that results from the calculation of the transfer matrix using two subsequent FODO cells, which are only approximately but not exactly identical.

5.3 Wake Kicks

Similar to the non-linear external fields the wake fields are also non-linear, especially for bunch distributions filling almost the full aperture of the dielectric grating structure. Furthermore, wake effects possibly change the bunch distribution significantly.

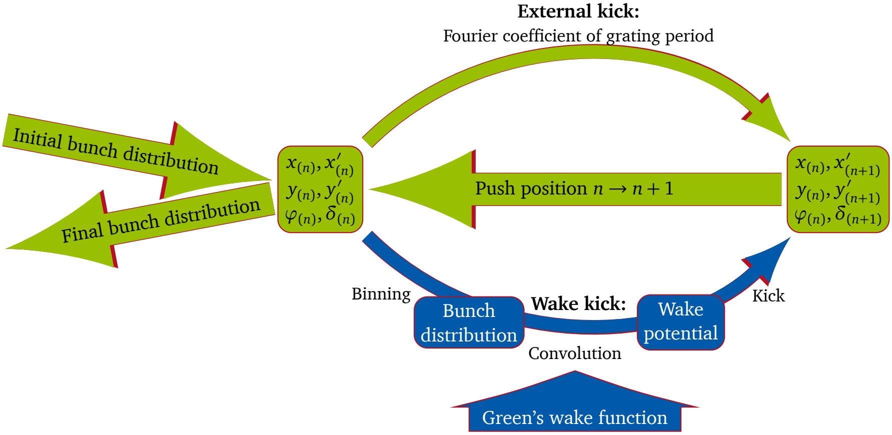

Figure 5.7: Schematic of one tracking step of DLAtrack6D with wake kick.

Linearized analytical wake models are thus not sufficient for studying intensity dependent beam dynamics. Instead tracking with position dependent evaluation of the wake is essential. In this thesis, wake kicks were included to the tracking tool DLAtrack6D (introduced in Sec. 5.1). The extended tracking scheme is shown in Fig. 5.7. The external kick depends only on the particle laser interaction and can be calculated independently for each individual particle. In contrast, the wake kicks depend on the current particle distribution. Hence, the calculation of the wake kicks in each grating period starts with particle binning to determine the bunch distribution. The wake potential results from a convolution of the Green's wake function with the bunch distribution, which can be written as three tensor products (cf. Eq. 3.10). Evaluating the collective wake potential $\vec{W}(x, y, s)$, that applies to all particles, at the particle coordinates $\left(x_\mathrm{p}, y_\mathrm{p}, s_\mathrm{p}\right)$, the wake kicks for each particle can be calculated as

$$\Delta x'\left(x_\mathrm{p}, y_\mathrm{p}, s_\mathrm{p}\right) = \frac{q\, q_\mathrm{bunch}}{p_{z0}\beta c} W_x\left(x_\mathrm{p}, y_\mathrm{p}, s_\mathrm{p}\right), \tag{5.8a}$$

$$\Delta y'\left(x_\mathrm{p}, y_\mathrm{p}, s_\mathrm{p}\right) = \frac{q\, q_\mathrm{bunch}}{p_{z0}\beta c} W_y\left(x_\mathrm{p}, y_\mathrm{p}, s_\mathrm{p}\right), \tag{5.8b}$$

$$\Delta \delta\left(x_\mathrm{p}, y_\mathrm{p}, s_\mathrm{p}\right) = \frac{q\, q_\mathrm{bunch}}{E_0} W_s\left(x_\mathrm{p}, y_\mathrm{p}, s_\mathrm{p}\right) \tag{5.8c}$$

with the particle charge q, the bunch charge q_bunch. Moreover, E_0 is the energy, β is the velocity, and p_{z0} is the longitudinal momentum of the reference particle. The wake kicks (Eqs 5.8) are then added to the kicks by the external laser field (Eqs. 5.1). Due to the discrete manner of the determined bunch distribution and the Green's wake function calculated as described in Sec. 3.1, all convolutions are implemented as matrix multiplications. This makes the calculation fast and efficient, such that it can run on an ordinary PC. The upgraded version of DLAtrack6D including wake kicks is applied in the studies of wake field effects presented in Chapter 6.

6 Intensity Effects

The strength of wake fields depends on the bunch charge. For a fixed bunch distribution, this dependency is linear. As the beam intensity is increased, the wake fields alter the external fields. When the perturbations become sufficiently strong, instabilities can occur. The analysis of intensity effects and collective instabilities in DLA grating structures is discussed in this chapter. Section 6.1 elaborates beam loading as the longitudinal intensity effect. The sections 6.2 and 6.3 describe two transverse intensity effects in different beam energy ranges: first the transverse beam breakup for high-energy beams with frozen synchrotron motion and second the head tail instability for lower energies where the synchrotron motion has to be taken into account. The following studies are focused on single bunch effects caused by the short-range wake fields: The long-range wake fields are radiative and decrease exponentially [37], thus can be neglected.

6.1 Beam Loading

The total energy loss of a bunch by the longitudinal wake field is described as beam loading [59] (cf. Sec. 1.3). It is given by $\Delta E_{\mathrm{loss}} = q_{\mathrm{bunch}}^2 k_{\mathrm{loss}}$, where k_{loss} is the loss factor as introduced in Eq. 1.28. The beam loading intensity limit is defined by the bunch charge at which the total energy loss equals the total energy gain by an external (laser) field. For example, the beam loading limit of a rectangular grating structure is calculated in the following. For a 30 nm bunch, the longitudinal wake field per grating period of 0.8 µm is plotted in Fig. 3.5a. The total energy gain of the bunch per grating period for on-crest acceleration at a gradient of $1\,\mathrm{GV\,m^{-1}}$ is

$$\Delta E_{\mathrm{gain}} = q_{\mathrm{bunch}} \int_{-\infty}^{\infty} 1\,\mathrm{GV\,m^{-1}} \cos\left(\frac{2\pi s}{0.8\,\mu\mathrm{m}}\right) \lambda(s)\,\mathrm{d}s \tag{6.1a}$$

$$\approx q_{\mathrm{bunch}} \cdot 778\,\mathrm{V} \tag{6.1b}$$

The longitudinal wake potential results in a loss factor of $k_{\mathrm{loss}} \approx 107\,\mathrm{kV\,pC^{-1}}$ and thus a total energy loss of

$$\Delta E_{\mathrm{loss}} \approx q_{\mathrm{bunch}}^2 \cdot 107\,\mathrm{kV\,pC^{-1}} \tag{6.2}$$

Comparing Eqs. 6.1b and 6.2 leads to a bunch charge limit of $q_{\mathrm{bunch,max}} \approx 7.3\,\mathrm{fC}$ (see Fig. 6.1). Below this limit, the position dependent longitudinal wake field has not only

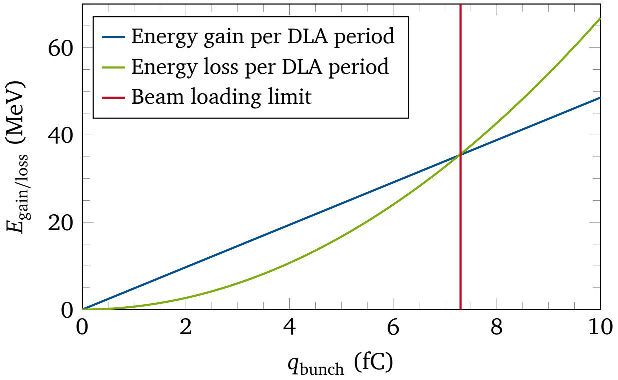

Figure 6.1: Energy gain and energy loss of a Gaussian bunch in one rectangular grating period. The red line symbolizes the bunch charge where the energy loss by beam loading equals the external energy gain (adapted from [42, Fig. 3]).

a detrimental effect, but instead the energy loss by the longitudinal wake can be used to compensate the energy spread by the external field. The voltage seen by the beam is

$$V(s) = V_{\mathrm{laser}}(s) + V_{\mathrm{wake}}(s) \tag{6.3a}$$

$$= \lambda_0 \left| e_{-1}^0 \right| \cos\left(\frac{2\pi s}{\lambda_0} + \varphi_0 \right) + q_{\mathrm{bunch}} W_z(s), \tag{6.3b}$$

where $\left| e_{-1}^0 \right|$ is the peak gradient, λ_0 is the laser wavelength and period length ($\beta \approx 1$), and φ_0 is the synchronous phase. Following [93], the energy spread is compensated, if all the particles near the bunch center are accelerated by the same voltage, i.e., $\partial V(s)/\partial s|_{s=0} = 0$. For the charge in Eq. 6.3, it follows

$$q_{\mathrm{bunch,comp}} = 2\pi \left| e_{-1}^0 \right| \sin(\varphi_0) \left(\left. \frac{\partial W_z(s)}{\partial s} \right|_{s=0} \right)^{-1}. \tag{6.4}$$

In the investigated rectangular grating the energy spread can be compensated up to a bunch charge of $q_{\mathrm{bunch,comp}} = 2.6\,\mathrm{fC}$ but with a significantly reduced gradient due to the chosen synchronous phase. For a reasonable synchronous phase of $\varphi_0 = 135°$, the bunch charge of compensation is $q_{\mathrm{bunch,comp}} = 1.8\,\mathrm{fC}$. In comparison to passive bunch modulation and correction of a previously generated energy spread as in Sect. 3.2.3, this compensation directly acts at the same time as the energy spread generation by the external potential.

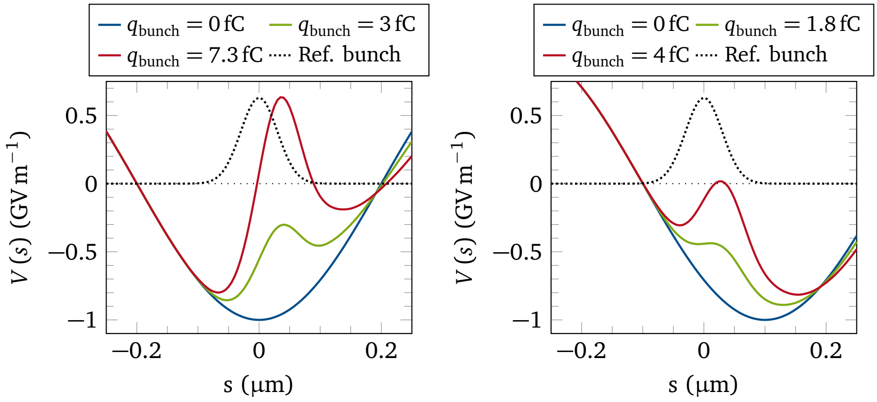

(a) Synchronous phase $\varphi_0 = 180°$ (on-crest)

(b) Synchronous phase $\varphi_0 = 135°$ (45° off-crest)

Figure 6.2: Accelerating potential of a rectangular grating structure as sum of laser potential and longitudinal wake potential for various synchronous phases and bunch charges.

Furthermore, the wake field of the bunch possibly reduces the electromagnetic fields in the dielectric material. If the wake fields are present, it is therefore feasible to use stronger external laser fields without damaging the grating structure. For increasing bunch charge, the short-range longitudinal wake fields counteracting the accelerating fields increase. Thus, the electromagnetic fields in the material decrease but the energy gain decreases at the same time. Hanuka et al showed that there is an optimal bunch charge for either maximal gradient or maximal efficiency [39, 40]. However, using this compensating effect requires accurate synchronization between laser pulse and electron bunch. A very fast feedback system has to ensure that the laser pulse does not enter the structure if the bunch charge is too low. Otherwise, the wake field is not sufficient to push the electromagnetic fields in the dielectric material below the damage threshold and the laser pulse will destroy the structure. Thus, the experimental implementation is very challenging.

6.2 Transverse Beam Breakup

For the analysis of transverse intensity effects, we have to distinguish two regimes: first a regime, where the synchrotron and betatron motions are considered frozen since the instability develops much faster than a synchrotron or betatron period, and second a regime where the motion by external fields and the motion by wake fields are on the same time scale. In order to identify the regime, the strength of the focusing elements in a lattice is crucial. We can choose a constant synchronous phase, at which there is a constant longitudinal focusing (see Sec. 2.2). The synchrotron frequency is the inverse of the focusing strength in Eq. 2.21 multiplied with $v = \beta c_0$,

$$\Omega_s = \sqrt{\frac{2\pi q \left|\underline{e}_1^0\right| \sin(\varphi_0)}{\lambda_0 \beta \gamma^3 m_e}}. \tag{6.5}$$

Therein, $\left|\underline{e}_1^0\right|$ is the accelerating peak gradient given by the first spatial harmonic in the center of the vacuum gap, φ_0 the synchronous phase, and λ_0 the laser wavelength. First, we look at the regime of frozen motion. We consider parameters achievable at the DLA experiment at SwissFEL [34, 33] (see App. A.1.1 for details about SwissFEL), which is a 3 GeV electron beam accelerated with a peak gradient of $\left|\underline{e}_1^0\right| = 1\,\mathrm{GV\,m^{-1}}$ at the synchronous phase $\varphi_0 = 135°$. Following Eq. 6.5, the synchrotron frequency is $\Omega_s \approx 43.9 \times 10^6\,\mathrm{s^{-1}}$. The synchrotron period length is thus $\lambda_s \approx 42.87\,\mathrm{m}$. An APF FODO cell for these parameters would have a length of 8.5×10^6 DLA grating periods or 17 m with a maximal Twiss beta function of $\hat{\beta}_{\max} \approx 29\,\mathrm{m}$. On the other hand, the DLA grating is outlined to be only a few millimeters long. Thus, the frozen synchrotron motion approximation is justified. Consequently, the betatron motion can also be considered frozen due to Eq. 2.20. However, transverse wakes can cause particle loss by defocusing or deflection also within a short DLA structure. This effect is called transverse beam breakup. It can be described analytically by dividing the bunch distribution $\lambda(s)$ in N slices centered at s_n and a width of Δs. For a given initial offset $\hat{y}_0$ of the entire bunch, a deflecting force acts on each slice following the wake kick in Eq. 5.8b as

$$y_n'' = \frac{q q_{\text{bunch}}}{p_{z0} \beta c_0 \lambda_z} W_y(s_n, \hat{y}_0). \tag{6.6}$$

Frozen synchrotron motion means, that s_n stays constant along the DLA structure. Thus, the right hand side of Eq. 6.6 does not depend on y_n or the longitudinal position z of the bunch in the structure. Equation 6.6 can be integrated twice and the n-th slice has an offset of

$$y_n(z) = \hat{y}_0 + \frac{q q_{\text{bunch}}}{2 p_{z0} \beta c_0 \lambda_z} W_y(s_n, \hat{y}_0) z^2. \tag{6.7}$$

This is equal to Chao's two-particle model [93] in the limit $k_\beta z = 2\pi z/\lambda_\beta = 2\pi z/\lambda_s \ll 1$. Figure 6.3 shows the tracking results of a 16 fC Gaussian bunch with a longitudinal bunch length of 50 nm and $\sigma_y = \sigma_x = 75\,\mathrm{nm}$ injected with an offset of 200 nm. In plot (a), centroids of five bunch slices in y-direction are compared to the corresponding analytical solutions given by Eq. 6.7. The tracking results fit in with the analytical description quite well as long as the bunch slices (indicated by the distance of two standard devia-

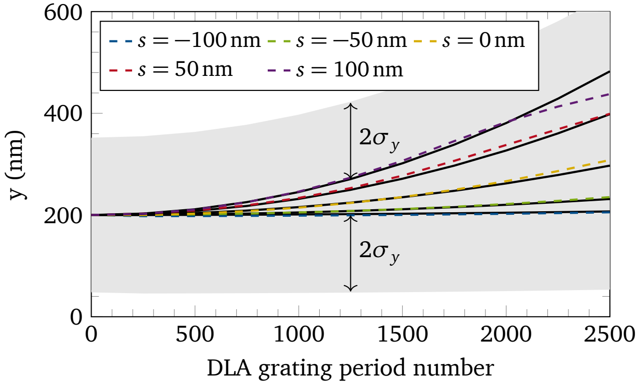

(a) Comparison of slice center of mass for a tracked bunch divided into five slices (dashed lines) with the analytical description (black solid lines). The gray area shows the 2σ distance to the minimum and maximum curve (adapted from [43, Fig. 7]).

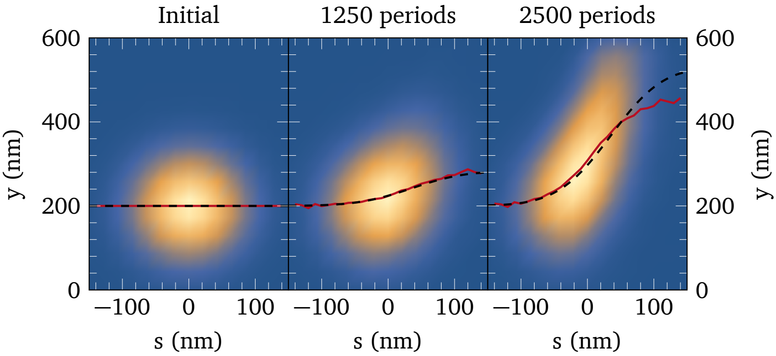

(b) Initial bunch distribution and bunch distribution after 1250 and 2500 DLA grating periods. The red curves show the means of transverse slices in comparison to the analytical estimates (black curves) (adapted from [43, Fig. 8]).

Figure 6.3: Comparison of tracking a bunch through 2500 DLA grating periods with the analytical description. The aperture of the dual pillar structure with 2 µm period length is at $y = 600$ nm.

tions) are within the aperture. In the analytical model, the maximal interaction length is obtained as proportional to $\sqrt{p_{z0}\beta_{\text{ref}}/q_{\text{bunch}}}$. In this tracking example, it results in up to about 4.72 mm (2360 DLA periods) grating length with negligible particle loss. However, particle loss starts earlier as visible in the decreasing slope of the maximum tracked curve in Fig. 6.3a. This is caused by an increasing standard deviation of the bunch distribution due to defocusing of the macroparticle slices which is not included in the analytical description. The bottom plot (Fig. 6.3b) shows the initial and resulting bunch distributions after 1250 and 2500 DLA grating periods. If the transverse width of a bunch is small compared to the aperture, the analytical description gives a good estimate for the transverse deflection of the bunch tail. However, if the bunch fills most of the aperture, tracking covers also the effect of the wake defocusing forces.

Since the external forces, which can potentially counteract the deflection, are much weaker than the forces by the transverse wake field, damping of the effect is not possible. Nevertheless, in order to reduce the deflection and defocusing particle loss, the injection offset has to be minimized as good as possible. However, this is technically difficult to ensure within an accuracy of a few tens of nanometers and helps only in symmetric structures and with symmetric non-tilted bunch distributions. Complete mitigation can only be obtained by reduced bunch charge, geometrical wake optimization, or simply by a more stiff beam at higher energy, such that the rising bunch width is kept below the aperture limit at given DLA structure length.

6.3 Head Tail Instability

This section focuses on lower beam energies where wake driven instabilities occur at the same time scale as a synchrotron and betatron period of an APF FODO lattice. In this regime, the focusing forces by the laser field counteract the deflecting forces by the wake field. This interplay leads to the so-called strong head tail instability. Section 6.3.1 starts with the analysis of the strong head tail instability in a beam transport lattice, which is an APF FODO lattice with strictly periodic cells. Section 6.3.2 extends this lattice to an accelerating, quasi-periodic lattice with decreasing focusing strength. A possible damping mechanism is introduced in Sec. 6.3.3.

6.3.1 Beam Transport

We consider a 6.5 MeV electron beam passing through an APF transport lattice with a peak gradient of 0.56 GV m^{-1} corresponding to the experimental parameters at PEGASUS [18] (see App. A.1.3 for details about PEGASUS). The synchrotron period length of a transport lattice, i.e., with a synchronous phase ± 90° off-crest, is in the range of a few millimeters and therefore in the same order of magnitude as the interaction length or below. Thus, we have to take the longitudinal and transverse motion driven by the laser field into account, which is possible by tracking particles using DLAtrack6D.

For the validation of the tracking results with wake effects, we adapt an analytical description of the strong head tail instability from the literature, which is Chao's two-particle model for synchrotrons [93, Sec. 4.3]. The simplified model considers a bunch which is made of two macroparticles executing synchrotron oscillations with equal amplitude but opposite phase. The smooth approximation is applied, i.e., the alternating focusing and defocusing segments are replaced by a constant focusing with the same phase advance per lattice cell μ (cf. Eq. 1.9). The betatron wavenumber is then given by $k_\beta = \mu/L$, where L is the length of a lattice cell. The resulting oscillation is sinusoidal and the flutter of the trajectories by the focusing and defocusing segments is averaged out. During the first half of the synchrotron period, the leading particle has the index 1, the trailing particle the index 2. In the second half, the order of the macroparticles has changed. The leading particle is not affected by the transverse wake field (see Sec. 1.3) and performs unperturbed betatron oscillations (cf. Eq. 2.20). The oscillation of the trailing particle, however, is disturbed by the wake field of the leading particle. Chao's derivation [93, Sec. 4.3] applies the dynamics of conventional accelerators where the synchrotron frequency is usually much smaller than the transverse betatron frequency. According to the dynamics in an APF lattice (cf. Sec. 2.2), both frequencies are indeed the same and we adapt the model in the following.

In the first half of the synchrotron period, the equations of transverse motion for the two macroparticles in a focusing transport lattice in smooth approximation are

$$y_1'' + k_\beta^2 y_1 = 0 \tag{6.8a}$$

$$y_2'' + k_\beta^2 y_2 = C_\mathrm{W} y_1, \tag{6.8b}$$

with the wake-constant

$$C_\mathrm{W} = \frac{q q_\mathrm{bunch}}{p_{z0} \beta c_0 \lambda_0} W_y', \tag{6.9}$$

where q is the particle charge, q_bunch is the bunch charge, p_{z0} and β are the longitudinal momentum and the velocity of the reference particle, respectively, c_0 is the speed of light, and λ_0 is the laser wavelength. We assume the wake is a constant longitudinally and linear in the transverse offset, such that the slope $W_y' = \partial W_y / \partial y$ of the transverse wake per grating cell is a constant. A solution of Eq. 6.8a for the leading particle is the unperturbed (betatron) oscillation

$$y_1(z) = y_1(0) \cos\left(k_\beta z\right) + \frac{y_1'(0)}{k_\beta} \sin\left(k_\beta z\right), \tag{6.10}$$

where $y_1(0)$ and $y_1'(0)$ are the initial conditions for position and angle of the leading particle, respectively. Accordingly, the initial conditions of the trailing particle are $y_2(0)$ and $y_2'(0)$.

The solution of Eq. 6.8b for the trailing particle is

$$
\begin{aligned}
y_2(z) = \cos\left(k_\beta z\right)&\left[y_2(0) - \frac{y_1'(0)}{2k_\beta^2} C_\mathrm{W} z\right] \\
&+ \sin\left(k_\beta z\right)\left[\frac{y_2'(0)}{k_\beta} + \frac{y_1'(0)}{2k_\beta^3} C_\mathrm{W} + \frac{y_1(0)}{2k_\beta} C_\mathrm{W} z\right].
\end{aligned}
\tag{6.11}
$$

The first terms in the brackets describe the unperturbed (betatron) oscillation of the trailing particle and the second terms, growing linearly with z, describe the perturbation by the transverse wake field of the leading particle. The solutions 6.10 and 6.11 can be combined to a matrix form

$$
\begin{pmatrix} y_1 \\ y_1' \\ y_2 \\ y_2' \end{pmatrix} = \begin{pmatrix} M_\beta^\mathrm{f}(z) & 0 \\ M_\mathrm{W}^\mathrm{f}(z) & M_\beta^\mathrm{f}(z) \end{pmatrix} \begin{pmatrix} y_1 \\ y_1' \\ y_2 \\ y_2' \end{pmatrix}_{z=0} , \tag{6.12}
$$

where the entries in the matrix are the 2x2 lattice maps given by (cf. Eq. 2.30a)

$$
M_\beta^\mathrm{f}(z) = \begin{pmatrix} \cos\left(k_\beta z\right) & \frac{1}{k_\beta}\sin\left(k_\beta z\right) \\ -k_\beta \sin\left(k_\beta z\right) & \cos\left(k_\beta z\right) \end{pmatrix} \tag{6.13}
$$

and

$$
M_\mathrm{W}^\mathrm{f}(z) = \begin{pmatrix} \frac{C_\mathrm{W}}{2k_\beta} z \sin\left(k_\beta z\right) & \frac{C_\mathrm{W}}{2k_\beta^3}\sin\left(k_\beta z\right) - \frac{C_\mathrm{W}}{2k_\beta^2} z \cos\left(k_\beta z\right) \\ \frac{C_\mathrm{W}}{2k_\beta}\sin\left(k_\beta z\right) + \frac{C_\mathrm{W}}{2} z \cos\left(k_\beta z\right) & \frac{C_\mathrm{W}}{2k_\beta} z \sin\left(k_\beta z\right) \end{pmatrix}, \tag{6.14}
$$

which describes the interplay of the two particles via the wake function. The solutions are valid as long as the macroparticles do not change their order. Evaluating Eqs 6.13 and 6.14 after a half longitudinal oscillation period $L_\beta = 2\pi/k_\beta$ and taking into account that the longitudinal oscillation period equals the transverse betatron period, the transfer matrices evaluate as

$$
M_\beta^\mathrm{f}\left(\frac{L_\beta}{2}\right) = \begin{pmatrix} -1 & 0 \\ 0 & -1 \end{pmatrix} \tag{6.15}
$$

and

$$
M_\mathrm{W}^\mathrm{f}\left(\frac{L_\beta}{2}\right) = \begin{pmatrix} 0 & \frac{C_\mathrm{W}}{16\pi^2} L_\beta^3 \\ -\frac{C_\mathrm{W}}{4} L_\beta & 0 \end{pmatrix}. \tag{6.16}
$$

The results for the second half oscillation period where the particles change there position can be obtained by exchanging the indices in Eq. 6.12. The transfer matrix of a full oscillation period is then given by the product of the two half periods as

$$\begin{pmatrix} y_1 \\ y_1' \\ y_2 \\ y_2' \end{pmatrix}_{z=L_\beta} = \begin{pmatrix} 1+M_\mathrm{W}^\mathrm{f}\left(\frac{L_\beta}{2}\right)^2 & M_\mathrm{W}^\mathrm{f}\left(\frac{L_\beta}{2}\right) \\ M_\mathrm{W}^\mathrm{f}\left(\frac{L_\beta}{2}\right) & 1 \end{pmatrix} \begin{pmatrix} y_1 \\ y_1' \\ y_2 \\ y_2' \end{pmatrix}_{z=0} . \tag{6.17}$$

The matrix equation 6.17 is repeatedly applied along the lattice. We can now formulate the resulting transfer matrix in an eigenvalue equation according to Chao's stability analysis. The stability of the system is determined by the eigenvalues, which are

$$\lambda_{1/2} = \frac{1}{128\pi^2}\left(128\pi^2 - C_\mathrm{W}^2 L_\beta^4 \pm i\,|C_\mathrm{W}|\,L_\beta^2\sqrt{256\pi^2 - C_\mathrm{W}^2 L_\beta^4}\right). \tag{6.18}$$

Stability is ensured for $\left|\lambda_{1/2}\right| = 1$. This is equivalent to the requirement that the characteristic polynomial

$$\lambda_{1/2} + 1/\lambda_{1/2} = 2 - \frac{C_\mathrm{W}^2 L_\beta^4}{64\pi^2} \tag{6.19}$$

is real and its value is between -2 and 2. The first condition is always fulfilled. The second condition gives the stability criterion

$$\frac{q q_\text{bunch}}{p_{z0}\beta c_0 \lambda_z \hat{y}_0} W_y\left(\sigma_s, \hat{y}_0\right) = C_\mathrm{W} \le \frac{16\pi}{L_\beta^2}. \tag{6.20}$$

For the PEGASUS parameters with a peak gradient of 0.56 GV m^{-1} [18], an APF FODO cell length of 1808 DLA grating periods (1.44 mm) with a laser wavelength of 0.8 µm and a bunch length of 20 nm, the maximal bunch charge is about 0.3 fC. According to the APF design procedure (cf. Sec. 2.3), the FODO cell length is chosen such that the maximal Twiss beta function (without wake) is minimized. Following Eq. 6.20, a further minimization of the betatron period length would increase the maximal bunch charge. It would, however, increase the maximal Twiss beta function at the same time and thus decrease the initial acceptance. Additionally, a modification of the structure can possibly increase the maximal bunch charge. An increased vacuum gap would, for example, reduce the wake field. At the same time the focusing fields would not change so strongly due to the large relativistic factor, on which the exponential decrease of the external fields in the gap depends inversely.

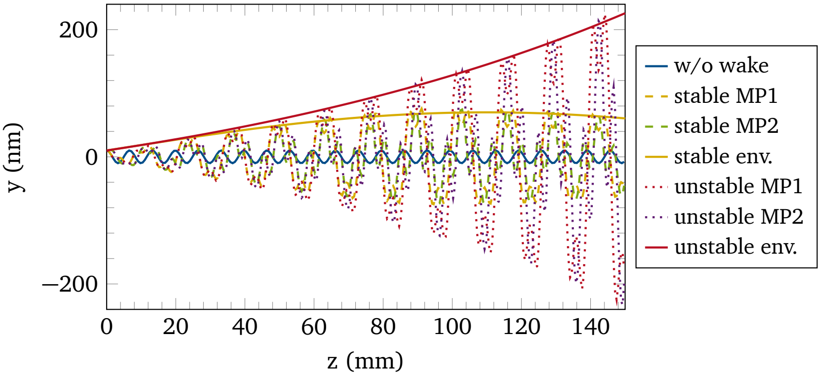

Figure 6.4: Two-particle model in smooth approximation. For a small initial offset, a transversely stable bunch has a sinusoidal envelope (yellow line) and an unstable bunch has an exponentially growing amplitude (red line). The y-offsets of both macroparticles (MP1 and MP2) are plotted respectively. The initial excitation without wake is shown for comparison (blue) (adapted from [43, Fig. 16]).

Looking in detail on the motion of the two macroparticles, the coherent oscillation of a transversely stable bunch in y has a sinusoidal envelope whereas the oscillation amplitude of an unstable bunch grows exponentially. Figure 6.4 shows the oscillation of both macroparticles and the corresponding envelopes for stable and unstable motion, respectively. Note that the smooth approximation, i.e., constant focusing, is used for this calculation. In order to apply the two-particle model without smooth approximation, we have to calculate also the transfer matrices for the defocusing sections in an APF grating (with transverse wake fields). The equations of transverse motion in these defocusing sections are equal to the Eqs. 6.8 except that sign changes. This change of sign results in exchanging the trigonometric functions in the solutions of the equations of motion (Eqs. 6.10 and 6.11) by hyperbolic functions. Writing the solutions again as matrix equation yields the transfer matrices (cf. Eq. 2.30b)

$$M_\beta^{\mathrm{d}}(z) = \begin{pmatrix} \cosh\left(k_\beta z\right) & \frac{1}{k_\beta}\sinh\left(k_\beta z\right) \\ k_\beta \sinh\left(k_\beta z\right) & \cosh\left(k_\beta z\right) \end{pmatrix} \tag{6.21}$$

and

$$M_{\mathrm{W}}^{\mathrm{d}}(z) = \begin{pmatrix} \frac{C_{\mathrm{W}}}{2k_\beta} z \sinh\left(k_\beta z\right) & \frac{C_{\mathrm{W}}}{2k_\beta^2} z \cosh\left(k_\beta z\right) - \frac{C_{\mathrm{W}}}{2k_\beta^3} \sinh\left(k_\beta z\right) \\ \frac{C_{\mathrm{W}}}{2k_\beta} \sinh\left(k_\beta z\right) + \frac{C_{\mathrm{W}}}{2} z \cosh\left(k_\beta z\right) & \frac{C_{\mathrm{W}}}{2k_\beta} z \sinh\left(k_\beta z\right) \end{pmatrix}. \tag{6.22}$$

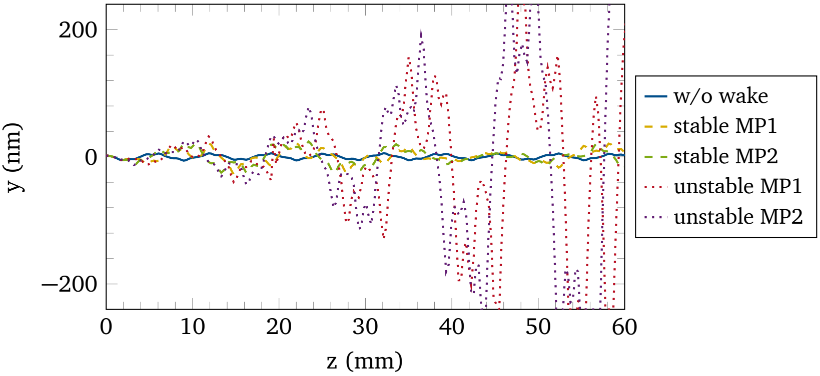

Figure 6.5: Two-particle model using the APF transfer matrices with the wake of a dual pillar APF grating with 0.8 µm period length. The y-offsets of both macroparticles (MP1 and MP2) are plotted respectively. The initial excitation without wake is shown for comparison (blue) (adapted from [43, Fig. 9]).

The APF FODO lattice is then described by the focusing and defocusing tranfer matrices with corresponding focusing strength $k_\beta = \sqrt{K}$ of Eq. 2.21 instead of the averaged focusing strength in smooth approximation. Figure 6.5 shows the y-offset of the macroparticles calculated with the full APF transfer matrices. Tracking with these transfer matrices describes the stability behavior significantly better than with the smooth approximation. Calculating an analytical stability threshold as in Eq. 6.20 is, however, not possible. The alternating sign of the focusing function reduces the stability threshold in this numerical example and for the analyzed interaction length roughly by half. The full tracking results as shown in Fig. 6.6 confirm these semi-analytical estimates. Thus, the two-particle model in smooth approximation can be seen as an upper limit for the estimation of the stability threshold. The more precise limit for a given APF grating with given interaction length is, however, smaller and can be estimated numerically using DLAtrack6D.

6.3.2 Acceleration

In the following, coherent acceleration of a bunch is considered, which requires deviations from strict periodicity of the lattice. Due to the synchronicity condition (Eq. 2.5), the DLA grating periods of a relativistic accelerating lattice ($\beta \approx 1$) are almost identical. That means the first spatial harmonic and thus peak accelerating gradient $\left|\underline{e}_1^0\right|$ and synchronous phase φ_0 are almost constant. This means, a linear energy gain $\gamma(z) = \gamma_0 \left[1 + q\left|\underline{e}_1^0\right| \cos\varphi_0 / \left(m_e c_0^2\right) z\right]$ is provided. The focusing strength decreases proportional to $\gamma^{-3/2}(z)$ (cf. Eq. 2.21) as compared to $\gamma^{-1/2}$ for a magnetic quadrupole

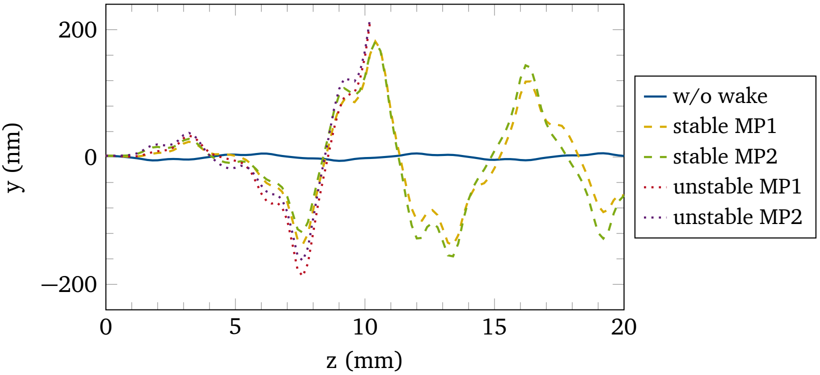

Figure 6.6: Bunch distribution divided in two halves (MP1 and MP2) and tracked through a dual pillar APF grating with a 0.8 μm period length. The betatron motion without wake is shown for comparison (blue) (adapted from [43, Fig. 10]).

lattice [50]. In order to ensure a stable acceleration, there are two approaches to design the APF FODO lattice: One approach is to keep the phase advance per APF FODO cell constant (see Sec. 5.2.3). This implies that the length of the cell needs to be increased in accordance to the decreasing focusing strength. The second approach is to keep the maximal beta function minimal, as described in Sec. 2.3. Both approaches result in the same lattice (see App. A.2).

We can again apply the two-particle model in order to describe the bunch motion. However, we have to consider that the bunch energy is now a function of time and thus equivalently of the longitudinal position in the DLA grating structure, i.e., $\gamma = \gamma(z)$, $k_\beta = k_\beta(\gamma(z))$, and $C_W = C_W(\gamma(z))$. The transverse equations of motion for the two macroparticles are then given by

$$\frac{d}{dz}\left[\gamma(z)\frac{dy_1}{dz}\right] + \gamma(z)\,k_\beta(z)^2\,y_1 = 0 \tag{6.23a}$$

$$\frac{d}{dz}\left[\gamma(z)\frac{dy_2}{dz}\right] + \gamma(z)\,k_\beta(z)^2\,y_2 = \gamma(z)\,C_W(z)\,y_1. \tag{6.23b}$$

For a constant phase advance per FODO cell, the FODO cell length has to be proportional to $\gamma^{3/2}$ according to the energy dependence of the focusing strength. This means

$$k_\beta(z) = \frac{k_{\beta,0}}{\gamma(z)^{3/2}}\gamma_0^{3/2}. \tag{6.24}$$

If we consider the linear energy gain $\gamma(z) = \gamma_0 + q\left|\underline{e}_1^0\right|\cos\varphi_0/\left(m_e c_0^2\right)z$ and apply the transformation $u = 1 + \alpha z$ with $\alpha = q\left|\underline{e}_1^0\right|\cos\varphi_0/\left(\gamma_0 m_e c_0^2\right)$, the equations of motion become

$$\frac{d^2 y_1}{du^2} + \frac{1}{u}\frac{dy_1}{du} + \frac{k_\gamma^2}{u^3}y_1 = 0 \tag{6.25a}$$

$$\frac{d^2 y_2}{du^2} + \frac{1}{u}\frac{dy_2}{du} + \frac{k_\gamma^2}{u^3}y_2 = \frac{C_{W,0}}{\alpha^2 u}y_1. \tag{6.25b}$$

with $k_\gamma = k_{\beta,0}/\alpha$. A solution of Eq. 6.25a is

$$y_1(u) = c_1 J_0\left(\frac{2k_\gamma}{\sqrt{u}}\right) + c_2 N_0\left(\frac{2k_\gamma}{\sqrt{u}}\right), \tag{6.26}$$

where $J_n(x)$ and $N_n(x)$ are n-th order Bessel functions of the first and second kind, respectively. In order to determine the constants c_1 and c_2, the initial conditions $y_1(u=1) = y_0$ and $y_1'(u=1) = y_0'$ are applied. This yields

$$c_1 = \frac{y_0 k_\gamma N_1(2k_\gamma) - y_0' N_0(2k_\gamma)}{k_\gamma\left[J_0(2k_\gamma)N_1(2k_\gamma) - J_1(2k_\gamma)N_0(2k_\gamma)\right]} \tag{6.27a}$$

$$c_2 = \frac{-y_0 k_\gamma J_1(2k_\gamma) + y_0' J_0(2k_\gamma)}{k_\gamma\left[J_0(2k_\gamma)N_1(2k_\gamma) - J_1(2k_\gamma)N_0(2k_\gamma)\right]}. \tag{6.27b}$$

Using the asymptotic expressions of the Bessel functions, the solution of the first macroparticle becomes

$$y_1(u) = \sqrt[4]{u}\left[y_0\cos\left(2k_\gamma\left(1 - \frac{1}{\sqrt{u}}\right)\right) - \frac{\alpha y_0 - 4y_0'}{4\alpha k_\gamma}\sin\left(2k_\gamma\left(1 - \frac{1}{\sqrt{u}}\right)\right)\right]. \tag{6.28}$$

The solution of the second macroparticle (Eq. 6.25b) is given in App. A.3. Equation 6.28 and the exemplary particle trajectory plotted in Fig. 6.7 show that the betatron oscillations in a DLA grating are not damped adiabatically compared to a conventional magnetic focusing lattice. In Chao's model, the magnetic focusing strength is increased proportionally to the bunch energy to get a constant betatron wave number [93]. Increasing the focusing strength in an APF lattice is only possible at the price of increasing the laser field strength limited by the material damage threshold or playing with the synchronous phase, which would reduce the accelerating gradient. The adiabatic damping, i.e., the reduction of emittance and physical size of the beam by an increasing beam momentum (see Eqs. 1.18 and 1.20), is being counteracted by the increase in beta function due to reduced focusing strength. Therefore, the adiabatic damping of an initial

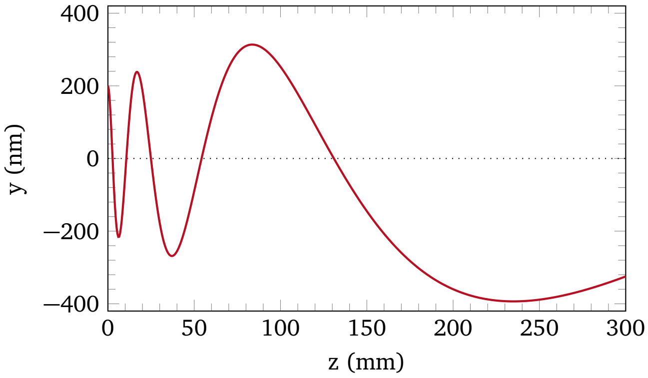

Figure 6.7: Exemplary trajectory of a particle with 6.5 MeV as solution of Eq. 6.26 with an initial focusing strength of $k_{\beta,0} = 644.8\,\mathrm{m}^{-1}$, a peak gradient of $\left|\underline{e}_1^0\right| = 560\,\mathrm{MV\,m}^{-1}$, and a synchronous phase 45° off-crest.

coherent offset in a conventional linear accelerator, which leads to an increased stability threshold [94], does not help for DLA. Instead, the stability threshold is decreased compared to an APF transport channel. This is confirmed by tracking simulations, which are stable in the simulated interaction length in the case of transport and unstable for an accelerated bunch. For an acceleration from 6.5 MeV up to 17 MeV, the numerical simulations show a reduction of the threshold roughly by half as compared to an APF transport channel at constant energy.

6.3.3 Damping Mechanisms

In the analyzed structures, the upper bunch charge limit due to beam loading is in the range of a few femtocoulombs for 1 GeV accelerating gradient (see Sec. 6.1). As the stability criterion of the strong head tail instability, however, is below a femtocoulomb for the same peak gradient (see Sec. 6.3.1), the bunch intensity is thus limited by the transverse effects. To raise the limits, a damping mechanism is required.

BNS-damping [95] named after its inventors Balakin, Novokhatsky, and Smirnov is routinely used in relativistic rf linacs. This damping mechanism is not applicable in APF lattices, since it requires a chirp in phase advance depending on the longitudinal position of the particles within the bunch. In rf linacs, this chirp remains almost unchanged for many transverse betatron periods, because the synchrotron frequency is usually significantly lower than the betatron frequency. Due to the longitudinal motion in an APF lattice, where both frequencies are identical, the particle positions change continuously and a constant chirp in phase advance as function of longitudinal coordinate cannot be achieved.

Another stabilizing mechanism is based on phase mixing [96], i.e., the incoherent betatron frequency spread can under particular circumstances stabilize the bunch against the strong head tail instability. Thus, the bunch charge limit given by Eq. 6.20 is increased at larger emittances. In order to confirm that, tracking simulations in a 5 cm long dual pillar APF grating with varying initial transverse emittances are performed. The matched Gaussian bunch distribution has an initial longitudinal length of 20 nm, a constant width of 400 nm in x-direction, and a particle energy of 6.5 MeV. The FODO cell length is chosen such that the maximum of the Twiss beta function is minimal, i.e., $\hat{\beta}_{y,\max} = 0.69\,\mathrm{mm}$, and the assumed peak accelerating gradient is $5\,\mathrm{GV\,m^{-1}}$. The stable and unstable distributions as functions of the transverse emittance and bunch charge are shown in Fig. 6.8. In the limit of zero transverse emittance the limit of stability is already larger than described by the analytical stability criterion in Eq. 6.20 ($q_{\mathrm{bunch,max}} \approx 1.8\,\mathrm{fC}$), since stabilization is already provided by the finite longitudinal emittance. Moreover, the non-zero width in the x-direction weakens the wake. For increasing transverse emittance, the stability limit is shifted to higher bunch charges, which indicates a stabilization by phase mixing is really present here. Due to the finite aperture of the grating, a further increase of the emittance leads to particle loss before the stabilization by phase mixing can be efficacious. Stable beam transport with larger charge and larger emittance is possible with an increased aperture, which reduces the wake fields. However, this re-

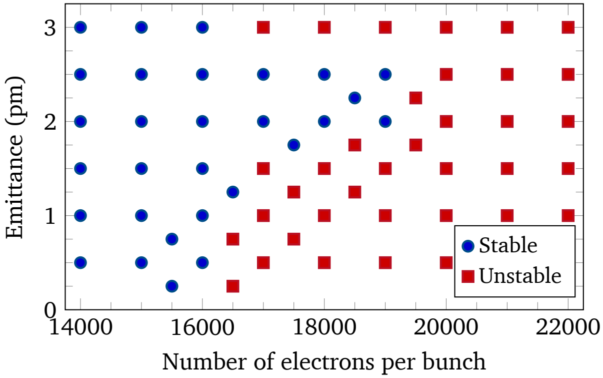

Figure 6.8: Stability diagram of bunch distribution with varying transverse geometric emittance and bunch charge passing through a dual pillar APF structure with 0.8 µm period length. The energy of the particles is 6.5 MeV. Simulation settings with stable behaviour are colored blue and settings with unstable behaviour are colored red (adapted from [43, Fig. 13]).

duces also the accelerating gradient, or requires more laser power, which is limited by the material damage threshold.

Increasing the phase mixing would possibly lead to a stronger damping effect. This is possible by changing the length of one FODO cell of the lattice. Such a slightly not ideal design enlarge the beta function for a given emittance and thus the amplitudes. Another option is the injection of a slightly mismatched bunch. This also results in an increase of the amplitudes. At the same time, larger amplitudes increase the non-linearities in the accelerating fields and that could lead to increasing particle loss. Therefore, all measures to increase the phase-mixing have to be a trade-off between increasing damping of wake field effects and decreasing throughput by the non-linearities of the external fields. Discussing this trade-off for particular experiments that really achieve instability limited bunch charges is beyond the scope of this thesis and outlined for future work.

Summary and Outlook

This thesis is dedicated to beam dynamics simulations in dielectric laser accelerator grating structures including intensity effects caused by wake fields. The accelerating and focusing fields in DLA grating structures are highly non-linear. The apertures of such structures are on the order of a few hundred nanometers. Therefore, a major challenge in the design of DLAs is to achieve a sufficiently high charge throughput.

A detailed understanding of the particle dynamics was reached by means of a field representation by spatial Fourier harmonics. Due to Wideröe's condition, only the synchronous spatial harmonic provides net acceleration. This leads to an analytical description of the accelerating fields by a potential very similar to that in conventional accelerators. However, the equations of motion are non-linear and coupled. For the limit of infinitesimal beam emittance, the linearized equations of motion were solved by applying the Courant-Snyder theory.

The accelerating potential implies, that the transverse fields are always defocusing for longitudinally stable buckets. Magnets cannot overcome the strong defocusing due to the high gradients in DLAs. Thus, a focusing scheme based on jumps in the synchronous phase was proposed. In this alternating phase focusing scheme (APF), alternating between focusing in the longitudinal and one transverse plane confines the beam in both planes. Combined with a tilted pulse front of the driving laser, APF makes DLA fully scalable in structure length. Using APF, acceleration of sub-100 keV electrons up to MeV range with gradients of several $100\,\mathrm{MV\,m^{-1}}$ works with transmission rates well above 90 %. Furthermore, confining both relativistic and sub-relativistic beams is also possible.

In order to simulate the full non-linear dynamics in a lattice, the numerical particle tracking tool DLAtrack6D was applied. DLAtrack6D is based on kicks in all spatial directions once per DLA grating period. The kicks are analytically calculated from the synchronous spatial harmonic. Particle tracking with only one kick per DLA grating period is computationally significantly lighter than tracking in the full electromagnetic fields.

For particle distributions with many electrons per bucket at relativistic energies, wake fields affect the beam dynamics. These are caused by the Smith-Purcell effect at the surface of the periodic grating structures and by the Cherenkov effect in the dielectric material. Wake fields of various DLA grating structures were simulated and the results were compared to an analytical model of metallic corrugated structures for the Smith-Purcell part of the wake field and to simulations of dielectric wake field accelerator structures for the Cherenkov part.

Longitudinal wake fields modulate the energy spectrum of the particle distribution. In the worst case, further acceleration is completely prevented by the wake field. On the other hand, the energy modulating dielectric structures can be used for passive phase space manipulations. In order to have a tunable modulation strength, two different structures were proposed, in which a geometrical parameter is varied along the otherwise invariant direction. A similar structure, but without variation, was used to measure energy modulation caused by longitudinal wake fields in DLA grating structures for the first time. The experiments, conducted in the ACHIP chamber at SwissFEL, have confirmed the simulated wake fields.

Deflection by transverse wake fields can lead to beam instabilities. For the analysis of such instabilities in DLA grating structures, DLAtrack6D was rewritten and extended by wake fields. The wake functions originate from CST simulations. When excited by a sufficiently short bunch, the obtained wake potential is a good approximation of the Green's function wake. Tracking results including wake fields have shown, that transverse wake effects limit the bunch charge stronger than longitudinal, energy modulating effects. Two different energy regimes were distinguished. At high energies, the transverse wake deflects a non-centered bunch and the synchrotron motion is too slow to have any stabilizing effect. The structure length, which is passed through by the bunch without particle loss at the dielectric material, can be calculated upon the wake and the bunch charge. At lower energies, synchrotron and betatron motion and deflection by the wake field are on the same time scale. In the simulated example at 6.5 MeV, the strong head tail instability limits the bunch charge for stable beam transport to a few femtocoulomb for a reasonable peak gradient in the order of one $\mathrm{GV\,m^{-1}}$. In both energy regimes, the description of the transverse effects by analytical models, in particular by a two-particle model, was confirmed by tracking simulations of APF transport lattices. The maximal bunch charge seems low compared to conventional accelerators. However, the possible repetition rate of several megahertz is significantly higher. Moreover, bunch dimensions in the range of some ten to hundred nanometers and a bunch length below one femtosecond are achievable.

In case of acceleration, the adiabatic damping of emittance and thus envelope in conventional accelerators with a magnetic focusing lattice increases the bunch charge limits of the head tail instability. As shown in the thesis, adiabatic damping in an accelerating DLA lattice is counteracted by an increasing Twiss beta function and a coherent offset increases. Thus, the maximum achievable bunch charge decreases for acceleration compared to a pure guiding structure.

Additionally, DLAtrack6D was equipped by a module to determine the phase advance distribution. The results of a transport lattice were compared to analytical values from the linearized theory. The existence of spread in phase advance has indicated, that phase mixing is a possible damping mechanism and it was numerically shown that this effect really stabilizes the bunch in a DLA against transverse wake instabilities.

In this thesis, the APF scheme as well as the investigation of wake fields and intensity effects are limited to two dimensions: the longitudinal and one transverse dimension in which the aperture is defined by the grating (see Secs. 2.2, 3 and 6). In the future, the studies can be extended to three dimensions. For beam confinement in the third dimension, a permanent quadrupole magnet is required and sufficient as long as the dielectric structure is invariant in this dimension. However, the alignment of such a magnet turned out to be a major experimental challenge. Furthermore, the assumption of one invariant direction applies only if structure and laser spot in this direction are significantly larger than the electron beam. Otherwise, the electromagnetic fields in the structure exhibit dependencies such that only a few transverse positions agree with the two-dimensional predictions. This can be overcome by three-dimensional DLA structures. However, there are restrictions to fabrication of such structures by lithographic techniques. A method to create three-dimensional alternating phase focusing fields is the use of silicon on insulator wavers, which are multi-layer systems of silicon and fused silica. An extension of the alternating phase focusing scheme to three dimensions with multi-layer grating structures is proposed in [97]. In this extension, the aperture size in both transverse directions is similar. Thus, in future, the wake field and instability analysis has to be extended to this dimension.

A first wake field experiment, where the third dimension can be exploited, is the energy modulation by a tunable grating as proposed in Sec. 3.2.3. Therein, the third dimension of the structure is used to change the longitudinal wake as function of this dimension. Such an experiment will be carried out at SwissFEL in the near future.

The measurements presented in Chapter 4 can be further improved. The reconstructed longitudinal phase space did not reproduce the measured energy spectra perfectly and the transverse particle distribution was not included. In a coming beam time, phase space measurements can be completed, preferably at two different locations in the beam line. This would allow to validate the tracking from the phase space measurement location to the DLA chamber.

The first DLA net acceleration of an entire bunch at relativistic energies is expected at the ARES linear accelerator (see App. A.1.2). At this facility, a laser modulator is planned for microbunching with a period length equal to the DLA grating period length. The setup offers high-charge microbunches smaller than optical buckets and thus the possibility to experimentally investigate transverse intensity effects for the first time. The models for beam loading and transverse instabilities described in this thesis can be adapted to the ARES parameters and used for theoretical predictions of the expected wake field effects.

Finally, the estimation of maximum achievable beam intensities is crucial for future discussions of possible applications for dielectric laser accelerators with high requirements for beam current. The simulation models and stability thresholds developed in this thesis can be applied to determine the critical quantities.

Appendix

A.1 Accelerator Laboratories

Three members of the ACHIP collaboration are facilities for DLA experiments with relativistic electrons. The free electron laser SwissFEL described in Sec. A.1.1 delivers 3 GeV electrons with relatively high bunch charge and impressive beam quality. The ARES accelerator introduced in Sec. A.1.2 will enable to reach net acceleration by a microbunching setup. Furthermore, the optical setup in the experiment at PEGASUS presented in Sec. A.1.3 with a pulse front tilt allows to increase the DLA interaction length in the range of a few centimeters. At this length and a maximum beam energy of 7 MeV studying focusing lattices based on DLA structures is possible.

A.1.1 SwissFEL

SwissFEL is a X-ray Free Electron Laser facility at the Paul Scherrer Institute in Villigen in Switzerland. Such facilities are a new generation of light sources providing very intense X-ray beams with a pulse length on the order of femtoseconds and wavelengths down to 0.1 nm [86]. They can be used to map the atomic structure of materials, including biomolecules and nanometer scale structures. In detail, SwissFEL contains a rf electron gun creating bunches with 10-200 pC bunch charge and a booster section followed by three linear accelerator sections and two bunch compressors. After the second linear accelerator section at 2-3 GeV, there is a kicker magnet and a switch-yard. With this setting, it is possible to use the subsequent undulator sections and X-ray beam lines in parallel. SwissFEL includes two of them. The Aramis beamline has the third linear accelerator section to increase the electron energy up to 5.8 GeV, an undulator generating X-rays with 0.1-0.7 nm wavelength, and a X-ray beamline to two experimental areas in operation and a third one under construction. The Athos beam line is currently under construction. The undulator in this beamline is designed to generate X-rays with a wavelength of 0.65-5 nm.

The DLA experiments presented in Sec. 4 are conducted in the experimental chamber located in the switch-yard to the Athos beamline [34]. This allows to perform DLA experiments at an electron energy of about 3 GeV. The presented experiment uses a DLA structure with 50 μm period length. The focusing requirements are thus rather relaxed to a beam size of a few micrometers. Beam dynamics simulations have shown that it is even possible to focus the beam with a bunch charge of 1 pC such that it has a rms beam size of 0.26 µm by 0.36 µm with a rms pulse duration of 92 fs and a rms energy spread of 42 keV. Reaching this in an experiment would make it possible to use DLA structures with a period length of 2 µm.

A.1.2 ARES

ARES stands for Accelerator research experiment at SINBAD, which is an abbreviation for Short and innovative bunches and accelerators at DESY. The ARES linear accelerator is foreseen to produce ultra-short electron bunches in order to investigate novel high gradient acceleration techniques [98, 36, 35]. It is currently in the commissioning phase. The lattice contains a 1.5 cell rf gun and two traveling wave structures for the acceleration up to 100 MeV. The bunches with a bunch charge of 0.5-20 pC are compressed by velocity bunching or a magnetic chicane (with slit in the dispersive section) to a sub-femtosecond bunch length. For the DLA experiments, a laser modulator is planned. This setup includes a laser driven undulator creating a sinusoidal energy modulation and a chicane transforming the energy modulation into microbunching. Simulations have shown that the resulting bunch length of the microbunches is sufficient for net acceleration in a DLA structure with 2 µm period length. Due to the use of only one laser for bunching and DLA acceleration, the synchronization is given intrinsically and a possible bunch arrival time jitter of the linear accelerator can be neglected.

A.1.3 PEGASUS

PEGASUS, the photoelectron generated amplified spontaneous undulator radiation source, at UCLA is an university laboratory for basic accelerator research. The accelerator beamline was first commissioned in 2007 [99]. It currently contains a rf photogun and a 11-cell linear accelerator to accelerate electrons to a maximum energy of 7 MeV. In order to focus the beam there are two solenoids and a quadrupole doublet and a transverse deflecting cavity and two spectrometers are installed for measurement purposes. The rf photogun is a highly resonant copper cavity, which generated electron bunches by photo-emission driven by a Ti:Sapphire laser and accelerate them to maximum 4.5 MeV with a normalized emittance smaller than 25 nm when operated at low bunch charge with less than 1 pC [100].

A.2 Accelerating APF Lattice: Design Approaches

There are two approaches to design a stable accelerating APF FODO lattice: One approach is to keep the phase advance per APF FODO cell constant (see Sec. 5.2.3). This implies that the length of the cell L needs to be increased in accordance to the decreasing focusing strength $\sqrt{K}$ such that $\sqrt{K}L = \text{const}$. The second approach is to keep the maximal Twiss beta function minimal, as described in Sec. 2.3. In the following we prove that both approaches result in the same lattice. In order to calculate the maximal beta function, we assume a periodic APF FODO cell and solve the eigenvalue equation

$$\begin{pmatrix} \hat{\beta}_u \\ \hat{\alpha}_u \\ \hat{\gamma}_u \end{pmatrix} = M_{\text{twiss}} \begin{pmatrix} \hat{\beta}_u \\ \hat{\alpha}_u \\ \hat{\gamma}_u \end{pmatrix}, \tag{7.29}$$

where the transfer matrix of the Twiss parameters M_{twiss} is given in Eq. 1.16 with the two-dimensional transfer matrix

$$M_{\text{if},u} = M_{\text{f}}\left(\frac{L}{4}\right) M_{\text{d}}\left(\frac{L}{2}\right) M_{\text{f}}\left(\frac{L}{4}\right). \tag{7.30}$$

The transfer matrices of the focusing and defocusing segments of the APF FODO cell are given in Eq. 2.30. Due to the chosen splitting of the segments in Eq. 7.30, the eigenvector of Eq. 7.29 with $\hat{\alpha}_u = 0$ includes the maximal Twiss beta function

$$\hat{\beta}_{\text{max},u} = \frac{1}{\sqrt{K}} \sqrt{\frac{2}{1 - \frac{\tanh\left(\frac{\sqrt{K}L}{2}\right)}{\sin\left(\frac{\sqrt{K}L}{2}\right)}} - 1}. \tag{7.31}$$

The requirement that the maximal Twiss beta function and thus the square root in Eq. 7.31 is purely real corresponds to the stability condition in Eq. 2.31. If we now choose a APF FODO cell length such that the maximal Twiss beta function is minimal for the focusing strength at initial particle energy, the first derivative

$$\frac{\partial \hat{\beta}_{\text{max},u}}{\partial L} = \frac{4\left[\cosh\left(\frac{\sqrt{K}L}{2}\right)\sin\left(\frac{\sqrt{K}L}{2}\right) + \sinh\left(\frac{\sqrt{K}L}{2}\right)\right]^2 \left[2\sin\left(\frac{\sqrt{K}L}{2}\right) - \cos\left(\frac{\sqrt{K}L}{2}\right)\sinh\left(\sqrt{K}L\right)\right]}{\left\{\cos\left(\sqrt{K}L\right) - 3 + \left[1 + \cos\sqrt{K}L\right]\cosh\sqrt{K}L\right\}^2 \sqrt{\frac{2}{1 - \frac{\tanh\left(\frac{\sqrt{K}L}{2}\right)}{\sin\left(\frac{\sqrt{K}L}{2}\right)}} - 1}} \tag{7.32}$$

vanishes due to the necessary condition of a minimum. For increasing particle energy, the focusing strength decreases. However, the first derivative (Eq. 7.32) has to remain zero to stay on the minimum of the maximal Twiss beta function. Since the derivative is only a function of the product $\sqrt{K}L$, it stays constant if $\sqrt{K}L$ does not change. This corresponds to the design approach of keeping the phase advance constant.

A.3 Accelerating APF Lattice: Solution of Equations of Motion

Section 6.3.2 discusses the head tail instability in an accelerating APF lattice. Therein, the bunch is divided into two macroparticles and the motion of the trailing particle is disturbed by the transverse wake field of the leading particle. The transverse equations of motion for the two macroparticles are given in Eq. 6.25 and Eq. 6.26 describes the solution of the first macroparticle. For the sake of completeness, Eq. 6.25b for the second particle can be solved as

$$y_2(u) = y_1(u) + \frac{C_{W,0}}{\alpha^2} \int_1^u G(u,\tilde{u})\, y_1(\tilde{u})\, \mathrm{d}\tilde{u}, \tag{7.33}$$

where the Green's function is given by

$$G(u,\tilde{u}) = -\pi \left[J_0\left(\frac{2k_\gamma}{\sqrt{u}}\right) N_0\left(\frac{2k_\gamma}{\sqrt{\tilde{u}}}\right) - N_0\left(\frac{2k_\gamma}{\sqrt{u}}\right) J_0\left(\frac{2k_\gamma}{\sqrt{\tilde{u}}}\right)\right] \tag{7.34a}$$

$$\approx \frac{\sqrt[4]{u\tilde{u}}}{k_\gamma} \sin\left(2k_\gamma\left(\frac{1}{\sqrt{u}} - \frac{1}{\sqrt{\tilde{u}}}\right)\right). \tag{7.34b}$$

Lists

List of Figures

List of Symbols

λ_z — Grating period length

λ_0 — Laser wave length

β — Ratio of particle's velocity to speed of light

c_0 — Speed of light

x, y, z — Cartesian coordinates

$\underline{E}_z$ — Complex longitudinal electric field

τ — Pulse length

$\vec{r}$ — Position

t — Time

$\vec{E}$ — Electric field strength

$\vec{D}$ — Electric displacement field

$\varepsilon(\vec{r})$ — Permittivity

ε_r — Relative permittivity

$\vec{B}$ — Magnetic flux density

$\vec{H}$ — Magnetic field strength

$\mu(\vec{r})$ — Permeability

ρ — Charge density

$\vec{J}$ — Current density

$\vec{J}_\kappa$ — Conduction current density

κ — Conductivity

$\vec{J}_\rho$ — Convection current density

$\vec{J}_\mathrm{s}$ — Source current density

ω — Angular frequency

$\vec{k}$ — Wave vector

i — Imaginary unit

$\vec{F}_\mathrm{L}$ — Lorentz force

$\vec{v}$ — Particle’s velocity

q — Particle’s charge

m_p — Particle’s rest mass

$\vec{p}$ — Particle’s momentum

γ — Lorentz factor

$\vec{r}_\mathrm{p}$ — Phase space vector

s — Particle’s distance to the reference particle

δ — Particle’s energy deviation from the reference particle

p_0 — Momentum of the reference particle

M_if — Transfer matrix

K — Focusing strength

L — Lattice period length

u — Placeholder for coordinate x, y, or z

ϕ — Phase advance

μ — Phase advance per lattice period

w — Envelope

ϵ — Emittance

$\hat{\alpha}, \hat{\beta}, \hat{\gamma}$ — Twiss parameters

σ — RMS beam size

V — Potential

ΔE — Energy difference

φ_0 — Synchronous phase of reference particle

E_0 — Energy of reference particle

$\vec{w}$ — Wake function

$\vec{W}$ — Wake potential

λ — Charge / particle distribution

k_loss — Loss factor

$\vec{A}$ — Electromagnetic vector potential

ΔE_p — Particle’s energy gain

m — Order of the spatial harmonic of the evanescent electric field

$\underline{e}_m$ — m-th spatial harmonic of the evanescent electric field

$\underline{e}_m^0$ — m-th spatial harmonic of the evanescent electric field in the gap center

g — Gap size

r — Reflection coefficient

m_e — Electron rest mass

E_kin — Kinetic energy

E_p — Particle’s energy

M_f — Transfer matrix of focusing segment

M_d — Transfer matrix of defocusing segment

L_f — Length of focusing segment

L_d — Length of defocusing segment

$l_{\mathrm{d}\to\mathrm{f}}, l_{\mathrm{f}\to\mathrm{d}}$ — Drift lengths

z_c — Catch-up distance

t — Longitudinal gap between corrugations

h — Depth of corrugations

α — Scaling factor

d — Groove depth

φ — Particle's phase

e — Elementary charge

Ω_s — Synchrotron frequency

$\hat{y}_0$ — Initial injection offset

k_β — Betatron wave number

C_W — Wake field constant

M_β^f — Transfer matrix of focusing segment without wake field

M_β^d — Transfer matrix of defocusing segment without wake field

M_W^f — Transfer matrix of focusing segment with wake field

M_W^d — Transfer matrix of defocusing segment with wake field

L_β — Betatron period length

List of Acronyms

ACHIP — Accelerator on a Chip International Program

APF — Alternating phase focusing

ARES — Accelerator research experiment at SINBAD

BLM — Beam loss monitor

CAD — Computer-aided design

DESY — Deutsches Elektronen-Synchrotron

DLA — Dielectric laser accelerator

DWA — Dielectric wakefield accelerator

FFT — Fast Fourier transform

FODO — Lattice with a focusing and a defocusing segment with drifts in between

FWHM — Full width at half maximum

LCLS — Linac coherent light source

LINAC — Linear accelerator

PEC — Perfect electric conductor

PEGASUS — Photoelectron generated amplified spontaneous undulator radiation source

PFT — Pulse front tilt

PSI — Paul Scherrer Institute

rf — Radio-frequency

rms — Root mean square

SINBAD — Short and innovative bunches and accelerators at DESY

SLAC — Stanford linear accelerator center

SwissFEL — Swiss X-ray free electron laser

TDC — Transverse deflecting cavity

UCLA — University of California Los Angeles

Bibliography

[1] B. C. Stuart, M. D. Feit, A. M. Rubenchik, B. Shore, and M. D. Perry, "Laser-induced damage in dielectrics with nanosecond to subpicosecond pulses," *Phys. Rev. Lett.*, vol. 74, no. 12, pp. 2248–2252, 1995. (cit. on p. 1)

[2] K. Soong, R. L. Byer, E. R. Colby, R. J. England, and E. A. Peralta, "Laser damage threshold measurements of optical materials for direct laser accelerators," *AIP Conf. Proc.*, vol. 1507, pp. 511–515, 2012. (cit. on p. 1)

[3] P. Pronko, P. V. Rompay, C. Horvath, X. Liu, T. Juhasz, and G. Mourou, "Avalanche ionization and dielectric breakdown in silicon with ultrafast laser pulses," *Phys. Rev. B*, vol. 58, no. 5, pp. 2387–2390, 1998. (cit. on p. 1)

[4] M. Polyanskiy, "Refractive index database." *Available at* http://refractiveindex.info. Accessed: 2020-05-13. (cit. on p. 2)

[5] H. H. Li, "Refractive index of silicon and germanium and its wavelength and temperature derivatives," *J. Phys. Chem. Ref. Data*, vol. 9, pp. 561–658, 1980. (cit. on p. 2)

[6] D. Chandler-Horowitz and P. M. Amirtharaj, "High-accuracy, midinfrared ($450\,\mathrm{cm}^{-1} \leq \omega \leq 4000\,\mathrm{cm}^{-1}$) refractive index values of silicon," *J. Appl. Phys.*, vol. 97, p. 123526, 2005. (cit. on p. 2)

[7] R. Kitamura, L. Pilon, and M. Jonasz, "Optical constants of silica glass from extreme ultraviolet to far infrared at near room temperature," *Appl. Optics*, vol. 46, no. 33, pp. 8118–8133, 2007. (cit. on p. 2)

[8] K. Shimoda, "Proposal for an electron accelerator using an optical maser," *Appl. Optics*, vol. 1, no. 1, pp. 33–35, 1962. (cit. on p. 2)

[9] A. Lohmann, "Electron acceleration by light waves," *IBM Technical Note*, vol. 5, pp. 169–182, 1962. (cit. on p. 2)

[10] E. A. Peralta *et al.*, "Demonstration of electron acceleration in a laser-driven dielectric microstructure," *Nature*, vol. 503, pp. 91–94, 2013. (cit. on pp. 2, 5, and 28)

[11] J. Breuer and P. Hommelhoff, “Laser-based acceleration of nonrelativistic electrons at a dielectric structure,” *Phys. Rev. Lett.*, vol. 111, no. 13, p. 134803, 2013. (cit. on pp. 2 and 6)

[12] J. D. Lawson, “Lasers and accelerators,” *IEEE Trans. Nucl. Sci.*, vol. 26, no. 3, pp. 4217–4219, 1979. (cit. on p. 3)

[13] P. M. Woodward, “A method of calculating the field over a plane aperture required to produce a given polar diagram,” *J. Inst. Electr. Eng. - Part IIIA: Radiolocation*, vol. 93, no. 10, pp. 1554–1558, 1946. (cit. on p. 3)

[14] R. B. Palmer, “An introduction to acceleration mechanisms,” in *Frontiers of Particle Beams. Lecture Notes in Physics* (M. Month and S. Turner, eds.), vol. 296, pp. 607–635, Berlin, Heidelberg: Springer, 1988. (cit. on p. 3)

[15] E. Esarey, P. Sprangle, and J. Krall, “Laser acceleration of electrons in vacuum,” *Phys. Rev. E*, vol. 52, no. 5, pp. 5443–5453, 1995. (cit. on p. 3)

[16] K. P. Wootton, Z. Wu, B. M. Cowan, A. Hanuka, I. V. Makasyuk, E. A. Peralta, K. Soong, R. L. Byer, and R. J. England, “Demonstration of acceleration of relativistic electrons at a dielectric microstructure using femtosecond laser pulses,” *Opt. Lett.*, vol. 41, no. 12, pp. 2696–2699, 2016. (cit. on pp. 5 and 28)

[17] D. Cesar *et al.*, “High-field nonlinear optical response and phase control in a dielectric laser accelerator,” *Commun. Phys.*, vol. 1, p. 46, 2018. (cit. on p. 5)

[18] D. Cesar, J. Maxson, P. Musumeci, X. Shen, R. J. England, K. P. Wootton, and S. Tan, “Enhanced energy gain in a dielectric laser accelerator using a tilted pulse front laser,” *Opt. Express*, vol. 26, no. 22, pp. 29216–29224, 2018. (cit. on pp. 5, 44, 80, and 83)

[19] J. Breuer, R. Graf, A. Apolonski, and P. Hommelhoff, “Dielectric laser acceleration of nonrelativistic electrons at a single fused silica grating structure: Experimental part,” *Phys. Rev. Spec. Top-Ac.*, vol. 17, p. 021301, 2014. (cit. on p. 6)

[20] K. J. Leedle, A. Ceballos, H. Deng, O. Solgaard, R. F. Pease, R. L. Byer, and J. S. Harris, “Dielectric laser acceleration of sub-100 keV electrons with silicon dual-pillar grating structures,” *Opt. Lett.*, vol. 40, no. 18, pp. 4344–4347, 2015. (cit. on p. 6)

[21] K. J. Leedle, D. S. Black, Y. Miao, K. E. Urbanek, A. Ceballos, H. Deng, J. S. Harris, O. Solgaard, and R. L. Byer, “Phase-dependent dielectric laser acceleration of electrons with symmetrically driven silicon dual pillar gratings,” *Opt. Lett.*, vol. 43, no. 9, pp. 2181–2184, 2018. (cit. on p. 6)

[22] D. S. Black, K. J. Leedle, Y. Miao, U. Niedermayer, R. L. Byer, and O. Solgaard, “Laser-driven electron lensing in silicon microstructures,” *Phys. Rev. Lett.*, vol. 122, p. 104801, 2019. (cit. on p. 6)

[23] D. S. Black, U. Niedermayer, Y. Miao, O. Solgaard, R. L. Byer, and K. J. Leedle, “Net acceleration and direct measurement of attosecond electron pulses in a silicon dielectric laser accelerator,” *Phys. Rev. Lett.*, vol. 123, no. 26, p. 264802, 2019. (cit. on pp. 6, 23, and 24)

[24] N. Schönenberger, A. Mittelbach, P. Yousefi, U. Niedermayer, and P. Hommelhoff, “Generation and characterization of attosecond micro-bunched electron pulse trains via dielectric laser acceleration,” *Phys. Rev. Lett.*, vol. 123, no. 26, p. 264803, 2019. (cit. on p. 6)

[25] P. Yousefi, N. Schönenberger, J. McNeur, M. Kozák, U. Niedermayer, and P. Hommelhoff, “Dielectric laser electron acceleration in a dual pillar grating with a distributed Bragg reflector,” *Opt. Lett.*, vol. 44, no. 6, p. 1520, 2019. (cit. on p. 6)

[26] N. V. Sapra *et al.*, “On-chip integrated laser-driven particle accelerator,” *Science*, vol. 367, pp. 79–83, 2020. (cit. on p. 6)

[27] J. Breuer, J. McNeur, and P. Hommelhoff, “Dielectric laser acceleration of electrons in the vicinity of single and double grating structures - theory and simulations,” *J. Phys. B-At. Mol. Opt.*, vol. 47, p. 234004, 2014. (cit. on pp. 6 and 24)

[28] T. Hughes, G. Veronis, K. P. Wootton, R. Joel England, and S. Fan, “Method for computationally efficient design of dielectric laser accelerator structures,” *Opt. Express*, vol. 25, no. 13, p. 15414, 2017. (cit. on pp. 6, 24, and 31)

[29] T. Egenolf, O. Boine-Frankenheim, and U. Niedermayer, “Simulation of DLA grating structures in the frequency domain,” in *J. Phys.: Conf. Ser.*, vol. 874, p. 012040, 2017. (cit. on pp. 6, 7, 24, and 31)

[30] U. Niedermayer, O. Boine-Frankenheim, and T. Egenolf, “Designing a dielectric laser accelerator on a chip,” in *J. Phys.: Conf. Ser.*, vol. 874, p. 012041, 2017. (cit. on pp. 6, 7, 24, 26, 31, and 40)

[31] U. Niedermayer, T. Egenolf, and O. Boine-Frankenheim, “Beam dynamics analysis of dielectric laser acceleration using a fast 6D tracking scheme,” *Phys. Rev. Accel. Beams*, vol. 20, no. 11, p. 111302, 2017. (cit. on pp. 6, 7, 21, 22, 24, 25, 33, and 63)

[32] U. Niedermayer, T. Egenolf, O. Boine-Frankenheim, and P. Hommelhoff, "Alternating-phase focusing for dielectric-laser acceleration," *Phys. Rev. Lett.*, vol. 121, no. 21, p. 214801, 2018. (cit. on pp. 6, 7, 25, 28, 29, 31, and 66)

[33] B. Hermann, S. Bettoni, T. Egenolf, U. Niedermayer, E. Prat, and R. Ischebeck, "Laser-driven modulation of electron beams in a dielectric micro-structure for x-ray free-electron lasers," *Sci. Rep.*, vol. 9, p. 19773, 2019. (cit. on pp. 6, 47, and 78)

[34] E. Prat *et al.*, "Outline of a dielectric laser acceleration experiment at SwissFEL," *Nucl. Instrum. Meth. A*, vol. 865, pp. 87–90, 2017. (cit. on pp. 6, 51, 78, and 95)

[35] W. Kuropka, R. Aßmann, F. Burkart, H. Cankaya, U. Dorda, I. Hartl, F. X. Kärtner, F. Lemery, B. Marchetti, and F. Mayet, "Plans for dielectric laser accelerators at SINBAD," in *2018 IEEE Advanced Accelerator Concepts Workshop, AAC 2018 - Proceedings*, (Breckenridge, CO, USA), 2018. (cit. on pp. 6 and 96)

[36] F. Mayet, R. Assmann, J. Bödewadt, R. Brinkmann, U. Dorda, W. Kuropka, C. Lechner, B. Marchetti, and J. Zhu, "Simulations and plans for possible DLA experiments at SINBAD," *Nucl. Instrum. Meth. A*, vol. 909, 2018. (cit. on pp. 6 and 96)

[37] L. Schächter, R. L. Byer, and R. H. Siemann, "Wake field in dielectric acceleration structures," *Phys. Rev. E*, vol. 68, p. 036502, 2003. (cit. on pp. 6, 44, and 75)

[38] A. Hanuka and L. Schächter, "Operation regimes of a dielectric laser accelerator," *Nucl. Instrum. Meth. A*, vol. 888, pp. 147–152, 2018. (cit. on p. 6)

[39] A. Hanuka and L. Schächter, "Optimized operation of dielectric laser accelerators: Multi bunch," *Phys. Rev. Accel. Beams*, vol. 21, p. 064402, 2018. (cit. on pp. 6 and 77)

[40] A. Hanuka and L. Schächter, "Optimized operation of dielectric laser accelerators: Single bunch," *Phys. Rev. Accel. Beams*, vol. 21, p. 054001, 2018. (cit. on pp. 6 and 77)

[41] T. Egenolf and U. Niedermayer, "Analytical energy spectra and wake effects for relativistic dielectric laser accelerators," *J. Phys. Conf. Ser.*, vol. 1596, p. 012017, 2020. (cit. on pp. 7, 26, and 28)

[42] T. Egenolf, U. Niedermayer, and O. Boine-Frankenheim, "Intensity limits by wakefields in relativistic dielectric laser acceleration grating structures," in *2018 IEEE Advanced Accelerator Concepts Workshop, AAC 2018 - Proceedings*, (Breckenridge, CO, USA), 2018. (cit. on pp. 7 and 76)

[43] T. Egenolf, U. Niedermayer, and O. Boine-Frankenheim, “Tracking with wakefields in dielectric laser acceleration grating structures,” *Phys. Rev. Accel. Beams*, vol. 23, p. 054402, 2020. (cit. on pp. 7, 35, 36, 39, 45, 46, 70, 71, 79, 84, 85, 86, and 89)

[44] O. Heaviside, “XI. On the forces, stresses, and fluxes of energy in the electromagnetic Field,” *Philosophical Transactions of the Royal Society of London (A.)*, vol. 183, pp. 423–480, 1892. (cit. on p. 9)

[45] J. C. Maxwell, “VIII. A dynamical theory of the electromagnetic field,” *Phil. Trans. R. Soc.*, vol. 155, pp. 459–512, 1865. (cit. on p. 9)

[46] J. C. Maxwell, *A treatise on electricity and magnetism (Vol. 1)*. Oxford, UK: Clarendon Press, 1873. (cit. on p. 9)

[47] J. C. Maxwell, *A treatise on electricity and magnetism (Vol. 2)*. Oxford, UK: Clarendon Press, 1873. (cit. on p. 9)

[48] F. Frenet, “Sur les courbes à double courbure,” *Journal de Mathématiques Pures et Appliquées*, vol. 17, pp. 437–447, 1852. (cit. on p. 11)

[49] J. A. Serret, “Sur quelques formules relatives à la théorie des courbes à double courbure,” *Journal de Mathématiques Pures et Appliquées*, vol. 16, pp. 193–207, 1851. (cit. on p. 11)

[50] H. Wiedemann, *Particle Accelerator Physics*. Berlin, Heidelberg, New York: Springer-Verlag, 3rd ed., 2007. (cit. on pp. 12 and 86)

[51] G. W. Hill, “On the part of the motion of the lunar perigee which is a function of the mean motions of the sun and moon,” *Acta Math.*, vol. 8, pp. 1–36, 1886. (cit. on p. 12)

[52] E. D. Courant and H. S. Snyder, “Theory of the alternating-gradient synchrotron,” *Annals of Physics*, vol. 3, no. 1, pp. 1–48, 1958. (cit. on p. 12)

[53] S. Y. Lee, *Accelerator Physics*. Singapore, New Jersey, London, Hong Kong: World Scientific, 1999. (cit. on p. 13)

[54] J. Liouville, “Note sur la Théorie de la Variation des constantes arbitraires,” *Journ. de Math.*, vol. 3, pp. 342–349, 1838. (cit. on p. 14)

[55] R. Wideröe, “Über ein neues Prinzip zur Herstellung hoher Spannungen,” *Archiv für Elektrotechnik*, vol. 21, no. 4, pp. 387–406, 1928. (cit. on pp. 15 and 22)

[56] T. Weiland and R. Wanzenberg, “Wake fields and impedances,” in *Proc. of 4th US-CERN School on Particle Accelerators*, (Hilton Head Island, SC, USA), pp. 39–79, 1990. (cit. on pp. 17, 18, and 19)

[57] U. Niedermayer, “Bench Measurements and Simulations of Beam Coupling Impedance,” *CERN Yellow Reports: School Proceedings*, vol. 3, pp. 81–105, 2017. (cit. on p. 17)

[58] K. Y. Ng, *Physics of Intensity Dependent Beam Instabilities*. Singapore, New Jersey, London, Hong Kong: World Scientific, 2006. (cit. on p. 18)

[59] P. B. Wilson, “High energy electron linacs: applications to storage ring rf systems and linear colliders,” Tech. Rep. SLAC-PUB-2884, Stanford Linear Accelerator Center, Stanford, CA, USA, 1991. (cit. on pp. 18 and 75)

[60] L. Palumbo, V. G. Vaccaro, and M. Zobov, “Wake fields and impedance,” in *Proc. of the CERN Accelerator School*, (Rhodes, Greece), 1994. (cit. on p. 18)

[61] W. K. H. Panofsky and W. A. Wenzel, “Some considerations concerning the transverse deflection of charged particles in radio-frequency fields,” *Rev. Sci. Instrum.*, vol. 27, p. 967, 1956. (cit. on pp. 19 and 25)

[62] U. Niedermayer *et al.*, “Challenges in simulating beam dynamics of dielectric laser acceleration,” *Int. J. Mod. Phys. A*, vol. 34, p. 1942031, 2019. (cit. on pp. 23, 24, and 45)

[63] B. Naranjo, A. Valloni, S. Putterman, and J. B. Rosenzweig, “Stable charged-particle acceleration and focusing in a laser accelerator using spatial harmonics,” *Phys. Rev. Lett.*, vol. 109, p. 164803, 2012. (cit. on p. 28)

[64] W. Shin and S. Fan, “Accelerated solution of the frequency-domain Maxwell’s equations by engineering the eigenvalue distribution of the operator,” *Opt. Express*, vol. 21, no. 19, p. 22578, 2013. (cit. on p. 31)

[65] Dassault Systemes Deutschland GmbH, “CST Studio Suite 2019,” 2019. (cit. on pp. 31, 33, and 35)

[66] Wolfram Research Inc., “Wolfram Mathematica 11,” 2017. (cit. on p. 33)

[67] D. Cesar, J. Maxson, P. Musumeci, X. Shen, R. J. England, and K. P. Wootton, “Optical design for increased interaction length in a high gradient dielectric laser accelerator,” Tech. Rep. SLAC-PUB-17180, Stanford Linear Accelerator Center, Stanford, CA, USA, 2017. (cit. on p. 31)

[68] M. Kozák, J. McNeur, N. Schönenberger, J. Illmer, A. Li, A. Tafel, P. Yousefi, T. Eckstein, and P. Hommelhoff, “Ultrafast scanning electron microscope applied for studying the interaction between free electrons and optical near-fields of periodic nanostructures,” *J. Appl. Phys.*, vol. 124, p. 023104, 2018. (cit. on p. 31)

[69] T. Weiland, “Eine Methode zur Lösung der Maxwellschen Gleichungen für sechskomponentige Felder auf diskreter Basis,” *Archiv für Elektronik und Übertragungs-technik*, vol. 31, no. 3, pp. 116–120, 1977. (cit. on p. 35)

[70] P. B. Wilson, “Introduction to wakefields and wake potentials,” Tech. Rep. SLAC-PUB-4547, Stanford Linear Accelerator Center, Stanford, CA, USA, 1989. (cit. on p. 36)

[71] K. Bane, “Wakefield effects in a linear collider,” in *AIP Conf. Proc. 153*, pp. 971–1014, 1987. (cit. on pp. 37 and 44)

[72] Tech-X, “VSim 8.1,” 2017. (cit. on p. 40)

[73] E. Gjonaj, X. Dong, R. Hampel, M. Kärkkäinen, T. Lau, W. F. O. Müller, and T. Weiland, “Large scale parallel wake field computations for 3D-accelerator structures with the PBCI code,” in *Proc. of ICAP 2006*, (Chamonix, France), pp. 29–34, 2006. (cit. on p. 40)

[74] K. Bane, G. Stupakov, and I. Zagorodnov, “Analytical formulas for short bunch wakes in a flat dechirper,” *Phys. Rev. Accel. Beams*, vol. 19, p. 084401, 2016. (cit. on p. 40)

[75] A. Tremaine, J. Rosenzweig, and P. Schoessow, “Electromagnetic wake fields and beam stability in slab-symmetric dielectric structures,” *Phys. Rev. E*, vol. 56, no. 6, pp. 7204–7216, 1997. (cit. on p. 42)

[76] D. Mihalcea, P. Piot, and P. Stoltz, “Three-dimensional analysis of wakefields generated by flat electron beams in planar dielectric-loaded structures,” *Phys. Rev. Spec. Top-Ac.*, vol. 15, no. 8, p. 081304, 2012. (cit. on p. 42)

[77] P. D. Hoang *et al.*, “Experimental characterization of electron-beam-driven wakefield modes in a dielectric-woodpile cartesian symmetric structure,” *Phys. Rev. Lett.*, vol. 120, p. 164801, 2018. (cit. on p. 42)

[78] M. W. Guetg *et al.*, “Commissioning of the RadiaBeam/SLAC dechirper,” in *Proc. 7th Int. Particle Accelerator Conf. (IPAC16)*, (Busan, Korea), pp. 809–812, 2016. (cit. on p. 47)

[79] J. Zemella *et al.*, “Measurements of wake-induced electron beam deflection in a dechirper at the Linac Coherent Light Source,” *Phys. Rev. Accel. Beams*, vol. 20, p. 104403, 2017. (cit. on p. 47)

[80] P. Yousefi, J. McNeur, M. Kozák, F. Gannott, O. Lohse, and P. Hommelhoff, “Silicon dual pillar structure with a distributed Bragg reflector for dielectric laser accelerators: Design and fabrication,” *Nucl. Instrum. Meth. A*, vol. 909, pp. 221–223, 2018. (cit. on p. 47)

[81] “FEMTOprint SA.” https://www.femtoprint.ch. Accessed: 2020-06-10. (cit. on pp. 47 and 51)

[82] C. J. Milne *et al.*, “SwissFEL: The Swiss X-ray Free Electron Laser,” *Appl. Sci.*, vol. 7, p. 720, 2017. (cit. on p. 51)

[83] E. Ferrari *et al.*, “The ACHIP experimental chambers at the Paul Scherrer Institut,” *Nucl. Instrum. Meth. A*, vol. 907, pp. 244–247, 2018. (cit. on p. 51)

[84] C. Ozkan Loch, D. Llorente Sancho, P. Pollet, G. Marinkovic, R. Ischebeck, and V. Schlott, “System integration of SwissFEL beam loss monitors,” in *Proc. of IBIC 2015*, (Melbourne, Australia), pp. 170–174, 2015. (cit. on p. 53)

[85] G. L. Orlandi *et al.*, “Nanofabricated free-standing wire scanners for beam diagnostics with submicrometer resolution,” *Phys. Rev. Accel. Beams*, vol. 23, no. 4, p. 42802, 2020. (cit. on p. 53)

[86] “SwissFEL Conceptual Design Report,” Tech. Rep. PSI Bericht Nr. 10-04, Paul Scherrer Institute, Villigen, Switzerland, 2012. (cit. on pp. 53 and 95)

[87] P. Emma, J. Frisch, and P. Krejcik, “A transverse RF deflecting structure for bunch length and phase space diagnostics,” Tech. Rep. LCLS-TN-00-12, Stanford Linear Accelerator Center, Stanford, CA, USA, 2000. (cit. on pp. 53 and 57)

[88] M. Borland, “elegant: A flexible SDDS-compliant code for accelerator simulation,” Tech. Rep. APS LS-287, Advanced Photon Source, Argonne, IL, USA, 2000. (cit. on p. 54)

[89] P. Craievich *et al.*, “Sub-femtosecond time-resolved measurements based on a variable polarization X-band transverse deflecting structures for SwissFEL,” in *Proc. of 38th Int. Free-Electron Laser Conf. (FEL2017)*, (Santa Fe, NM, USA), p. WEP040, 2018. (cit. on p. 61)

[90] MathWorks, “Matlab,” 2016. (cit. on p. 64)

[91] Python Software Foundation, “Python 3.7,” 2018. (cit. on p. 64)

[92] A. Luccio and N. D'Imperio, "Eigenvalues of the one-turn matrix," Tech. Rep. C-A/AP#126, Brookhaven National Laboratory, Upton, NY, 2003. (cit. on p. 67)

[93] A. Chao, *Physics of collective beam instabilities in high energy accelerators*. New York: John Wiley & Sons, 1993. (cit. on pp. 76, 78, 81, and 87)

[94] A. W. Chao, "Coherent instabilities of a relativistic bunched beam," Tech. Rep. SLAC-PUB-2946, Stanford Linear Accelerator Center, Stanford, CA, USA, 1982. (cit. on p. 88)

[95] V. E. Balakin, A. V. Novokhatsky, and V. P. Smirnov, "VLEPP transverse beam dynamics," in *Proc. of the 12th Intern. Conf. on High-Energy Accelerators*, (Batavia, IL, USA), pp. 119–120, 1983. (cit. on p. 88)

[96] A. Hofmann, "Landau damping," in *CAS - CERN Accelerator School: Intermediate Course on Accelerator Physics*, (Zeuthen, Germany), pp. 271–304, 2006. (cit. on p. 89)

[97] U. Niedermayer, T. Egenolf, and O. Boine-Frankenheim, "Threedimensional alternating-phase focusing for dielectric-laser electron accelerators," *ArXiv preprint 2004.05458*, 2020. Submitted to Phys. Rev. Lett. (cit. on p. 93)

[98] B. Marchetti *et al.*, "Electron-beam manipulation techniques in the SINBAD Linac for external injection in plasma wake-field acceleration," *Nucl. Instrum. Meth. A*, vol. 829, pp. 278–283, 2016. (cit. on p. 96)

[99] P. Musumeci, J. Moody, and G. Gatti, "Ultrafast beam research at the PEGASUS laboratory," in *Proc. of PAC 2007*, (Albuquerque, NM, USA), pp. 2751–2753, 2007. (cit. on p. 96)

[100] D. Cesar, *Probing Ultrafast Dynamics With Relativistic Electrons*. PhD thesis, UCLA, 2019. (cit. on p. 96)

Acknowledgements

An dieser Stelle möchte ich all jenen meinen Dank ausdrücken, deren Unterstützung erst ermöglicht hat, dass ich meine Dissertation erfolgreich abschließe.

Bedanken möchte ich mich bei Prof. Oliver Boine-Frankenheim für die Betreuung während der Promotion und bereits zuvor während meiner Bachelor- und Masterarbeit. Seine Beschleunigerphysik-Vorlesung hat mich erst ans TEMF geführt und seine Angebote haben mich jedes Mal davon überzeugt auch dort zu bleiben. Mein besonderer Dank gilt Dr. Uwe Niedermayer für die federführende Betreuung aller meiner Abschlussarbeiten, auch wenn dies bei der Promotion nur inoffiziell war. Vielen Dank für all die fachlichen Diskussionen, zahlreiche weiterführende Ideen, das direkte Feedback und insbesondere die zahlreichen Kommentare beim Korrekturlesen dieser Arbeit. Ebenso möchte ich Prof. Holger Podlech für die Bereitschaft danken, das Korreferat dieser Arbeit zu übernehmen.

Mein Dank gilt allen Kollegen am TEMF. Durch Euch hat es immer viel Spaß gemacht, an diesem Institut zu arbeiten. Ein besonderer Dank geht an meine Bürokollegen Dr. Nicolas Marsic und Mikhail Patrushev für die sehr angenehme Arbeitsatmosphäre. Bedanken möchte ich mich auch bei allen Mitgliedern unserer Arbeitsgruppe für die gegenseitige Unterstützung, insbesondere bei Aamna Khan für die Hinweise zu meiner Arbeit. Ebenso möchte ich mich bei allen Mitgliedern des GED-Teams für die immer hoch motivierte Arbeit in der Vorlesungsbetreuung bedanken. Danken möchte ich außerdem Heike Koch, Dr. Wolfgang Müller, Achim Wagner und Dragos Munteanu, die immer zur Stelle sind und uns Promovierenden am TEMF viele organisatorische Aufgaben abnehmen.

Ich möchte mich bei allen Mitgliedern der ACHIP Kollaboration für den regen wissenschaftlichen Austausch besonders während der Treffen an unterschiedlichsten Orten auf drei Kontinenten und in zahlreichen Videokonferenzen bedanken. Ein besonderer Dank gilt Rasmus Ischebeck und Benedikt Hermann, die mich mehrmals am PSI willkommen geheißen haben. Ohne ihre experimentelle Arbeit, die Simulationen und die Diskussion der Ergebnisse wäre ein Teil dieser Arbeit nicht möglich gewesen.

Schließlich möchte ich mich bei meiner Familie bedanken. Auch wenn Ihr in meinem Leben eigentlich immer an erster Stelle steht, musstet Ihr vor allem in den letzten Monaten meiner Promotion etwas zurücktreten. Heike und Didi, vielen Dank, dass Ihr mich auf dem Weg bis zur Promotion immer unterstützt habt! Aniko, vielen Dank für all die Ermutigungen, egal wie gestresst oder mies gelaunt ich teilweise war ... und für alles andere. Ich liebe Dich, mein Schatz! Fiona, vielen Dank, dass Du während meiner Promotion in unser Leben getreten bist. Etwas Besseres konnte uns nicht passieren.

Diese Arbeit wurde gefördert durch das Bundesministerium für Bildung und Forschung (Projekt-Nr. FKZ: 05K16RDB) und die Gordon and Betty Moore Foundation (Projekt-Nr. GBMF4744).

Curriculum Vitae

Thilo Egenolf

born on 22.06.1988 in Wiesbaden, Germany

Education

Oct. 2015 – May 2017	**M. Sc. in Physics at TU Darmstadt** (German grade 1.28) specialized in accelerator physics Thesis: Development of a 2D finite element solver for DLA structures Supervisor: Prof. Dr. Oliver Boine-Frankenheim
Oct. 2009 – Sept. 2015	**B. Sc. in Physics at TU Darmstadt** (German grade 1.6) Thesis: Impedance of the beam pipe for the Future Circular Collider Supervisor: Dr. Uwe Niedermayer
Aug. 1999 – July 2008	**General qualification for university entrance (Abitur)** (German grade 1.0) Diltheyschule Wiesbaden

Work Experience

June 2017 – Present	**Research staff** Institute for Accelerator Science and Electromagnetic Fields Technical University Darmstadt
Oct. 2010 – July 2016	**Student assistant** Teaching assistant at various lectures in the physics, electrical engineering and computer science departments Technical University Darmstadt
Sept. 2008 – Aug. 2009	**Voluntary social year** Emergency medical services at Arbeiter-Samariter-Bund Wiesbaden

Publication List

Journal Articles

- **T. Egenolf**, U. Niedermayer, and O. Boine-Frankenheim, *Tracking with wakefields in dielectric laser acceleration grating structures*, Phys. Rev. Accel. Beams 23, 054402 (2020).
- B. Hermann, ..., **T. Egenolf** et al., *Laser-driven modulation of electron beams in a dielectric micro-structure for X-ray free-electron lasers*, Sci. Rep. 9, 19773 (2019).
- U. Niedermayer, ..., **T. Egenolf** et al., *Challenges in simulating beam dynamics of dielectric laser acceleration*, Int. J. Mod. Phys. A 34, 1942031 (2019).
- U. Niedermayer, **T. Egenolf**, O. Boine-Frankenheim, and P. Hommelhoff, *Alternating-phase focusing for dielectric-laser acceleration*, Phys. Rev. Lett. 121, 214801 (2018).
- U. Niedermayer, **T. Egenolf**, and O. Boine-Frankenheim, *Beam dynamics analysis of dielectric laser acceleration using a fast 6D tracking scheme*, Phys. Rev. Accel. Beams 20, 111302 (2017).

Preprints

- U. Niedermayer, **T. Egenolf** and O. Boine-Frankenheim, *Threedimensional alternating-phase focusing for dielectric-laser electron accelerators*, accepted for publication in Phys. Rev. Lett. (2020), ArXiv ID: 2004.05458.

Conference Proceedings

- **T. Egenolf** and U. Niedermayer, *Analytical energy spectra and wake effects for relativistic dielectric laser accelerators*, J. Phys. Conf. Ser. 1596, 012017 (2020).
- B. Hermann, ..., **T. Egenolf** et al., *Diagnostics for electron pulse trains at SwissFEL obtained by energy modulation in a laser-driven dielectric structure*, J. Phys. Conf. Ser. 1596, 012046 (2020).

- U. Niedermayer, ..., **T. Egenolf** et al., *Challenges in simulating beam dynamics of dielectric laser acceleration*, in Proceedings of ICAP'18, Key West, FL, USA (2018).
- **T. Egenolf**, U. Niedermayer, and O. Boine-Frankenheim, *Intensity limits by wakefields in relativistic dielectric laser acceleration grating structures*, 2018 IEEE Advanced Accelerator Concepts Workshop, Breckenridge, CO, USA (2018).
- **T. Egenolf**, O. Boine-Frankenheim, and U. Niedermayer, *Simulations of DLA grating structures in the frequency domain*, J. Phys. Conf. Ser. 874, 012040 (2017).
- U. Niedermayer, O. Boine-Frankenheim, and **T. Egenolf**, *Designing a dielectric laser accelerator on a chip*, J. Phys. Conf. Ser. 874, 012041 (2017).
- K. P. Wootton, ..., **T. Egenolf** et al., *Towards a fully integrated accelerator on a chip: dielectric laser acceleration from the source to relativistic electrons*, in Proceedings of IPAC'17, Copenhagen, Denmark (2017).

Conference Contributions

- *Transverse beam breakup instability in dielectric laser accelerators*, Poster presentation at EAAC2019, Isola d'Elba, Italy (2019)
- *Transverse intensity effects in dielectric laser accelerators*, Poster presentation at Workshop "Advances in Electromagnetic Research - KWT 2019", Riezlern, Austria (2019).
- *Wakefield tracking in dielectric laser acceleration grating structures*, Poster presentation at DPG spring meeting, Munich, Germany (2019).
- *Intensity limits by wakefields in relativistic dielectric laser acceleration grating structures*, Poster presentation at AAC'18, Breckenridge, CO, USA (2018).
- *Intensity limits of DLA grating structures at relativistic energies*, Poster presentation at DPG spring meeting, Würzburg, Germany (2018).
- *Simulating DLA grating structures in the time and frequency domain*, Oral presentation at Workshop "Advances in Electromagnetic Research - KWT 2017", Riezlern, Austria (2017).
- *Simulations of DLA grating structures in the frequency domain*, Poster presentation at IPAC'17, Copenhagen, Denmark (2017).
- *Simulations of DLA structures based on FEM in the frequency domain*, Oral presentation at DPG spring meeting, Dresden, Germany (2017).